# Fundamental Design Considerations for Nuclear Space Power Systems

A dissertation submitted to The University of Manchester for the degree of
**Master of Science in Nuclear Science and Technology**
in the Faculty of Science and Engineering

**Year of submission**
2023

**Student ID**
11173631 - Yuvraj Jain

School of Natural Sciences

# Contents

**Word count**: 16503

# List of tables

# List of figures

# Abstract

This thesis aims to set forth the fundamental differences in the design methodology and system engineering of Nuclear Space Power (NSP) reactor and electrical generation systems versus terrestrial designs.

We begin by comparing NSP with Solar Photo-Voltaic (SPV) systems and their evolution in space, intending to identify and justify urgent and necessary applications of NSP generation. Then, we briefly review data on fuel forms and reactor materials, eliminating materials unsuitable for thermal spectrum reactors. Noting that heavy-duty materials may serve as fuel cladding, we discuss the reactor costs, mass, longevity and ease of manufacture. After that, we develop simple thermal hydraulics models of a Pin-in-Cell fuel element and discuss reactor coolant selection. Introducing our rudimentary heat engine models of the Brayton and Rankine cycles, we derive the mathematics describing the system-wide behaviour of a Brayton and Rankine cycle coupled to a radiator. Our insights from thermodynamic and thermal hydraulic analysis lead to nuclear engineering concepts that assist with building a working reactor. We design parametric simulation models using OpenMC's Python API, providing us with the optimum Moderator to Fuel (MF) volume ratios, MF mass ratios, and 3D reactor core data for high-temperature monolithic and composite hydride moderators.

Herein, we also demonstrate a novel NSP system design approach where regulatory justification, logistics and spacecraft thermal design principles are exploited to enforce fundamental constraints on the NSP system design. The NSP system design workflow we adopt relies on open-source, easy-to-use and computationally inexpensive software. Ultimately, we aim to provide a solid introduction to the subtleties of designing a nuclear power system to operate for long periods in space while being compact, lightweight and relatively inexpensive.

## Declaration of originality

I hereby confirm that this dissertation is my own original work unless referenced clearly to the contrary, and that no portion of the work referred to in the dissertation has been submitted in support of an application for another degree or qualification of this or any other university or other institute of learning.

## Intellectual property statement

i The author of this thesis (including any appendices and/or schedules to this thesis) owns certain copyright or related rights in it (the "Copyright") and s/he has given The University of Manchester certain rights to use such Copyright, including for administrative purposes.

ii Copies of this thesis, either in full or in extracts and whether in hard or electronic copy, may be made *only* in accordance with the Copyright, Designs and Patents Act 1988 (as amended) and regulations issued under it or, where appropriate, in accordance with licensing agreements which the University has from time to time. This page must form part of any such copies made.

iii The ownership of certain Copyright, patents, designs, trademarks and other intellectual property (the "Intellectual Property") and any reproductions of copyright works in the thesis, for example graphs and tables ("Reproductions"), which may be described in this thesis, may not be owned by the author and may be owned by third parties. Such Intellectual Property and Reproductions cannot and must not be made available for use without the prior written permission of the owner(s) of the relevant Intellectual Property and/or Reproductions.

iv Further information on the conditions under which disclosure, publication and commercialisation of this thesis, the Copyright and any Intellectual Property and/or Reproductions described in it may take place is available in the University IP Policy (see `http://documents.manchester.ac.uk/DocuInfo.aspx?DocID=24420`), in any relevant Dissertation restriction declarations deposited in the University Library, and The University Library's regulations (see `http://www.library.manchester.ac.uk/about/regulations/_files/Library-regulations.pdf`).

## Acknowledgements

# 1 Justifying Nuclear Space Power Generation

Before we begin discussing and analysing what a Nuclear Space Power (NSP) system should be and how it should function, it is instructive to look outside the field of nuclear engineering and peer into the competition. There is little debate in the literature that high electrical power generation in space is the domain of two technologies: Solar Photo-Voltaics (SPV) and nuclear fission reactors [1]. Currently, SPV dominates the market, and there is a growing push in the aerospace community to phase out radioisotope thermal generators (RTG) [2]. The Juno mission to the Jovian system utilised solar panels as a proof-of-concept to deliver 400 We (watt electric) [2]. Future missions to Jupiter, such as the 2024 Europa Clipper, continue that trend, marking an end of nuclear-powered platforms to explore the outer solar system. Shortages of 238-Pu and regulatory hurdles have led to mission cancellations where RTGs were mission critical [3].

NSP systems for the Artemis program have been qualified for flight, though not launched [4]. They are sub-10 KWe Sterling cycle fast reactors and are meant to be lightweight and deployed into a 10-unit redundant network to power the planned lunar outpost near the Lunar South Pole [4]. So far, space platforms have required sub-KWe power levels, which SPV systems provide efficiently, even while operating in Jupiter or Saturn orbit [2]. At these power levels, NSP systems are impractical. The International Space Station (ISS) has the most extensive SPV system built in space, generating 117 KWe. Life support systems, battery arrays, and computing and communications infrastructure [5] consume most of this power. If one assumes that the ISS is the limit of SPV systems engineering, NSP systems should deliver more than 100 KWe to be competitive. However, we can refine that estimate by considering the power-intensive subsystems used in space platforms. In the coming chapter, we briefly review the factors that inform power system design in space, namely, the power-consuming subsystems, the SPV power generation technology and the expectations of the aerospace community. After this review, we select and justify a niche where NSP systems fit and conclude with a set of challenges which need to be accounted for when designing any NSP system.

## 1.1 Power Requirements for Electricity and Propulsion

The International Space Station (ISS) generates a maximum of 117 KWe [5]. Astronauts utilise this electrical generation to survive and conduct scientific studies. An equivalent NSP system would present a radiation hazard to astronauts unless it uses heavy radiation shielding. Generally, an NSP system designed for servicing crewed missions shall face stringent radiation shielding requirements. This situation includes systems designed for Lunar or Martian colonies. Given those disadvantages and risks of local site contamination in case of an accident, there is no clear consensus ruling out SPV systems with lightweight lithium batter-

ies in exchange for a mass penalty [1].

On the other hand, high-power orbital systems which operate autonomously stand to benefit from NSP systems. In the absence of humans, spacecraft power consumption comprises communications systems, thermal management and, more recently, electric propulsion systems. Electric propulsion systems would represent a significant power-consuming subsystem in the future. [6] performs a detailed analysis of electric propulsion thrusters while considering power, system mass and system redundancy requirements. In the near future, low-power thruster subunits of 5 to 8 kilowatt electric (KWe) assembled in groups of 4 or 5 would result in a single fault-tolerant propulsion system consuming less than 50 KWe [6]. These power and redundancy specifications are meant for uncrewed spacecraft capable of cargo hauling or deep space exploration. Crewed missions require double redundancy, pushing up costs and mass. [6] presented a 400 KWe system with 13 to 18 KWe subunits for crewed deep space exploration. NSP reactors are uniquely suited to such missions due to their long duration and resistance to environmental damage due to space debris or ambient radiation.

Considering the ISS, the Artemis colony and future electrically powered and propelled spacecraft, there seems to be a demand for 100 KWe class power generation systems for the foreseeable future.


## 1.2  State of the Art of Spacecraft Solar Power and Thermal Systems

Solar Photo Voltaic (SPV) panels have been used in spacecraft since the dawn of the semiconductor age in the late 1960s. They are lightweight, affordable, and commercially available, and advances in semiconductor science have enabled them to grow more efficient at producing electricity. Currently, spacecraft utilise multi-junction silicon SPV panels [2] with a typical conversion efficiency of 33 %. A 100 KWe system would only weigh 2000 Kg [2]. Advances in technology would increase efficiencies to 36 % and reduce a 100 KWe system's mass to 500 Kg in the near term. These specifications have prompted mission designers to favour SPV systems even for deep space missions where the solar intensity approaches 4 % of the value in Earth orbit [2].

Further, SPV systems do not intrinsically generate waste heat and have no moving parts, reducing component-level failures. The aerospace community strongly prefers SPV systems because of those characteristics. Figure 1 shows a recent SPV development roadmap released by NASA. Note that NSP systems for scientific missions are not considered. Only missions to the outer planets beyond Saturn are slated to require an RTG. Figure 1 provides context to the NSP system designer of SPV systems' impressive and growing capabilities.
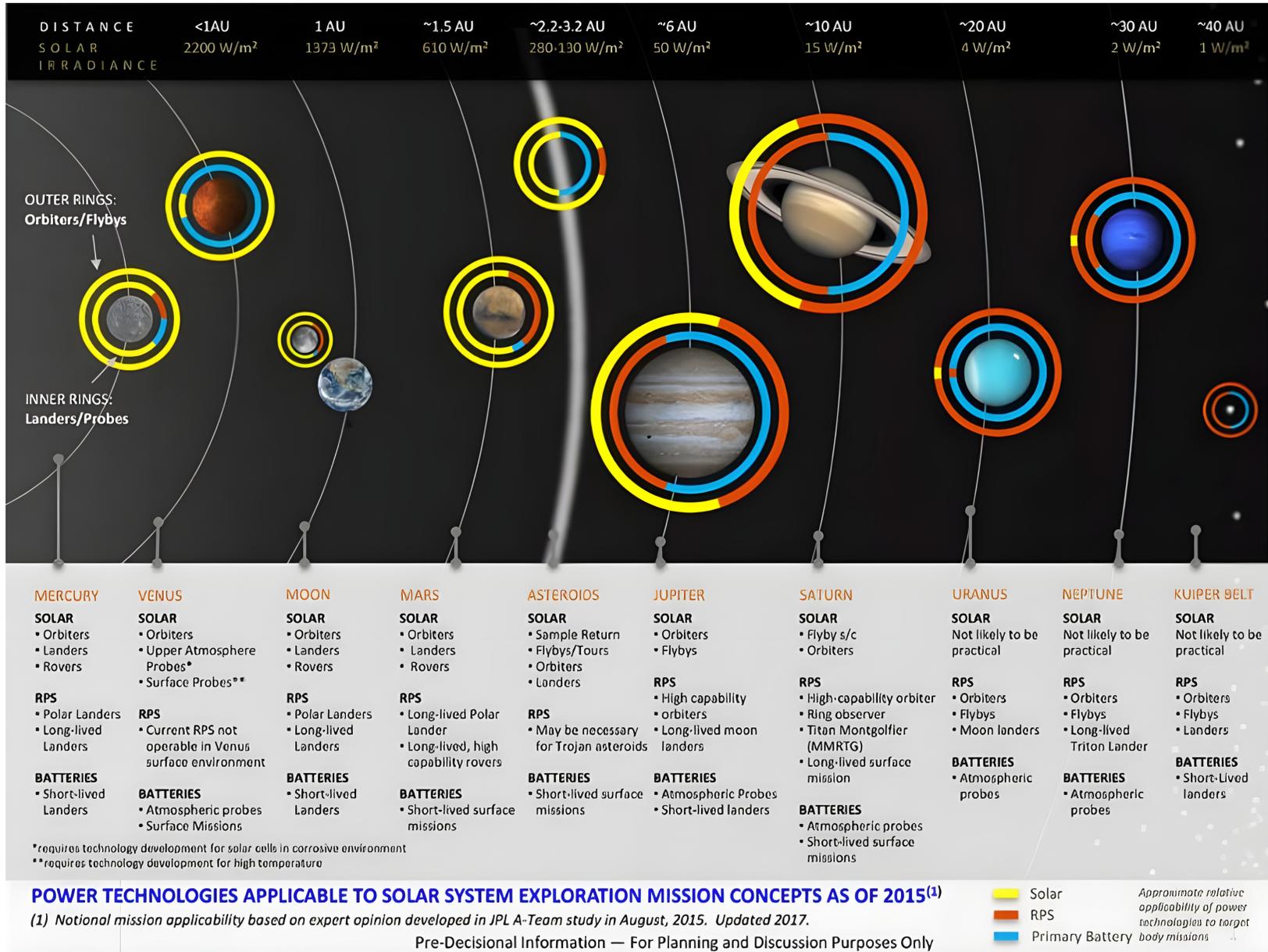
**Fig. 1.** Current and Future Applications of SPV and NSP Generation in Space [7]

However, an SPV array to generate 100 KWe would have some issues with deployment and space debris impacts due to its large surface area [8]. Further, SPV systems require a power storage system onboard to provide continuous power [1]. Unexpectedly, sunlight and illumination are not SPV systems' only environmental hurdles. Every celestial body in the solar system has a unique chemical and plasmonic environment in its orbit, and spacecraft utilising SPV panels must ensure that radiation damage, plasma sputtering and corrosion, and extreme operational temperature do not render them unusable [2]. Therefore, it seems that the cost of developing custom SPV technologies would not be reasonable once interplanetary traffic density exceeds its current limit of 2 spacecraft per decade. NSP systems are independent of the environment, enabling them to be modularised and fitted into any spacecraft regardless of destination, enabling a cargo spacecraft to haul goods to the Moon, Mars or Jupiter and survive in their varied space environments. Radioisotope thermal generator designs successfully exploit that opportunity. However, NSP designs in the past have taken a different approach, designing a spacecraft around the reactor concept and then assigning missions to it, forfeiting the modularity advantage.

Additionally, there is little knowledge of rejecting large heat loads at high temperatures in space. The state-of-the-art thermal management is geostationary communication satellites that reject around 12 KW of thermal energy (KWth) at around 400 K [9]. Dynamic heat pump systems with single and two-phase coolant have recently been considered but have not yet seen deployment [9]. This state-of-the-art is incompatible with a 100 KWe class NSP system. Past NSP systems servicing spacecraft have required vast 100 m$^2$ class radiator arrays to reject the waste heat [10]. These radiators face similar environmental damage compared to SPV panels. To design an NSP system that plays to the technology's strengths, radiator mass, cost, and area should be less than the equivalent SPV system's panels. While spacecraft thermal engineers are familiar with heat pipe radiators [11], few studies survey their cost and mass in relation to an equivalent SPV array. Furthermore, there is very little work on radiator materials and alloys used for rejecting heat at high temperatures, which hinders the development of practical NSP systems that provide a reasonable alternative to SPV systems.

## 1.3 Comparing Nuclear with Solar

Table 1 summarises the discussion so far. SPV systems have a range of advantages and are already mature technology. They are well suited to the sub-KWe spacecraft currently being designed and developed. One can also see that there is no sense of urgency in the market; for example, if a scientific mission to Neptune is only possible with an NSP system, it is likely to be scrapped as scientific missions are neither urgent nor necessary. However, the situation is due to change with the introduction of crewed colonies on the Moon and Mars. NSP systems that outperform equivalent SPV systems intended to service human colonies

**Table 1.** Comparison of High Power Generation Systems in Space

| Nuclear | Solar |
|---|---|
| Nascent | Mature |
| Unknown scope for fundamental technology development | Ample scope for solar cell improvement |
| Requires dense and expensive materials | Silicon is light and inexpensive |
| Volumetrically compact | Large panel arrays are common |
| Independent of space environment and modular | Sensitive to ambient radiation, plasma, debris and temperature |
| Requires heat rejection | Radiator free |
| Ultra-long life | Panels degrade year on year |

shall be developed to maturity once astronauts rely on them for survival. Fortunately, as the ISS shows [5], crewed spacecraft require 100 KWe class power generation, where SPV systems struggle without constant maintenance. SPV panels are also vulnerable to space debris and dust [8], making the Lunar surface [2] a challenging environment without human maintenance. One can see a clear trend. NSP systems that require minimal maintenance and are autonomous can compete with SPV systems in the 100 KWe class range.

After discussing the state-of-the-art, it seems clear that NSP system designs should be compact and lightweight. An equivalent SPV system design should be referred to whenever possible during design so that radiator masses and sizes are kept in check. Finally, NSP systems should press their advantage of modularity and robustness, anticipating operation in a diverse range of space environments that no single SPV panel design can manage [2]. The designer can maximise this advantage by developing a design workflow which creates an NSP reactor design starting from a given spacecraft design and a preset mission.

Finally, the designer must consider the logistics and regulations of transporting the reactor core to the launch site and space as they are non-trivial [12]. Here, we suggest that the reactor core radius is less than 60 cm so that the core can be transported inside spent fuel casks used for terrestrial PWR plant radioactive waste storage [13]. The mass of the NSP system should be well below 8000 Kg, the typical payload limit of modern heavy-lift rockets [14]. The situation where an equivalent SPV system would have foregone the multiple launches, on-orbit assembly and specialised transport to the launch site required by an NSP system should not arise.

## 1.4 Potential Applications of Nuclear Power Reactors in Space

The final step in justifying nuclear power reactors in space concerns the question of urgency and necessity. Public perception against nuclear reactors does not spare those designs that would never be operated on Earth [15]. The expansive costs of nuclear hardware and

radiation safety issues make it challenging to justify NSP systems, especially for crewed missions, where their power generation capabilities are most helpful. Private communication with experts in the aerospace community has led to the following possible applications of NSP systems that are adequately justified.

Nuclear communications infrastructure in deep space is not a novel concept [16]. However, up to this point, it has failed to pass the litmus test of urgency and necessity. If sizeable colonies are established on the Moon or Mars in the coming decades, they would require high bandwidth communications to support astronauts' basic quality of life. Thus, spacecraft in geostationary orbit fitted with NSP generation capable of terabit scale transmission would support essential operations on off-planet colonies. The cost of establishing a high-bandwidth deep space network and the required network reliability justifies nuclear data relays designed to operate continuously and autonomously for at least 10 years. There is also interest in developing high-powered electric propulsion systems for space tugs for cargo hauling [17]. Again, this infrastructure is only helpful if colonies requiring reliable and fast interplanetary transport of goods are established. NSP systems are suited to this work as they can operate independently of the space environment and produce the required power levels for redundant electric propulsion systems [6]. It seems that while necessary, this application is not urgent. Other concepts may deserve study to understand if they are necessary and urgent.

Given that nuclear data relays seem to be the most urgent and necessary application of NSP systems, we can complete a set of specifications typical of a geostationary data relay satellite designed to provide high-speed internet to colonies on the Moon or Mars [18]. Note that the state-of-the-art telecom satellite in geostationary orbit operates at the 10 KWe class [9]. An NSP system would be economical if the satellite could utilise 100 KWe of constant electrical output. Here, we assume the planar radiators are non-deployable and mounted on the four lateral faces of a cuboidal geostationary satellite bus [18]. Table 2 provides the specifications used throughout the remaining chapters to illustrate the applications of the data and insight presented to a practical problem. The mass and size of the reactor are defined somewhat arbitrarily to stay within the limits of current heavy lift launch vehicles [14] and the optimum geostationary orbit satellite bus [18].

## 1.5 Key Challenges: Technical, Economic and Political

This introduction to our work intended to compare and contrast NSP systems with their SPV counterparts to find a niche of applications where the deployment of NSP systems was adequately justified. The review concluded that 100 KWe class power generation systems are in current demand. Further, NSP systems are well suited to uncrewed missions requiring long-term, autonomous operation in various space environments. We identified various technical challenges:

**Table 2.** Targeted Specifications for NSP System Powered Communications Relay

| NSP System Parameter | Target Specification |
|---|---|
| Radiator Height | 3.5 m |
| Radiator Width | 1.5 m |
| Number of Radiators | 2 |
| Number of Redundant Radiators | 2 |
| System Lifetime | 10 years |
| Power Output | 100 KWe |
| Maximum Reactor Core Mass | 2500 Kg |
| Maximum Reactor Core Radius | 0.6 m |

- Hard limit of 8000 Kg on the NSP system mass

- Soft limit of 60 cm on the NSP reactor core radius

- Lack of adequate knowledge and testing of high heat rejection systems operating at high temperature

In addition to those constraints, we selected nuclear data relay telecom satellites as a potentially urgent and necessary application of NSP systems. We used that premise to set up target specifications for the NSP system, chiefly the available radiator area on the satellite bus and the spacecraft's lifetime.

Unlike SPV systems, NSP systems carry significant economic and political implications. From a technical perspective, the 100 KWe class is the minimum where NSP systems begin to compete with SPV systems. However, a detailed mass-cost analysis and consistently improving solar cell technology may push that higher. NASA has published [12] extensive nuclear reactor design and operational guidelines to ensure compliance with safety regulations that we recommend NSP system designers study. There is a legislative and regulatory vacuum concerning nuclear reactors in space, and it is difficult to predict how the legal framework would evolve in the coming decades. Similarly, the economics of NSP systems are in flux due to this power generation option's high uncertainty and low technical maturity. In the end, however, there is no debate that humanity shall come to rely on nuclear technology to spread across the solar system while preserving a connection with Earth and a high quality of life.

# 2 Reactor Materials for Nuclear Space Power Reactors

In this chapter, we take our first steps toward designing an NSP reactor. Chapter 1 presented justification for deploying NSP systems for nuclear data relays and practical considerations that had led to constraints on reactor power output, lifetime and size. Therefore, we now know what the NSP system must do and what sort of mission it must support. This chapter briefly reviews materials a designer could use to build a reactor. For a thorough review, the reader is directed to [19] and [20]. This exercise would create another set of performance constraints: material temperature limits, availability and costs. The review must also account for the thermal neutron absorption characteristics of the selected materials.

This work assumes a thermal neutron spectrum for the coming discussion, as neutron absorption is most substantial in the thermal and epi-thermal neutron energy range. Simultaneously, reactor designers should note that harder neutron spectrums would require materials more resistant to radiation damage, which we do not consider further in this thesis. Initially, we looked through the IAEA Thermophysical Properties of Materials for Nuclear Engineering handbook [21] and NSP systems literature [20] to create a tentative list of materials. This list included nuclear fuel, fuel cladding and general structural materials. There is a significant overlap between the fuel cladding materials and the general structural materials. As noted before, there is very sparse knowledge of high-temperature radiator materials. However, [22] provides a starting point.

Once we compiled the preliminary list of materials, the study moved to investigate basic materials compatibility in the expected operational environment. Operating pressures of gas-cooled NSP systems in the literature are around 2 MPa [23], but temperatures vary widely between particular designs. We assumed that a maximum temperature of 2000 K was conservative. Given this reference operational environment, one can use chemical thermodynamic equilibrium software to predict if a chemical reaction between two materials is thermodynamically favourable. This method has significant drawbacks, chiefly that it does not consider chemical kinetics and reaction rates. Given the scope of this thesis, detailed chemical kinetics simulations or experimental characterisation was not possible. Therefore, we used the freely available online software Fact-Web [24] to create a rough picture of materials compatibility at 2 MPa and 2000 K. Interactions of interest included the fuel-clad interaction, clad-coolant interaction and the fuel-moderator interaction; only the first two are presented here.

## 2.1 Nuclear Fuel

The IAEA handbook [21] provides a rich set of properties data to compare and contrast nuclear fuel materials. It also eliminates novel fuel forms that are less studied from consideration in this thesis as we did not perform a further literature study on novel fuel forms with a

**Table 3.** Thermophysical Properties of Uranium Ceramic Fuels

| Property | UN | UC | UO$_2$ |
|---|---|---|---|
| Total Density at 273 K (Kg/m$^3$) | 14420 | 13630 | 10963 |
| Uranium Density at 273 K (Kg/m$^3$) | 13619 | 12970 | 9664 |
| Melting Point (K) | 3123 | 2793 | 3120 |
| Thermal Conductivity at 2000 K (W/mK) | 27.20 | 22.76 | 2.24 |
| Heat Capacity at 2000 K (J/KgK) | 305 | 297 | 542 |

lower probability of near-term application. Table 3 summarises the data presented in [21] on UO$_2$, UC, and UN.

At a glance, we can see that UN and UO$_2$ stand out. UO$_2$ is well-studied, with decades of commercial experience and has a high melting point [19]. However, it has two significant drawbacks. One, it has a thermal conductivity equal to a tenth of the other fuel forms at 2000 K. Next, UO$_2$ incorporates a lesser amount of uranium per cubic meter than its counterparts. Its high melting point and higher heat capacity partially ameliorate the first disadvantage. However, there are no solutions to the low uranium density, which leads to a greater reactor mass. NSP reactor designers may still consider UO$_2$ for nuclear fuel because it is commercially available and has a vast application legacy.

Comparing UN and UC, UC seems like a weaker contender. A review of UC thermophysical properties states that it is harder to manufacture and offers fewer advantages over UO$_2$ than UN [25]. While UO$_2$ does not interact with most materials at 2 MPa and 2000 K, UC has been known to carburise cladding materials, leading to cladding embrittlement failures [26]. Fact-Web calculations show that UC decomposes to molten U carbonising titanium, chromium, zirconium, and niobium, common elements of nuclear reactor structural alloys. [25] also talks about the variable stoichiometry of UC and the difficulty of obtaining pure UC in a given sample. This chemical behaviour means UC is also unstable in contact with graphite, a common nuclear material. For these reasons, UC is less studied for future terrestrial reactor systems and past NSP systems. We conclude that UC is not a practical fuel form for NSP reactors compared to UN.

Past NSP concepts, such as the SP-100 [27], have worked with UO$_2$ and UN. The findings presented here reinforce those fuel form choices, and there is a strong consensus in the literature which prefers UN fuel. However, engineering materials decisions are rarely straightforward. UN is an excellent fuel form, but our Fact-Web calculations showed that it is unstable when in contact with zirconium and titanium, vital components of high-strength structural alloys. Metal nitriding is a surface process, and nitride moieties are not as mo-

bile as carbon in alloys. The immobility of nitride means embrittlement is less probable with UN than with UC [26]. Long-term testing for NASA's SP-100 nuclear electric propulsion program revealed that refractory metals such as niobium, tungsten and rhenium are compatible with UN [27]. Fact-Web calculations suggest standard steels are also compatible, which is supported by the literature [26].

However, UN brings its own set of engineering problems. At higher temperatures, UN tends to decompose into liquid uranium and nitrogen if an appropriate level of nitrogen partial pressure is not present [21]. This behaviour puts additional stress on the fuel cladding as it must contain gaseous fission products and nitrogen under pressure. The high melting point of UN is also somewhat misleading. When irradiated in a reactor, UN pellets undergo extensive swelling at temperatures above 1600 K, limiting nominal operational temperature compared to $UO_2$ [28]. Finally, there is substantial debate in the literature concerning the thermal neutron absorption of natural nitrogen, which produces long-lived radioactive 14-C in situ [29]. The neutronic impact of natural nitrogen compared with enriched nitrogen is well known but not well studied quantitatively. The economic case for nitrogen enrichment is unclear, with no consistent supply nor demand, and so far, all UN fuel testing campaigns have considered only natural nitrogen [19]. In later chapters of this thesis, we shall further investigate the effects of nitrogen enrichment in UN fuel.

## 2.2  Fuel Cladding and Structural Materials

The nuclear fuel cladding is structural in nature. It holds volatile fission products under pressure and supports the fuel pellet stack. Further, the coolant subjects the fuel cladding to corrosion under extreme irradiation. It is reasonable to assume that if a structural material can fulfil the role of cladding the nuclear fuel pellets, it would be adequate elsewhere. Widespread use of such heavy-duty materials in the NSP system would increase costs and mass, leaving the door open to design optimisation, a process unique to each NSP system's design. This section explores heavy-duty alloys compatible with common NSP system coolants and fuel forms.

Structural alloys are generally divided into alloy steels and refractory alloys [21]. The IAEA handbook provides many thermophysical properties data on pearlitic, martensitic and austenitic steels but notes that their maximum operating temperature is around 1073 K [21]. The SP-100 program used rhenium and Nb-1Zr alloys to line the UN fuel pellets [27]. Some designers have also considered Mo-14Re [20]. One can see that there is no strong preference or consensus in the literature on which materials are best suited to NSP systems.

Fact-Web calculations show that standard steels and high-temperature heavy metals, also known as refractory alloys, are primarily compatible with UN and $UO_2$. NSP systems designers may not select refractory alloys over steels because they are denser and heavier.

**Table 4.** Commercially Available High-Temperature Structural Alloys for NSP Reactors

| Property | MA956 ODS | Mo-TZM |
|---|---|---|
| Density at 298 K (Kg/m$^3$) | 7250 | 10160 |
| Melting Point (K) | 1755 | 2896 |
| Thermal Neutron Absorption (b) | 2.56 | 2.48 |
| Allowable Stress at 1400 K (MPa) | 15 | 50 |
| Allowable Stress at 1600 K (MPa) | - | 25 |

However, refractory alloys typically also have higher ultimate and tensile yield strengths [20], allowing components to reduce alloy usage. Another issue with refractory alloys containing tungsten, tantalum, hafnium or rhenium is that heavy metals absorb thermal neutrons effectively, which is not a problem with steels. These interdependent considerations complicate structural material selection. Therefore, we eliminated cladding and structural materials using a combination of neutronics and availability criteria. Table 4 illustrates commercially mass-produced structural alloys which can operate beyond 1100 K, weakly absorb thermal neutrons and behave well in contact with sodium or helium-based reactor coolants [20].

Table 4 does not contain some common materials encountered in the NSP systems literature [20]. We excluded hafnium, rhenium, tantalum and tungsten containing alloys because they strongly absorb thermal neutrons [30]. Further, Nb alloys fail to operate beyond 1100 K, while oxide dispersion strengthened (ODS) steels can operate at 1400 K [20]. Of the remaining alloy choices, searching for vendors yielded only sellers for MA956 ODS and Mo-TZM alloys, indicating that the other alloys are not as readily available on the open commercial market. Although our demanding elimination criteria have eliminated most of the materials under consideration, they have also illustrated the legacy NSP system designer's dependence on speciality, non-commercial alloys, contributing to the costs and technical risks associated with developing and testing an NSP system.

## 2.3 A Note about Moderators, Reflectors, Absorbers and Radiator Materials

As we wrap up this brief review of reactor materials, let us discuss the other materials in a nuclear reactor core. So far, we are targeting a thermal neutron spectrum in the NSP reactor core. Therefore, neutron moderator materials, which reduce the kinetic energy of fission neutrons, are integral to the reactor design. Our framework for eliminating materials eliminated nearly all moderator materials currently used in the nuclear industry [21]. Pressurised water systems cannot operate beyond 1100 K without extremely bulky plumbing, and graphite has poor neutron stopping power, resulting in large reactor core volumes [21]. Moderating

materials which survive high temperatures and have a high neutron stopping power have only recently been subjected to study [31]. The concept of composite moderators is also under study for terrestrial nuclear microreactors [32]. For these reasons, we shall investigate moderators in their own dedicated chapters later.

Beryllium and BeO have a history of preference by the nuclear engineering community for fabricating neutron reflectors. Beryllium and its alloys have poor irradiation resistance due to helium bubble formation and suffer from low operational temperatures and low ductility [33]. Hence, beryllium alloys are not suited to NSP systems. However, BeO has the appropriate properties for a reflector. The NSP reactor designer is left to decide if they require a reflector for their design and which material they use. We do not have any generic recommendations, as every specific design would have its own tradeoffs. For similar reasons, this thesis does not cover reactor control system absorbers such as boron carbide or Hf alloy.

Finally, there is the issue of turbomachinery and radiator materials. As noted in Chapter 1 and this chapter, there has been little study in this area. Generally, NSP system turbines, compressors and radiators can also use reactor cladding and structural alloys selected for NSP fuel cladding. Radiators would be subjected to a wide range of space environments, and more study is required to determine if reactor structural alloys could survive the plasmonic environments around various celestial bodies. Again, we leave the NSP reactor designer to decide if more common and less heavy-duty materials such as SS 316, Ti 4Al1V or others suit their design and save on costs.

In the next chapter, we take a final detour before heading into NSP reactor engineering to discuss heat engines, operational thermal limits, and heat rejection in space. Our review of reactor materials has left us with a list of potential materials and their operational limits. The coming chapter shall further refine our material choices and, in the process, provide us with our first real insight into NSP systems engineering as a discipline.

# 3  Heat Engines for Power Conversion in Space

In this chapter, we get on to thermal engineering. Chapters 1 and 2 covered what the basic NSP system specifications might be and what materials could be used for the design. Here, we combine that knowledge with the fundamental thermal and thermal hydraulics concepts to obtain a clear, high-level picture of NSP systems. We study the possible options for converting and rejecting large heat loads into space given the constraints of the spacecraft and its mission. This chapter provides the first valuable insights into NSP systems engineering as a standalone discipline as we cover how one can design a simple, redundant and robust NSP system.

As a reminder, we selected the nuclear data communication relay as a potentially urgent and necessary application of NSP systems. We determined that a 100 KWe class system would fit the application. The mission determined the optimum size of the spacecraft bus [18] and the area available to mount static radiators. We assume space is available for two planar high-temperature radiators on the lateral sides of the cuboidal spacecraft bus. The remaining two sides feature backup radiators for single-fault redundancy expected of uncrewed missions [6]. Surprisingly, this level of information is enough to analyse and compare heat engines for the NSP system.

## 3.1  Choice of Heat Cycles and Reactor Coolants

[19] and [34] review and compare power conversion systems for high power generation systems in a level of detail not possible here. In summary, Brayton and Rankine cycles offer an efficient and scalable means to convert thermal power to electricity. Other systems, such as direct thermoelectric conversion or the Sterling cycle, work well for 10 KWe class systems but fail to scale further [34]. Direct thermoelectric conversion is inefficient, and higher power systems ultimately reject a vast amount of the heat they produce, requiring larger radiators. Sterling cycles, preferred by the aerospace community for reliability and efficiency, fail to handle high power flow rates due to a lack of flowing coolant, ultimately relying on heat pipes to function [34].

Legacy NSP systems strongly prefer gas-cooled reactors deployed with a Brayton Cycle [23]. Advantages include mass savings, decoupling of reactor neutronics from thermal hydraulics and extensive aerospace engineering heritage with gas turbines and centrifugal compressors. More fundamentally, though, Brayton cycles seem ill-suited to the space environment. Legacy NSP designs rarely considered redundancy and did not consider the hard 8000 Kg mass limit in this work. Without heat pipe radiators, the gas coolant makes inefficient use of the radiator area as its temperature reduces while it passes through. In terrestrial settings, heat rejection is a linear function of temperature, but heat rejection is proportional to the fourth power of temperature in space. Furthermore, the gas coolant has an appreciable

temperature gradient from the bulk of the fluid to the radiator tube wall, further reducing the overall radiator temperature. With its isothermal heat injection and rejection, the Rankine cycle is ideal for maximising space radiator utilisation and minimising temperature gradients in the reactor core and radiator tubing [35].

A detailed analysis of heat cycles, including complex systems with recuperators and regeneration, is published for solar concentrator power systems in space [35]. However, they do not use working fluids or temperatures appropriate to nuclear systems. [35] concludes that the Rankine cycle possesses the best thermal efficiency, followed by the Brayton and the Sterling cycle. However, choosing cryogenic fluids for the working fluid leads to extremely low heat rejection temperatures and impractically large radiator areas [35]. Surprisingly, NSP systems designers rarely approach thermal management first and then design the reactor based on the limitations of the heat cycle employed and the available radiator surface area.

In any case, we demonstrate the utility of the thermal first approach in this chapter with two heat cycles: a Brayton cycle with HeXe gas coolant and a Rankine cycle with sodium coolant. There is a consensus in the literature on NSP systems that use the Brayton cycle that doping helium gas with xenon is required to reduce aerodynamic stresses on the turbine and compressor blades. The reduced stresses lead to more compact turbomachinery, which is also lightweight [23]. In the coming sections, we shall investigate the effects of xenon doping in further detail. A Rankine cycle with sodium coolant is also considered as an alternative to the Brayton cycle. NASA has studied legacy potassium Rankine cycles [35] [19] because of their reduced turbine blade corrosion tendency. However, modern spacecraft thermal management systems extensively use looped heat pipes for rejecting high heat loads [11], and more recently, NSP systems deploy sodium heat pipes [4]. Ultimately, we selected sodium coolant since sodium's thermophysical properties [36] and structural material interaction [37] are much more studied than potassium's in the aerospace and nuclear communities. Looped heat pipe-like systems avoid issues surrounding two-phase flow and boiling in null g entirely [11], enabling a boiling-free Rankine cycle with an annular flow regime in the condenser cum radiator.
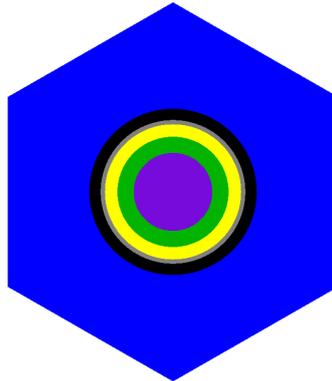
**Fig. 2.** Pin-in-Cell Fuel Element with a Moderator to Fuel Volume Ratio of 5. The blue region is the moderator, the black region is the coolant gas, and the fuel pellet is sectioned into three equal volume regions of different colours in the centre. The fuel cladding is not visible on this scale. This figure is to scale with each edge equal to 15 cm.

Now that the choice of coolants for the heat cycles is clear, we can perform a simple hot-channel thermal hydraulics analysis for heat transfer in the reactor core. These analyses would provide a mathematical framework to constrain the maximum linear power of the fuel pin in the NSP reactor core. For a performance comparison, we use an experimentally tested fuel pin concept [38], a 15.8 mm diameter UN fuel pellet capable of supporting 275 W/cm. As NSP system designers at NASA [4] recommended, we use a simple-to-analyse fuel element design that is also functional. Figure 2 shows the pin-in-cell design considered in this thesis. We believe that the insights from our work should remain largely valid even if the NSP reactor designer is considering more complex fuel element geometry. The model is infinite in the axial

direction. It assumes the moderator hexagonal block surrounding the fuel pin is isothermal with the coolant flowing in the channel. This assumption ignores the power generated in the moderator when it slows down fission neutrons, which is around 1 to 3 % of the total reactor thermal power for thermal spectrum reactors [39]. Lastly, the fuel pellet cladding is 0.5 mm thick MA 956 ODS steel.

## 3.2 HeXe Gas Thermal Hydraulics Model

The properties of HeXe gas coolant are a function of the equivalent molar mass of the coolant [23]. A recent review [40] compares HeXe with pure helium regarding its heat transfer co-efficient (HTC) in similar operating conditions. That work and others in the past [23] define 'similar operating conditions' as equal flow temperature, flow area and molar flow rate. This definition is unusual because nuclear engineers consider mass flow rates in their designs. We created a set of GNU Octave 8.3.0 scripts to calculate the transport properties of HeXe as a function of temperature and molar mass using equations provided in [41]. Then, another script used that data to build G-T tables, which are more familiar to nuclear engineers in the industry using a simplified, steady-state version of the Taylor HTC correlation for low Prandtl number fluids [40]. The simplified version, Equation 1, ignores the effects of the fluid bulk to wall temperature gradient on the HTC and assumes a fully formed flow. The simplification reduces the resulting HTC; therefore, it is a conservative assumption. Appendix B provides links to the GNU Octave scripts.

$$HTC = \frac{k}{D_h}\left[0.023 Re^{0.8} Pr^{0.65}\right] \tag{1}$$

Figure 3 contains the HTC data as a function of the coolant temperature and the mass flux for pure helium and 40 g/mol HeXe, popular with NSP designers in the literature [40]. Multiple studies in the literature show that 40 g/mol HeXe and pure helium have the same HTC [23] [40].

| G (Kg/m²s)/T (K)/HTC (W/m²K) | 100 | 200 | 300 | 400 | 500 | 600 | 700 | 800 | 900 | 1000 | 1100 | 1200 | 1300 | 1400 | 1500 |
|---|---|---|---|---|---|---|---|---|---|---|---|---|---|---|---|
| 400 | NaN | 3724 | 5151 | 6484 | 7751 | NaN | NaN | NaN | NaN | NaN | NaN | NaN | NaN | NaN | NaN |
| 500 | NaN | 3842 | 5314 | 6689 | 7996 | 9252 | NaN | NaN | NaN | NaN | NaN | NaN | NaN | NaN | NaN |
| 600 | NaN | NaN | 5458 | 6870 | 8213 | 9503 | 10750 | NaN | NaN | NaN | NaN | NaN | NaN | NaN | NaN |
| 700 | NaN | NaN | 5585 | 7030 | 8404 | 9723 | 10999 | 12239 | NaN | NaN | NaN | NaN | NaN | NaN | NaN |
| 800 | NaN | NaN | 5697 | 7172 | 8573 | 9920 | 11222 | 12487 | NaN | NaN | NaN | NaN | NaN | NaN | NaN |
| 900 | NaN | NaN | 5799 | 7300 | 8727 | 10097 | 11422 | 12710 | 13966 | NaN | NaN | NaN | NaN | NaN | NaN |
| 1000 | NaN | NaN | NaN | 7415 | 8865 | 10257 | 11603 | 12911 | 14187 | 15434 | NaN | NaN | NaN | NaN | NaN |
| 1100 | NaN | NaN | NaN | 7532 | 9005 | 10419 | 11786 | 13115 | 14410 | 15678 | 16920 | NaN | NaN | NaN | NaN |
| 1200 | NaN | NaN | NaN | 7622 | 9112 | 10543 | 11926 | 13271 | 14582 | 15865 | 17122 | 18356 | NaN | NaN | NaN |
| 1300 | NaN | NaN | NaN | 7674 | 9173 | 10614 | 12007 | 13361 | 14681 | 15972 | 17237 | 18480 | NaN | NaN | NaN |
| 1400 | NaN | NaN | NaN | NaN | 9250 | 10703 | 12108 | 13473 | 14804 | 16106 | 17382 | 18635 | 19867 | NaN | NaN |
| 1500 | NaN | NaN | NaN | NaN | 9376 | 10849 | 12272 | 13656 | 15005 | 16325 | 17618 | 18888 | 20137 | 21367 | NaN |
| 1600 | NaN | NaN | NaN | NaN | 9496 | 10987 | 12429 | 13830 | 15196 | 16533 | 17843 | 19129 | 20394 | 21639 | NaN |
| 1700 | NaN | NaN | NaN | NaN | 9577 | 11081 | 12535 | 13948 | 15326 | 16674 | 17995 | 19293 | 20568 | 21825 | 23063 |
| 1800 | NaN | NaN | NaN | NaN | 9642 | 11156 | 12620 | 14043 | 15431 | 16788 | 18118 | 19424 | 20708 | 21973 | 23220 |
| 1900 | NaN | NaN | NaN | NaN | 9707 | 11232 | 12706 | 14138 | 15535 | 16902 | 18241 | 19556 | 20849 | 22122 | 23378 |
| 2000 | NaN | NaN | NaN | NaN | NaN | 11303 | 12786 | 14227 | 15633 | 17008 | 18356 | 19679 | 20980 | 22262 | 23525 |
| Simplified Taylor Heat Transfer Coefficients for Pure Helium Versus Mass Flux and Flow Temperature (D$_h$ = 2.64 mm) | | | | | | | | | | | | | | | |

| G (Kg/m²s)/T (K)/HTC (W/m²K) | 100 | 200 | 300 | 400 | 500 | 600 | 700 | 800 | 900 | 1000 | 1100 | 1200 | 1300 | 1400 | 1500 |
|---|---|---|---|---|---|---|---|---|---|---|---|---|---|---|---|
| 400 | NaN | NaN | 819 | 1032 | 1233 | 1427 | 1614 | NaN | NaN | NaN | NaN | NaN | NaN | NaN | NaN |
| 500 | NaN | NaN | 843 | 1061 | 1268 | 1467 | 1660 | 1847 | NaN | NaN | NaN | NaN | NaN | NaN | NaN |
| 600 | NaN | NaN | NaN | 1085 | 1297 | 1501 | 1698 | 1890 | 2076 | 2259 | NaN | NaN | NaN | NaN | NaN |
| 700 | NaN | NaN | NaN | 1107 | 1323 | 1531 | 1731 | 1927 | 2117 | 2303 | 2486 | NaN | NaN | NaN | NaN |
| 800 | NaN | NaN | NaN | 1125 | 1345 | 1556 | 1760 | 1959 | 2152 | 2342 | 2527 | 2709 | NaN | NaN | NaN |
| 900 | NaN | NaN | NaN | NaN | 1364 | 1579 | 1786 | 1987 | 2184 | 2376 | 2564 | 2749 | 2930 | NaN | NaN |
| 1000 | NaN | NaN | NaN | NaN | 1382 | 1599 | 1809 | 2013 | 2212 | 2407 | 2597 | 2785 | 2969 | 3150 | NaN |
| 1100 | NaN | NaN | NaN | NaN | 1399 | 1619 | 1831 | 2038 | 2239 | 2436 | 2629 | 2818 | 3005 | 3188 | 3369 |
| 1200 | NaN | NaN | NaN | NaN | 1415 | 1637 | 1852 | 2061 | 2264 | 2463 | 2658 | 2850 | 3039 | 3224 | 3407 |
| 1300 | NaN | NaN | NaN | NaN | NaN | 1654 | 1871 | 2082 | 2288 | 2489 | 2686 | 2880 | 3070 | 3258 | 3443 |
| 1400 | NaN | NaN | NaN | NaN | NaN | 1670 | 1889 | 2102 | 2310 | 2513 | 2712 | 2908 | 3100 | 3290 | 3476 |
| 1500 | NaN | NaN | NaN | NaN | NaN | 1685 | 1906 | 2121 | 2331 | 2536 | 2737 | 2934 | 3128 | 3319 | 3508 |
| 1600 | NaN | NaN | NaN | NaN | NaN | 1699 | 1922 | 2139 | 2351 | 2557 | 2760 | 2959 | 3154 | 3347 | 3537 |
| 1700 | NaN | NaN | NaN | NaN | NaN | NaN | 1938 | 2156 | 2369 | 2577 | 2782 | 2982 | 3179 | 3373 | 3565 |
| 1800 | NaN | NaN | NaN | NaN | NaN | NaN | 1952 | 2172 | 2386 | 2596 | 2802 | 3004 | 3203 | 3398 | 3591 |
| 1900 | NaN | NaN | NaN | NaN | NaN | NaN | 1965 | 2187 | 2403 | 2614 | 2822 | 3025 | 3225 | 3422 | 3616 |
| 2000 | NaN | NaN | NaN | NaN | NaN | NaN | 1978 | 2202 | 2419 | 2632 | 2840 | 3045 | 3246 | 3445 | 3640 |
| Simplified Taylor Heat Transfer Coefficients for 40 g/mol HeXe Versus Mass Flux and Flow Temperature (D$_h$ = 2.64 mm) | | | | | | | | | | | | | | | |

**Fig. 3.** Calculated Heat Transfer Coefficient Values using the Simplified Taylor HTC Correlation

In contrast, our results show that the HTC coefficient of 40 g/mol HeXe for conditions of equal mass flux is nearly a tenth of pure helium. These results highlight the importance of the definition of 'similar operating conditions'. Our script factors in the Reynolds number limits of the Taylor HTC correlation [40], leading to invalid results for certain combinations of G and T. We see that the region of the G-T table with valid results for HeXe does not have valid results for pure helium. At a given flow temperature and flow area, we can define the Reynolds number of the flow as:

$$Re = \frac{MM\dot{N}D_h}{\eta(T)} \tag{2}$$

Where $\dot{N}$ is the molar flux, and $MM$ is the molar mass of the coolant. At conditions of constant molar flux, as assumed in [23] and [40], there is a factor of 10 between the Reynolds numbers of the two coolants, which always places one of them outside the applicability criteria of the Taylor's HTC correlation (1.8E4 < Re < 6E4) [40]. Therefore, one cannot make direct comparisons using the Taylor's HTC correlation.

Besides this subtlety, HeXe at 40 g/mol has a tenth of the heat capacity of pure helium. For a given heat source and temperature difference, the mass flow rate in a helium-powered Brayton cycle is a tenth of one powered by 40 g/mol of HeXe. The reduced mass flow would also reduce the turbomachinery RPM and size, which was the initial argument for doping helium with xenon. A reduction in the turboalternator voltage would accompany a reduction in RPM. However, previous NSP turbine designs operate from 30 to 50 kRPM [42]. The ISS primarily uses 120 to 160 V direct current systems to reduce the cabling size and mass [5], which shows that reducing the turboalternator frequency would have a minimal impact on the resulting voltage from the power conditioning system.

As we show shortly, the mass flow rate reduces to a point where it is debatable if a centrifugal compressor is suitable where positive displacement pumps may suffice. We would also like to point out that since [23], compact high-mass flow pumps for hydrogen have been developed as part of the push toward a hydrogen economy [43], which is noteworthy as hydrogen is more difficult to work with than pure helium. Ultimately, we leave it to the NSP systems designer to decide if they prefer HeXe or pure helium. Here, we continue with 40 g/mol HeXe so that our results stay relevant to legacy NSP designs using HeXe.

Now that the coolant selection is complete, we can direct our attention to thermal hydraulics. Our thermal hydraulics model is split into core pressure loss calculations and radial heat transfer calculations. We set criteria to constrain the mass flow through the coolant channel shown in Figure 2:

$$G_{mach} = 0.3P\sqrt{\frac{\gamma \times MM}{RT_o}} \tag{3}$$

28

$$G_{dP} = \sqrt{\frac{dP}{\frac{fHK_f}{2\rho_o D_h} + 0.5\left[\frac{1}{\rho_o} - \frac{1}{\rho_i}\right]}} \tag{4}$$

$$G_{HTC} = \frac{Re \times \eta(T_i)}{D_h} \tag{5}$$

$$G_{TH} = \frac{q'H}{C_p A(T_o - T_i)} \tag{6}$$

Equation 3 defines the incompressible flow limit of the gas at the coolant channel exit for 0.3 Mach and a given coolant pressure. Equation 4 defines the flow limit for 0.2 MPa pressure loss across the fuel element, accounting for flow friction using the Blasius correlation, form losses and acceleration [44]. Finally, Equation 5 defines the flow limit by setting the Reynolds number to 6E4, the upper limit of Taylor's HTC correlation. Table 5 compares results for a 400 K inlet and 1200 K outlet temperature with an element linear power of 275 W/cm and height of 46 cm. The channel flow area is 0.75 cm$^2$. These numbers are arbitrary and for illustration purposes. Equation 6 provides the minimum mass flux required to remove the heat generated.

**Table 5.** Limiting Mass Flux for Pin-in-Cell Fuel Element with 40 g/mol HeXe and Pure Helium Coolant

| Script Input Parameter | 40 g/mol HeXe | Pure Helium |
|---|---|---|
| Minimum Coolant Inlet Temperature | 400 K | 400 K |
| Maximum Coolant Inlet Temperature | 1200 K | 1200 K |
| Maximum Element Linear Power | 275 W/cm | 275 W/cm |
| Fuel Element Height | 46 cm | 46 cm |
| Coolant Flow Area | 0.75 cm$^2$ | 0.75 cm$^2$ |
| Coolant Channel Hydraulic Diameter | 2.64 mm | 2.64 mm |
| Coolant Molar Mass | 0.04 Kg/mol | 0.004 Kg/mol |
| Flow Reynolds Number | 60000 | 60000 |
| Coolant Pressure | 2 MPa | 2 MPa |
| Maximum Pressure Drop | 0.2 MPa | 0.2 MPa |
| Form Pressure Loss Factor | 1.5 | 1.5 |
| Incompressible Flow Mass Flux Limit | 1551 Kg/m$^2$s | 491 Kg/m$^2$s |
| Taylor's HTC Mass Flux Limit | 753 Kg/m$^2$s | 537 Kg/m$^2$s |
| Pressure Drop Mass Flux Limit | 734 Kg/m$^2$s | 232 Kg/m$^2$s |
| Minimum Mass Flux Limit | 406 Kg/m$^2$s | 41 Kg/m$^2$s |

Table 5 shows the differences between 40 g/mol HeXe and pure helium. The first notable

parameter is the required core cooling mass flow rate. At 41 Kg/m²s, it is unclear if a centrifugal compressor for a helium-powered Brayton cycle is preferable to a positive displacement pump. Table 5 also shows the difference in pressure losses between the two coolants. The ratio between the required mass flux to cool the reactor and the flow pressure drop limit is about 5.65 compared to 1.81 for HeXe, which is equivalent to stating that the actual pressure loss is 3.12 times lower with pure helium. This behaviour has been noted in the literature [40], and HeXe induces significantly higher loop pressure losses than pure helium. We also note that the optimal coolant channel area for 40 g/mol HeXe is close to 0.75 cm² as the pressure drop mass flux limit approaches the HTC Reynolds number mass flux limit. A pin-in-cell fuel element designed for pure helium should also exhibit such behaviour while ensuring incompressible flow. However, the mass flux limit equivalence would occur for a larger flow area, further exacerbating the comparative pressure losses.

Now that we have the flow constraints, we must verify that the fuel pin can support the assumed 275 W/cm linear power in this configuration. We start by integrating the expression for the thermal conductivity of UN between the fuel pellet centreline and the surface [21]:

$$k_f(T) = 1.41 T^{0.39} \tag{7}$$

We have from fundamental heat transfer in a cylindrical heat-generating body [44]:

$$\int_{T_s}^{T_m} k_f(T) dT = \frac{q'}{4\pi} \tag{8}$$

Putting Equation 7 in 8 and solving for the surface temperature $T_s$ yields:

$$T_s = \left[ T_m^{1.39} - \frac{1.39}{1.41} \times \frac{q'}{4\pi} \right]^{\frac{1}{1.39}} \tag{9}$$

Now, we find the radial heat conduction and convection expression for calculating the fuel pellet surface temperature from [44]:

$$T_s = T_b + q' \times \left[ \frac{\ln \frac{r_2}{r_1}}{2\pi K_c(T_b)} + \frac{1}{2\pi r_2 HTC(G, T_b)} \right] \tag{10}$$

We can now equate Equations 9 and 10 to numerically find the linear power of the fuel element, given that the fuel centreline temperature $T_m$ is constrained to 1600 K to reduce UN swelling [28]. The expression for the thermal conductivity of the MA 956 ODS clad, $k_c$, is from [45]:

$$k_c(T) = \frac{T - 273}{60} + 10 \qquad (11)$$

Figure 4 shows the script output for various coolant temperature, $T_b$, and mass flux, $G$, values. The 1200 K coolant temperature curve passes closely above 275 W/cm for the mass flux values predicted by Table 5. As the coolant temperature increases, we expect heat rejection from the radiator to improve. However, thermal hydraulic constraints exist on the fuel element's linear power. Note that for a linear power of 150 W/cm, the allowable maximum coolant temperature is 1400 K. We selected the coolant temperature of 1200 K and flow of area of 0.75 cm$^2$ by manual optimisation of the results of the two Octave scripts, ensuring that the mass flux constraints and linear power requirements are satisfied.
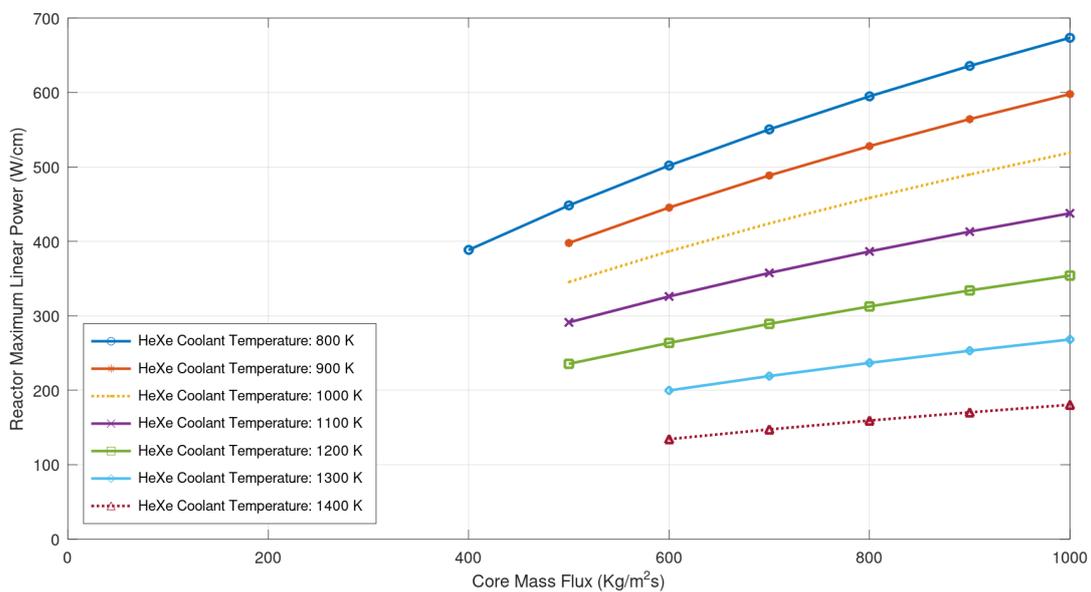


**Fig. 4.** Limiting Linear Power Curves for 40 g/mol HeXe Cooled Fuel Element

These results provide important insight. The space environment prefers high coolant temperature; however, thermal hydraulics prevents a high coolant temperature. Ideally, a higher fuel temperature enables higher coolant temperatures for the same linear power. This behaviour seemingly favours UO$_2$ fuel pellets, which can operate well above the 1600 K limit of UN. Thus, there is a complex interplay of NSP reactor power density, coolant temperature and radiator heat rejection. On closer analysis of these conditions, we found that the actual fuel pellet surface temperature was 1511 K, with the remaining 311 K primarily being dropped across the HeXe coolant gas due to its low HTC. Thus, one wonders how the system's thermal hydraulics would perform if the coolant were isothermal.

### 3.3 Sodium Isothermal Thermal Hydraulics Model

This section repeats the thermal hydraulics analysis for an isothermal coolant evaporating in the fuel element coolant channel. The complex annular flow behaviour is not modelled. A slight modification to equation 10 results in:

$$T_s = T_b + \frac{q' \ln \frac{r_2}{r_1}}{2\pi K_c(T_b)} \tag{12}$$

Here, the coolant temperature, $T_b$, is now the boiling point of sodium at the operating system pressure. We assume that the NSP system designers are flexible with the system pressure and, therefore, consider the temperature the driving variable. Equation 12 assumes that the coolant is isothermal, and the results of solving it are presented in Figure 5.
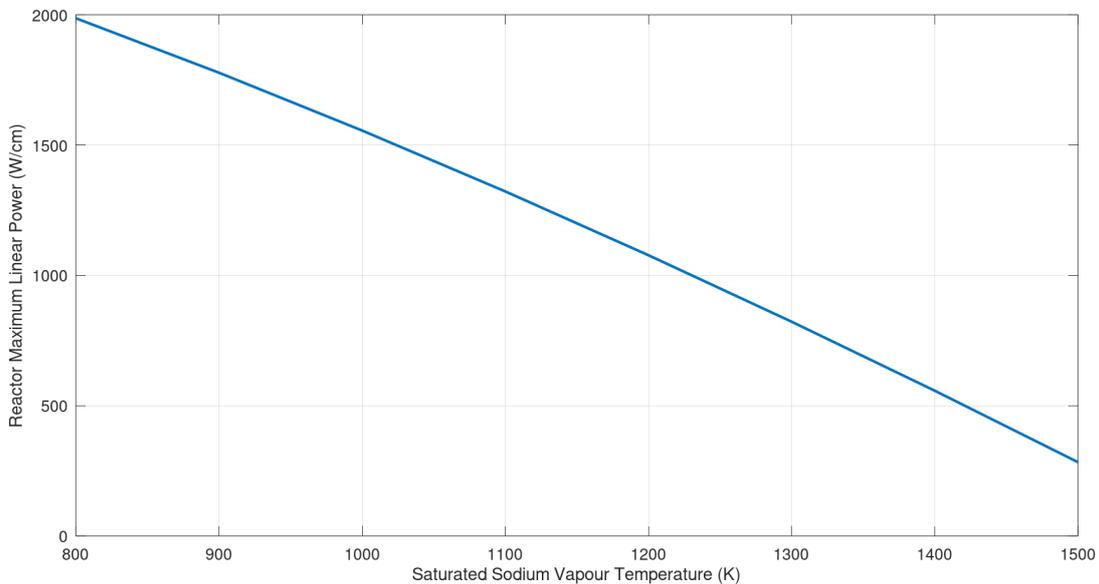


**Fig. 5.** Limiting Linear Power Curves for Sodium Vapourisation Cooled Fuel Element

Figure 5 shows the utility and power of an isothermal system. The allowable linear power for a coolant temperature of 1400 K is now 550 W/cm. A coolant temperature of 1200 K yields 1070 W/cm. The high heat of vapourisation of sodium further reduces the required mass flow rates in the coolant loop and decouples the mass flux limits from core cooling. This system far outperforms the gas-cooled system, and we suggest second-generation NSP systems investigate isothermal cooling for NSP reactor cores using principles similar to looped heat pipes already used in spacecraft [11].

### 3.4 Simple Models of Brayton and Rankine Cycles Operating in Space

Our thermal hydraulics analysis has put bounding limits on the NSP reactor coolant temperature, given a desired reactor power density. In this section, we develop simple mathematical models for the Brayton and Rankine cycles coupled to a radiator for rejecting heat. To simplify the analysis, we assume the radiator tube has no radial temperature gradient. In the interest of brevity, we do not present the complete derivations here. Appendix B contains links to the derivation of all the mathematics for both heat cycles and the GNU Octave scripts for solving the derived equations.
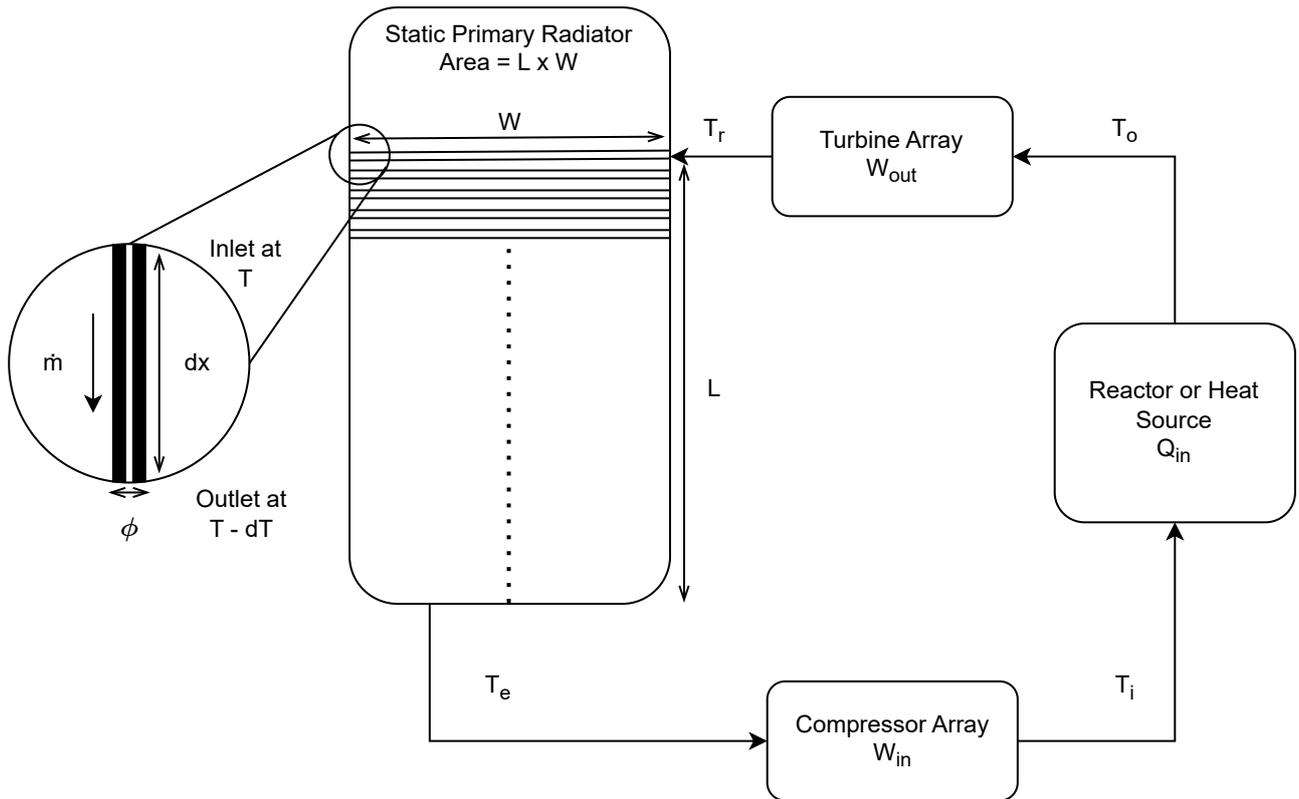


**Fig. 6.** Simple Brayton Heat Engine Coupled to a Radiator

Figure 6 shows the Brayton cycle under consideration. While NSP systems typically contain recuperators and other components [35], we wish only to study the fundamental limits here. Using an energy balance across the heat source, we write:

$$\dot{m} = \frac{Q_{in}}{C_p(T_o - T_i)} \tag{13}$$

Then, consider Figure 6 again. We can write for an infinitesimal section of the radiator using the Stefan-Boltzmann law:

$$dQ = \dot{m}C_p(T)dT = \epsilon\sigma_b\phi(T^4 - T_a{}^4)dx \tag{14}$$

In space, studies [35] [10] usually take the ambient temperature to be around 200 K, significantly less than the coolant temperatures under consideration. Ignoring the ambient temperature and substituting Equation 13 in 14, we can integrate to get:

$$\left[\frac{1}{3T_e{}^3} - \frac{1}{3T_r{}^3}\right]\left[\frac{1}{T_o - T_i}\right] = \frac{\epsilon\sigma_b}{Q_{in}} \int \phi dx = \frac{\epsilon\sigma_b LW}{Q_{in}} \tag{15}$$

The right-hand side integral ultimately yields the radiator area because we assume the radiator is a long coiled tube of apparent diameter $\phi$, leading to $\int \phi dx = \phi NW = \phi\frac{L}{\phi}W = LW$. We see that equation 15 is independent of the coolant properties, which is unintuitive. In fact, coolant properties only determine the mass flow rate in this cycle, with the other properties of interest being solely dependent on temperature. If the compressor must compensate for the pressure loss across the turbine, we get the following:

$$CPR = TPR \times F_p \tag{16}$$

TPR is the turbine pressure rate, CPR is the compressor pressure ratio, and $F_p$ is a factor to account for other pressure losses in the cycle, such as frictional flow loss. We conservatively assume TPR to be 0.5 to ensure the turbine is simple and single-stage. Using the isentropic flow relations [46], we can now relate the turbine inlet temperature to the radiator inlet temperature. Similarly, the radiator outlet temperature and the compressor outlet temperature are related. Substituting in Equation 15, an Octave script can numerically solve for the radiator outlet temperature if the turbine inlet temperature, TPR and $F_p$ are known. We assume a value of $F_p$ of 1.2. Using an energy balance across the turbine, compressor and reactor and assuming a constant value of coolant mass flow rate and heat capacity, we can write:

$$\eta_{th} = \eta_{gen}\frac{T_o - T_r - T_i + T_e}{T_o - T_i} \tag{17}$$

Using the isentropic relations, we get an expression for the conversion efficiency:

$$\eta_{th} = \eta_{gen}\frac{T_o\left[1 - (TPR)^{\frac{\gamma-1}{\gamma}}\right] - T_e\left[\left(\frac{F_p}{TPR}\right)^{\frac{\gamma-1}{\gamma}} - 1\right]}{T_o - T_e\left(\frac{F_p}{TPR}\right)^{\frac{\gamma-1}{\gamma}}} \tag{18}$$

35

**Table 6.** Heat Cycle Analysis Script Input Parameters for Brayton and Rankine Cycle

| Input Parameter | Parameter Value |
|---|---|
| Radiator Height | 3.5 m |
| Radiator Width | 1.5 m |
| Number of Radiators | 4 |
| Number of Redundant Radiators | 0 |
| Radiator Emissivity | 0.8 |
| Turbine Pressure Ratio | 0.5 |
| Pressure Factor | 1.2 |
| Generator Efficiency | 0.9 |
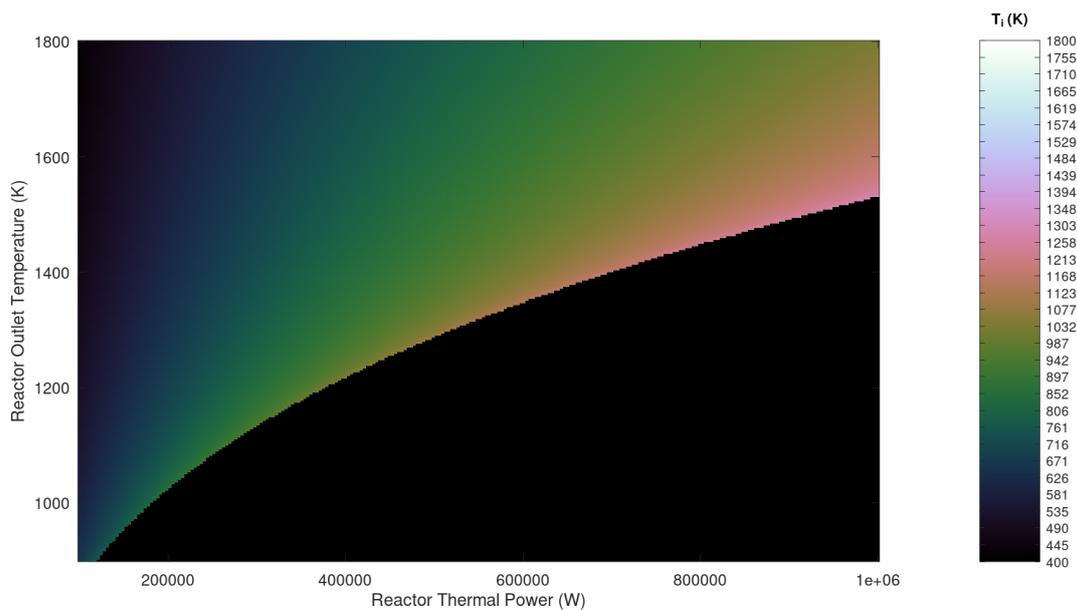


**Fig. 7.** Reactor Inlet Temperature for a Simple Brayton Cycle

Where $\eta_{gen}$ is the alternator or generator efficiency, assumed to be 0.9 [47]. Figure 7 shows a surface plot of the reactor inlet temperature for the script input parameters described in Table 6. Despite the target specifications calling for 2 radiator panels with 2 more for redundancy, we investigate the limits of the systems by using all 4 radiator panels at once.

The black area on the plot's surface is the region where no solutions exist because the radiator cannot reduce the temperature to a level where the reactor inlet temperature is less than the reactor outlet temperature. In other words, the radiator is saturated and unable to reject the heat required to sustain a cycle. Surprisingly, as the reactor outlet tempera-

ture increases, the reactor inlet temperature reduces for a given input thermal power level. This behaviour is because of the heat rejection process's critical dependence on the radiator's local coolant temperature. The same radiator area can reject much more heat, and the net radiator outlet temperature decreases despite the increased inlet temperature. Consequently, the compressor outlet temperature also reduces, and the overall mass flow required to run the cycle drops sharply.
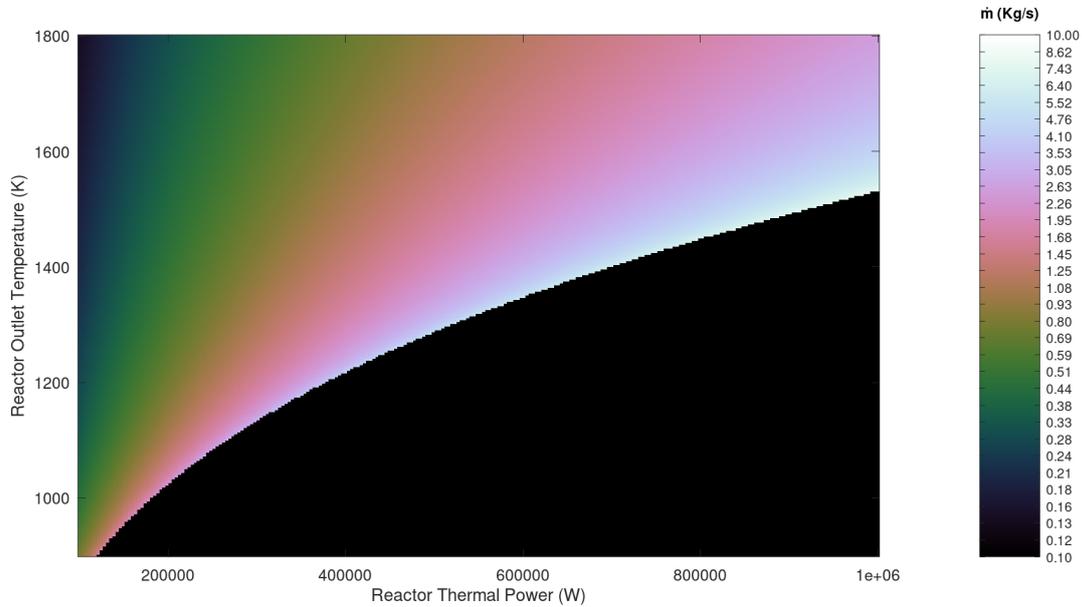


**Fig. 8.** 40 g/mol HeXe Mass Flow Rates for a Simple Brayton Cycle

Figure 8 shows the mass flow rates for the same system for a 40 g/mol HeXe coolant. Unfortunately, the previous thermal hydraulic analysis provided a target reactor outlet temperature of 1200 K, with no solutions producing 100 KWe in Figure 9. Therefore, in this case, the designer would have to reduce the targeted NSP reactor power density until the reactor outlet temperatures are in the acceptable range for a reactor. As noted earlier, the reduced maximum linear power would be 150 W/cm at 1400 K. However, that is insufficient to get the system to 100 KWe class.
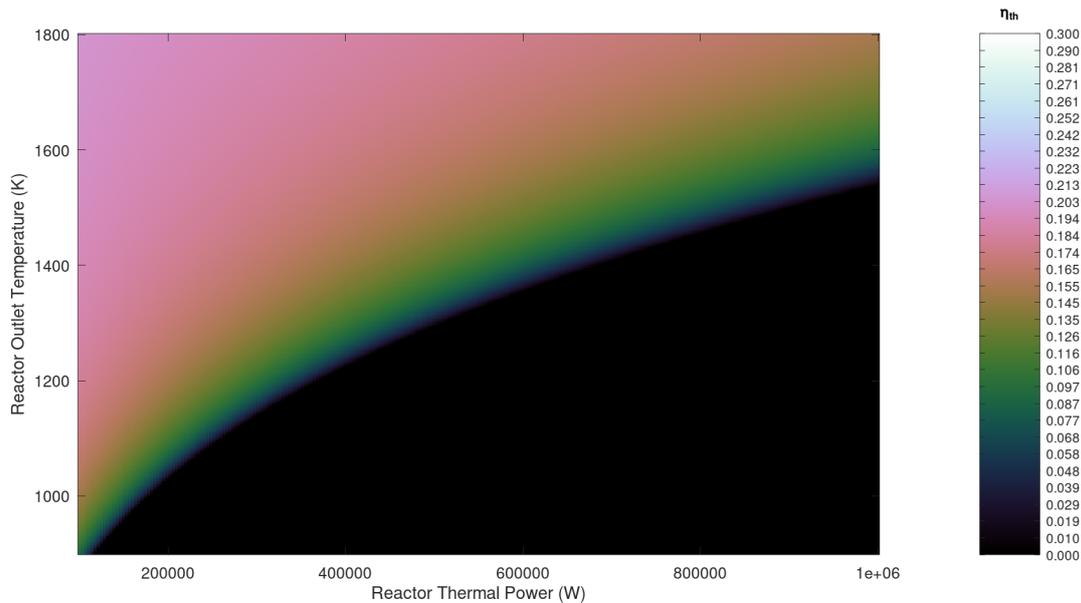
**Fig. 9.** Thermal to Electrical Conversion Efficiency for a Simple Brayton Cycle

Therefore, increasing the radiator area by 5 times is necessary, expanding the region of acceptable turbine inlet temperatures at the cost of redundancy. The simplicity of Equation 15 means NSP system engineers can quickly predict the resulting system temperatures and efficiencies. A 5 times increase in the radiator is required because we wish to preserve the conversion efficiency and have a system that is 20 % efficient with a reactor thermal power of 500 KWth. As we are currently getting 20 % efficiency at 1400 K and 100 KWth, we need to increase the radiator area by 5 times to handle a 500 KWth heat load because Equation 15 is linear in reactor power versus radiator area. Overall, the conversion efficiency is deficient compared to the nearly 30 % of the more sophisticated systems presented in NSP literature [48] [49]. Regardless, given the target of 100 KWe class, our example system would fall into the required power class even at the low efficiencies of 20 % if reactor outlet temperatures and radiator areas were dramatically increased. Unfortunately, no redundant radiator area would be left even with such allowances. More sophisticated systems would be significantly more efficient but still struggle with single-failure redundancy and mass budgeting issues.

This analysis shows the utility of the thermals first approach. Even though we have yet to discuss nuclear engineering in detail, thermal considerations have fully constrained the reactor design for us. These computationally inexpensive analyses provide valuable data regarding the design space in which an NSP system remains practical. Next, we discuss a Rankine cycle with sodium coolant for completeness. Again, complete mathematical derivations are available in Appendix B. Rankine cycles depend on materials property data. For our analysis, we relied on an IAEA publication [36] for sodium liquid and vapour thermophysical properties, such as enthalpy, density and partial pressure. The entropy and ratio of specific heat data from [50] were curve-fitted in Microsoft Excel with an R-value above 0.999. For lack of a better and simpler alternative, we averaged the ratio of specific heats between 900

and 1800 K, which resulted in 1.5757. The final equations for the coolant properties required for a sodium Rankine cycle are presented in Table 7.

**Table 7.** Thermophysical Properties Data Relevant to Sodium Rankine Cycles

| Sodium Property | Equation | Application Limits | Reference |
|---|---|---|---|
| Liquid Enthalpy (KJ/Kg) | $H_l = -365.77 + 1.6582\,T - 4.2395\text{E-4}\,T^2 + 1.4847\text{E-7}\,T^3 + \frac{2992.6}{T}$ | 380 K < T < 2000 K | [36] |
| Vapourisation Enthalpy (KJ/Kg) | $\Delta H_g = 393.37\left[1 - \frac{T}{2503.7}\right] + 4393.6\left[1 - \frac{T}{2503.7}\right]^{0.29302}$ | 380 K < T < 2000 K | [36] |
| Liquid Entropy (KJ/KgK) | $S_l = 7.4402\text{E-1} + 8.2785\text{E-3}\,T - 9.1681\text{E-6}\,T^2 + 6.0062\text{E-9}\,T^3 - 2.0202\text{E-12}\,T^4 + 2.7196\text{E-16}\,T^5$ | 380 K < T < 2000 K | [50] |
| Vapour Entropy (KJ/KgK) | $S_g = 2.9487\text{E1} - 6.0974\text{E-2}\,T + 7.1262\text{E-5}\,T^2 - 4.3225\text{E-8}\,T^3 + 1.3147\text{E-11}\,T^4 - 1.5835\text{E-15}\,T^5$ | 380 K < T < 2000 K | [50] |
| Partial Pressure (Pa) | $P_{sat} = \exp\left[11.9463 - \frac{12633.73}{T} - 0.4672\ln T\right]$ | 900 K < T < 2000 K | [36] |
| Liquid Density (Kg/m$^3$) | $\rho_l = 219.00 + 275.32\left[1 - \frac{T}{2503.7}\right] + 511.58\left[1 - \frac{T}{2503.7}\right]^{0.5}$ | 380 K < T < 2000 K | [36] |
| Ratio of Specific Heats of Vapour | $\gamma = 3.2012 - 7.6516\text{E-3}\,T + 1.1781\text{E-5}\,T^2 - 8.5367\text{E-9}\,T^3 + 3.0237\text{E-12}\,T^4 - 4.0740\text{E-16}\,T^5$ | 380 K < T < 2000 K | [50] |
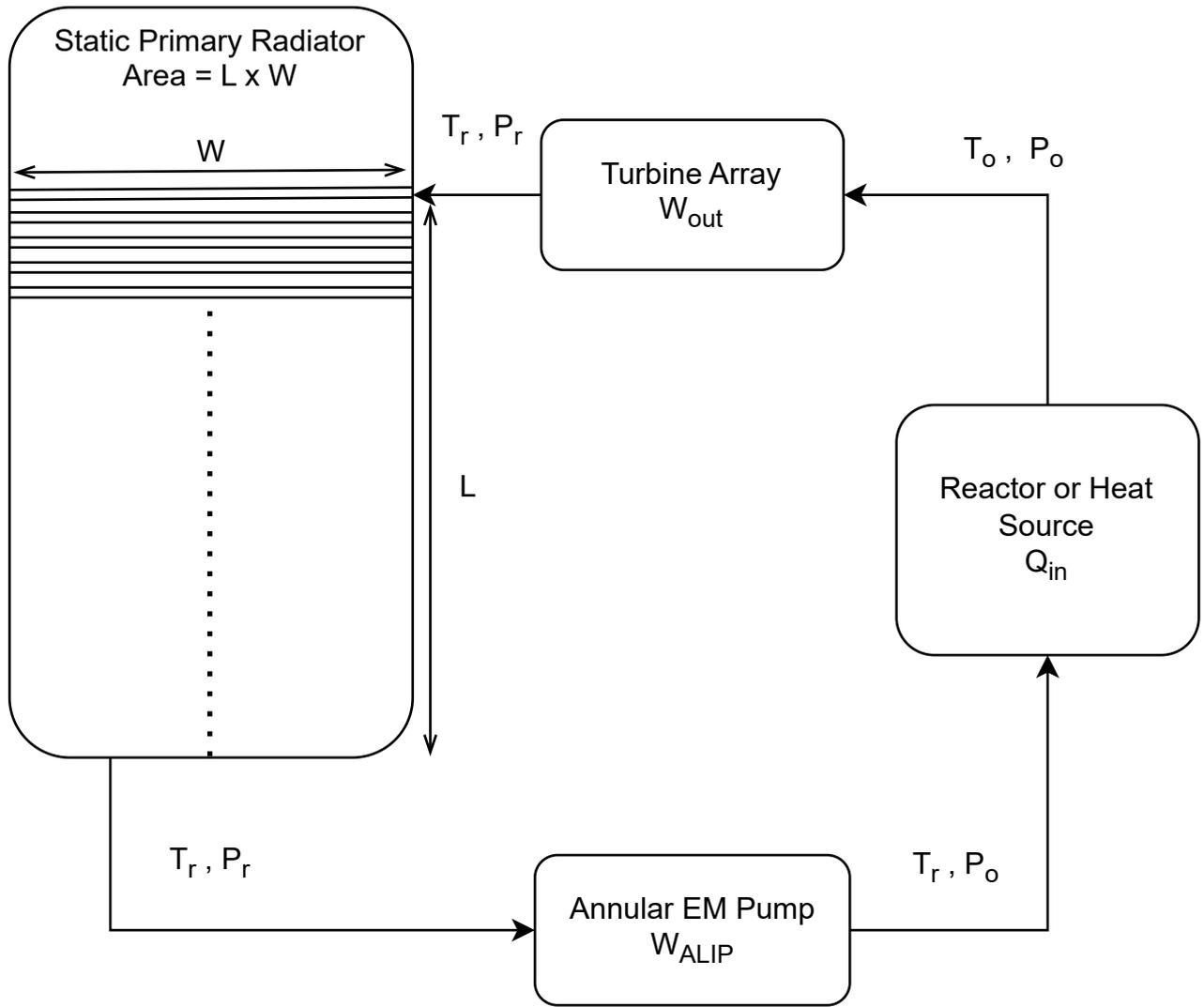
**Fig. 10.** Simple Rankine Heat Engine Coupled to a Radiator

Figure 10 shows the structure of the Rankine cycle we analysed. Using the energy balance we previously applied to the Brayton cycle, we get a new expression, Equation 19, for the cycle mass flow rate. Since the heat rejection was now at a constant temperature, the mathematics for the radiator were straightforward. Equation 20 provides the normalised radiator area required to condense the wet vapour exiting the turbine. The radiator area is normalised to the one required by the Brayton cycle in the past analysis.

$$\dot{m} = \frac{Q_{in}}{H_l(T_o) - H_l(T_r) + \Delta H_g(T_o)} \tag{19}$$

$$A_{norm} = \frac{\dot{m} \Delta H_g(T_r) X_r}{\epsilon \sigma_b L W T_r^4} \tag{20}$$

The turbine expands the sodium vapour isentropically, condensing a fraction of it in the process. Using the isentropic relations, we can find the turbine outlet temperature. Further,

the entropy data provide us with a means to find the vapour quality at the turbine exit:

$$X_r = \frac{S_g(T_o) - S_g(T_r)}{S_g(T_r) - S_l(T_r)} \tag{21}$$

The minimum vapour quality is usually around 0.8 for test Rankine cycles to avoid cavitation damage and turbine erosion [51]. However, we set the TPR here to 0.5 instead to compare the performance with the Brayton cycle. Now, we must find the power requirements of the sodium pump to calculate the cycle conversion efficiency. Since liquid sodium is an incompressible fluid, the pumping power of the annular electromagnetic linear induction pump is given by:

$$W_{ALIP} = F_p P_o (1 - TPR) \frac{\dot{m}}{\rho_l(T_r)} \tag{22}$$

All other cycle inputs are defined similarly to the Brayton cycle to facilitate comparison and are provided in Table 6. Finally, we can express the cycle conversion efficiency as follows:

$$\eta_{th} = \eta_{gen} \frac{H_g(T_o) - X_r \Delta H_g(T_r) - H_l(T_r) - \frac{F_p P_o (1 - TPR)}{\rho_l(T_r)}}{H_l(T_o) - H_l(T_r) + \Delta H_g(T_o)} \tag{23}$$

These equations complete the set to describe the heat cycle. Figure 11 shows the reactor temperature plot, and Figure 12 shows the corresponding nominal system pressure. Note that there is no temperature limiting region here compared to the Brayton cycle. Secondly, the surface plot has banding parallel to the x-axis, meaning that the reactor inlet temperatures are independent of the heat source power. These results show that NSP system designers have much greater flexibility with this cycle than with a Brayton cycle. The turbine inlet pressure is 0.7 MPa for a temperature of 1400 K compared to the 2 MPa for the HeXe Brayton cycle. This reduction in system pressure shall contribute to a reduction in plumbing and pressure vessel mass and cost reduction compared to the Brayton cycle. Compared to the Brayton cycle, the mass flow rates fall below 50 g/s, a hundred times less due to the impressively high heat of vapourisation of sodium. Ultimately, sodium surpasses pure helium or HeXe in every metric of comparison.
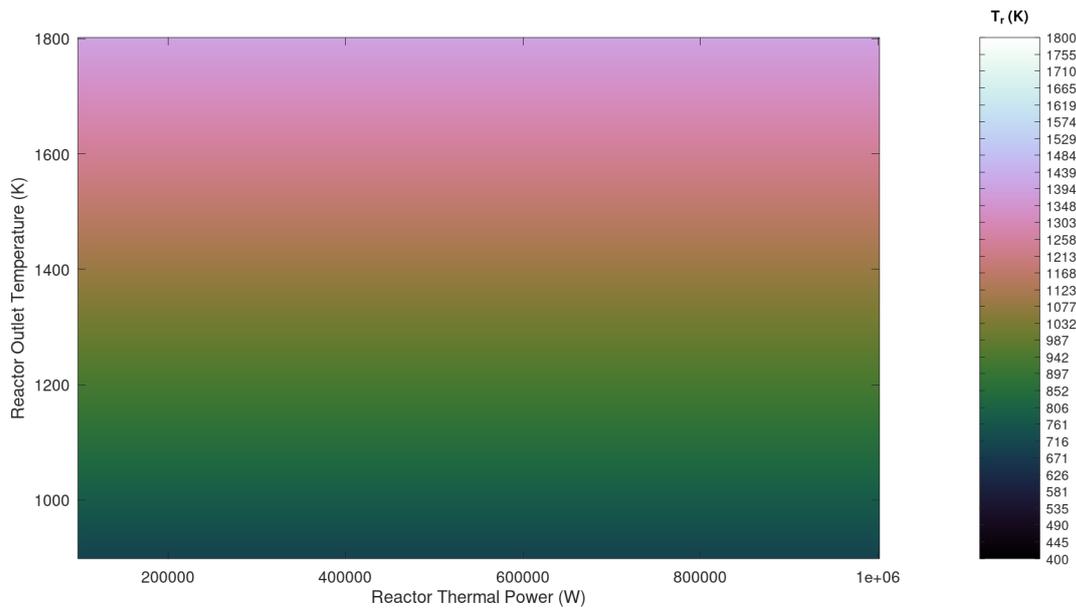
**Fig. 11.** Reactor Inlet Temperature for a Simple Sodium Rankine Cycle
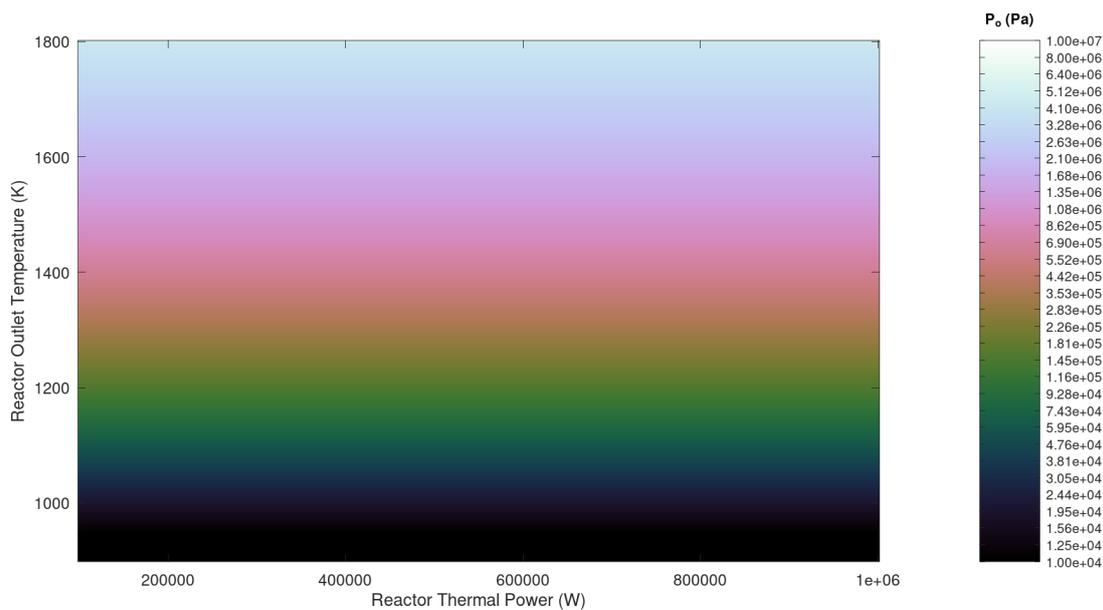


**Fig. 12.** Turbine Inlet Pressure for a Simple Sodium Rankine Cycle

Figure 13 shows the normalised radiator areas compared to the Brayton cycle. We immediately see a region where the required radiator area is larger than the Brayton cycle. However, at 1400 K, the radiator area required is roughly 30 % of that of the Brayton cycle at 500 KWth. If the turbine inlet temperature is 1200 K, the ratio of the radiator areas is nearly 0.55 at 500 KWth. Therefore, our hypothesis that a Brayton cycle performs poorly when coupled to a radiator was proven correct. Furthermore, the Rankine cycle does not require all four radiator panels available to produce 100 KWe, making at least one radiator panel redundant.
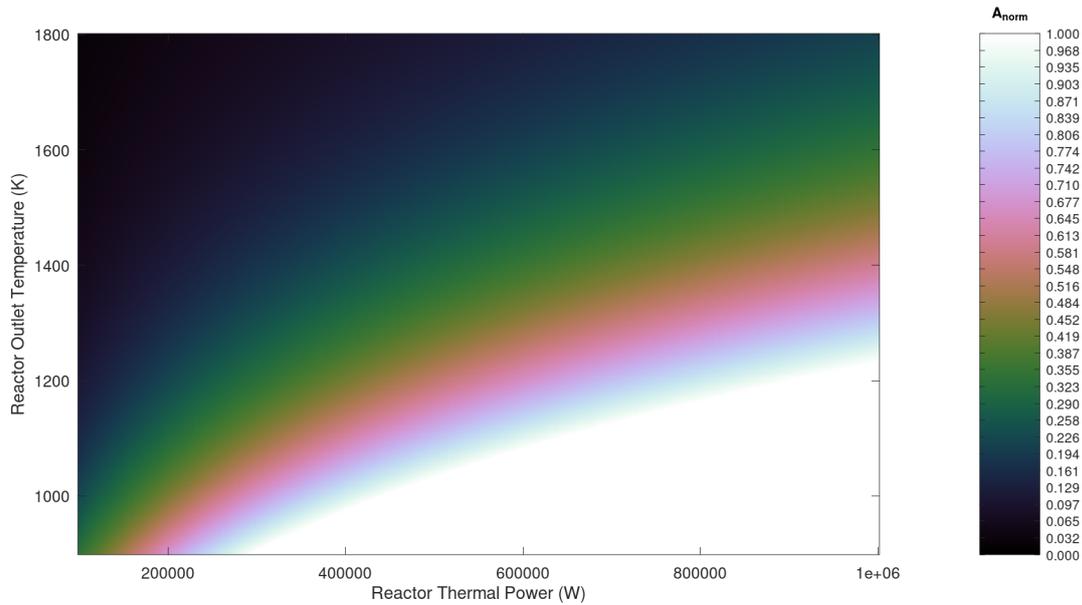
**Fig. 13.** Radiator Area for a Simple Sodium Rankine Cycle Normalised to the Brayton Cycle Radiator Area

Finally, Figure 14 shows the Rankine cycle's conversion efficiency. At the same cycle parameters, the simple Rankine cycle also has an efficiency of nearly 18 % at 1400 K, independent of the heat source power. Notably, the cycle efficiency at 1200 K is similar. There is a minimum in the efficiency around 1400 K because there is a corresponding minimum in the entropy difference between sodium liquid and vapour around 1400 K [50]. This property of sodium causes the vapour quality to increase at those temperature ranges and consequently reduces the cycle efficiency. Looking back to Figure 9, we see that the cycle efficiency for a Brayton system decreases with increasing reactor power as the radiator struggles to reject the heat. However, we did not employ a fixed radiator area when analysing the Rankine cycle. Regardless, as Figure 13 shows, there is a large region of the parameter space where the resulting required radiator areas are smaller than the Brayton cycle.
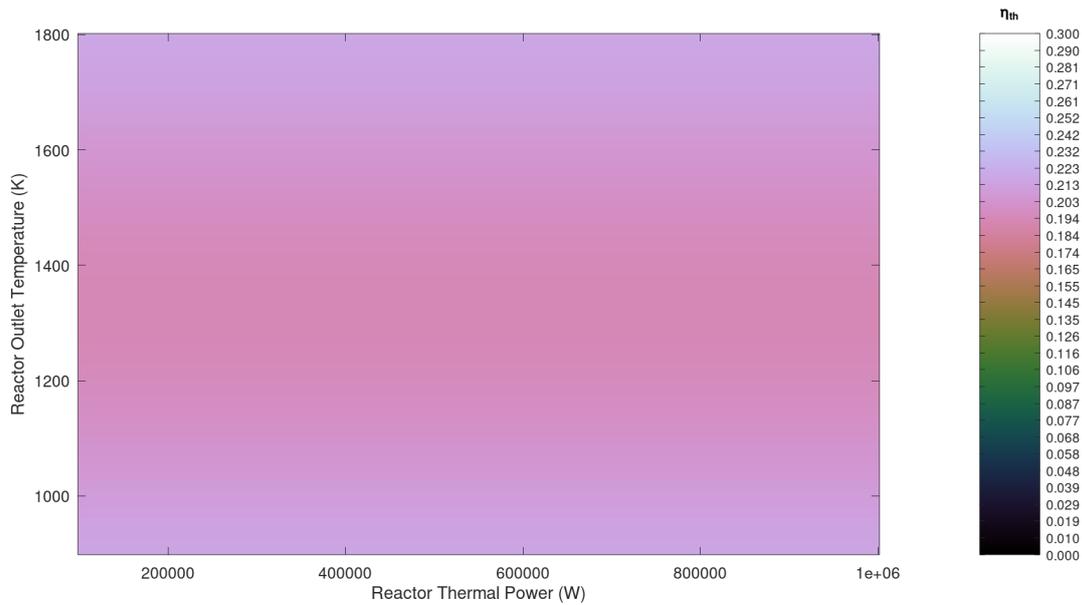
**Fig. 14.** Thermal to Electrical Conversion Efficiency for a Simple Sodium Rankine Cycle

## 3.5  Summary of Trends in Presented Models

In this chapter, we investigated thermal hydraulic and heat cycle models to develop our NSP reactor engineering constraints further. We studied fundamental trends that emerge in thermal management systems that reject large amounts of heat at high temperatures through simple and rudimentary models. The mathematical models we developed for the fuel element thermal hydraulics and heat engine thermodynamics were solved by GNU Octave 8.3.0 scripts in Appendix B.

The pin-in-cell model we used was simple enough to develop a helpful set of analytical tools to study the thermal hydraulic performance. Those efforts culminated in Figure 4, which shows that as the maximum coolant temperature increased, the maximum linear power density of the UN fuel pellet had to decrease for a fixed centreline temperature. Given the fuel element we chose, there was a set of fundamental mass flux limits concerning reactor core pressure drop, incompressible coolant flow and the Taylor HTC correlations applicability that we accounted for. Ultimately, we found that a coolant temperature of 1200 K in a coolant channel of 0.75 cm$^2$ supported the targeted linear power density of 275 W/cm. The issue was that over 300 K of the temperature drop between 1600 K and 1200 K occurred due to the low HTC of 40 g/mol HeXe gas coolant.

The maximum linear power density skyrocketed when the gas coolant was replaced with evaporating sodium, providing an isothermal environment. At 1200 K, the maximum linear power density was 1070 W/cm; at 1400 K, it was 550 W/cm. Therefore, we concluded that sodium Rankine systems that operated similarly to looped heat pipes in null g held promise.

Then, we developed a simple Brayton cycle's mathematical equations using isentropic relations and fundamental physics. First, we found that the radiator performance was independent of the gas coolant's properties, and the coolant's properties only affected the cycle mass flow rate. Second, we found that for our selected nuclear data relay application, there was not enough radiator area on the satellite bus to provide enough redundancy along with functional heat rejection at 1200 K and 1400 K. Figure 7 showed that for a given thermal power, increasing the reactor outlet temperature would result in a decrease in the radiator exit temperature. Thus, we had to consider a 1400 K reactor outlet temperature by reducing the maximum reactor linear power density to 150 W/cm and increasing the total available radiator area by 5 times. Finally, we found that the simple Brayton cycle was relatively inefficient at power conversion, only managing 20 % at selected temperatures.

At the beginning of the chapter, we hypothesised that the Brayton cycle would have poor performance in space due to issues with heat conduction in the gas coolant and the inefficient usage of the available radiator area. To investigate further, we developed the mathematics for a simple sodium Rankine cycle, which accepts and rejects heat isothermally. Compared to a gas-cooled Brayton cycle, the isothermal heat transfer dramatically improved the linear power density limits and the required radiator areas. Figure 13 shows that the simple Rankine cycle required a smaller radiator for an ample parameter space than the Brayton cycle. We also found that the Rankine cycle functioned well at a radiator temperature of 1200 K, had at least one redundant radiator panel and had nearly 18 % efficiency, independent of the input thermal power. This behaviour starkly contrasted with the Brayton cycle, which suffered from a decrease in efficiency as the thermal power was increased while keeping the radiator area constant. Overall, this chapter produced a strong argument for NSP system designers to research and develop Rankine cycle and sodium turbo-alternators for second-generation NSP systems. Table 8 summarises our results in numbers. A vast amount of legacy literature deals with gas-cooled Brayton cycles; therefore, it seems likely that the first generation of NSP systems would deploy a Brayton cycle. For later chapters in this thesis, we continue with a 40 g/mol HeXe-cooled Brayton system to maintain applicability with legacy NSP system designs. The next chapter builds upon the results of our analysis here to eliminate moderator materials and design a parametric neutronics performance study of NSP reactor cores.

**Table 8.** Summary of Rudimentary Brayton and Rankine Heat Cycle Analysis for NSP Systems in Geostationary Orbit

| NSP System Parameter | Optimum Value for Brayton Cycle | Optimum Value for Rankine Cycle |
|---|---|---|
| Radiator Width | 1.5 m | 1.5 m |
| Radiator Height | 3.5 m | 3.5 m |
| Radiator Emissivity | 0.8 | 0.8 |
| Radiator Tubing Material | MA 956 ODS | MA 956 ODS |
| Required Number of Radiator Panels | 10 | 2 |
| Available Radiator Panels on Bus | 4 | 4 |
| Generator Efficiency | 0.9 | 0.9 |
| Turbine Pressure Ratio | 0.5 | 0.5 |
| Pressure Factor | 1.2 | 1.2 |
| Reactor Thermal Power | 500 KWth | 750 KWth |
| Heat Cycle Conversion Efficiency | 0.20 | 0.18 |
| Reactor Outlet Temperature | 1400 K | 1400 K |
| Maximum Fuel Element Linear Power | 150 W/cm | 550 W/cm |
| HeXe Coolant Channel Area | 0.75 cm$^2$ | - |
| HeXe Coolant Molar Mass | 40 g/mol | - |

# 4  Selecting Moderators for Nuclear Space Power Reactors

It is finally time to begin nuclear engineering. In this chapter, we synthesise the constraints developed in the previous chapters to develop a framework to study various moderator materials for NSP reactor designs. Table 8 represents the overall design constraints on the HeXe-cooled NSP system design for the nuclear data relay. The thermal power output requirement and the maximum linear power limit effectively decide the total NSP reactor core volume. The maximum reactor outlet temperature is vital in eliminating moderator materials choices. As in Chapter 2, we create a predictable framework to eliminate moderator material choices. We use [31] as a monolithic and composite moderator materials reference.

Recently, a need for high-temperature and high neutron stopping power moderators has been recognised. Starting from the set of base materials in [31], we used Fact-Web to predict the bounding operating temperature of yttrium, zirconium and calcium hydrides at a pressure of 2 MPa. There is a consensus in the literature [31] [32] that hydride moderators are necessary for thermal spectrum nuclear microreactors, which are neutronically similar to NSP reactors. Table 9 displays our findings. At 0.1 MPa, zirconium hydride dehydrides at 900 K while yttrium hydride remains stable at 1200 K [52]. Fact-Web suggests that as the hydrogen partial pressure increases to 2 MPa, zirconium hydride is more resistant to dehydriding than yttrium hydride.

**Table 9.** Dehydriding Temperatures of High-Temperature Metal Dihydrides at 2 MPa

| Metal Dihydride | Maximum Operating Temperature at 2 MPa |
|---|---|
| Zirconium | 1300 K |
| Yttrium | 1200 K |
| Calcium | 1600 K |

Hydrogen loss at high temperatures [53] is a critical issue with monolithic hydride moderators. The universally agreed solution is the development of composite moderators [31]. Composite moderators comprise a non-moderating, weakly neutron-absorbing matrix carrying a highly moderating metal hydride. Typically, MgO is used for a matrix with zirconium and yttrium hydrides as the entrained moderator [31]. MgO is impermeable to hydrogen and thus prevents outgassing [52], enabling composite moderators to function at higher temperatures than their monolithic counterparts. In this thesis, we focus on composite moderators because, as Table 9 shows, familiar monolithic moderators used by nuclear engineers undergo dehydriding well below the temperatures that our thermodynamic analysis of a 100 KWe class NSP system called for.

## 4.1 Potential Moderator Materials

As discussed, hydrides of zirconium, yttrium and calcium have been studied for application in microreactors [32]. Figure 15 describes the results of our Fact-Web compatibility calculations.
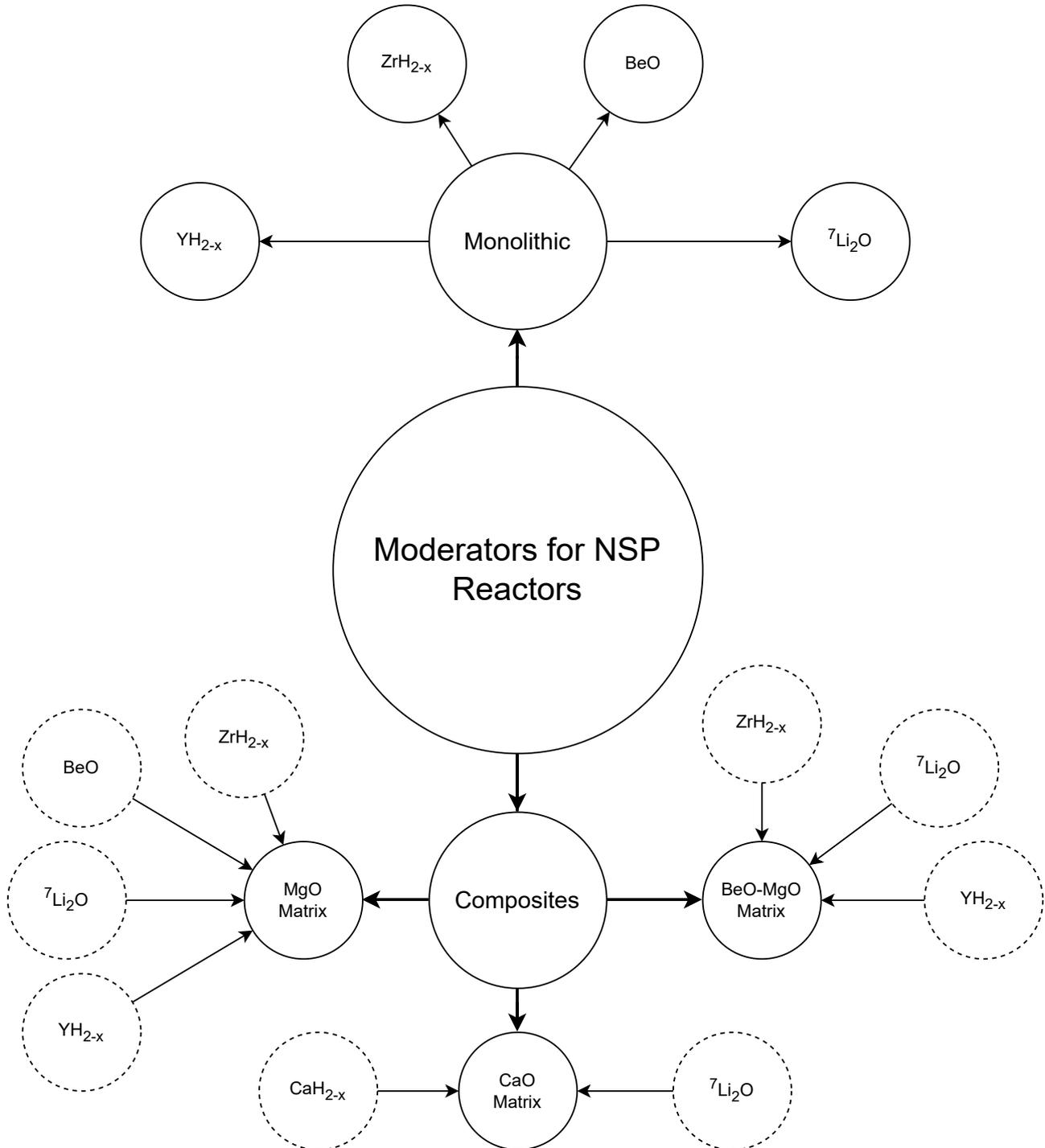


**Fig. 15.** High-Temperature Chemical Compatibility Chart for Monolithic and Composite Moderator Materials for NSP Reactors

We selected compounds containing moderating elements such as H and Li and subjected them to 1400 K and 2 MPa with the software. We can see why the MgO matrix is a popular

choice, as MgO is compatible with a range of moderating hydrides and oxides. Furthermore, MgO composites can be sintered below 1000 K with LiF [31] addition, enabling these composites to be practically manufactured without subjecting the entrained moderator to dehydriding temperatures. BeO as a matrix is enticing but suffers from a high sintering onset temperature of 1563 K [54], which means that hydrides cannot easily be incorporated. After a literature review, we found work [55] describing a BeO-MgO eutectic ceramic composed of 70 mole % of BeO, which melts near 2133 K [55]. While there are no sintering studies of this ceramic eutectic mixture, we expect the sintering onset temperature to be approximately half the melting temperature, resulting in 1066 K. Further, the presence of MgO implies that sintering additives such as LiF [31] that catalyse MgO sintering could assist in sintering BeO-MgO as well. Therefore, we included BeO-MgO in our study as it is potentially manufacturable and a better composite moderator than simple MgO composites.

Finally, we considered calcium hydride. $CaH_2$ is incompatible with MgO at the temperatures of interest. $CaH_2$ is well known for having a high dehydriding temperature and low hydrogen partial pressure [56]. It has been recently studied for thermal batteries for terrestrial solar thermal power plants [57] and as a moderator for nuclear reactors [58]. The corresponding matrix, CaO, is inexpensive and commercially available. The kinetics of sintering CaO are not as well studied as MgO, but they seem similar and are also catalysed by LiF [59]. Therefore, it seems that a $CaH_2$ containing composite moderator would be an inexpensive competitor to the rare earth hydride-containing options. Ultimately, we are cautious about this moderator's viability as $CaH_2$ begins to melt from 1090 K, and thus, the CaO would require to contain a molten moderator, which has no precedent. Recent studies of composite phase change materials support the viability of such composites [60]. However, an experimental campaign would be necessary to understand if a $CaH_2$ containing composite is a manufacturable and practical high-temperature neutron moderator.

Aside from chemical compatibility, we also considered the depth of literature and experience with the moderator materials in question. Figure 16 summarises our findings. We found no data on the thermophysical properties of lithium oxides, which removed them from consideration. Natural lithium has a high thermal neutron absorption cross section [30], and nuclear reactions in the moderator release helium gas. Therefore, its viability as a high-temperature, long-life neutron moderator is limited, and we can safely eliminate it.

| | YH$_x$ | ZrH$_x$ | Be | BeO | MgO | CaO | CaH$_x$ |
|---|---|---|---|---|---|---|---|
| S($\alpha$, $\beta$) | ENDF VIII.0 | ENDF VIII.0 | ENDF VIII.0 | ENDF VIII.0 | NCRYSTAL | NCRYSTAL | JEFF 3.3 |
| $\rho$(T) | Shivaprasad-2020 | Yamanaka-2002 | Tomberlin-2004 | Hou-2022a | Hofmeister-2014 | Tian-2022 | Kimura-2019 |
| $C_p$(T) | Shivaprasad-2020 | Yamanaka-1999 | Tomberlin-2004 | Hou-2022a | Hofmeister-2014 | Chase-1998 | Balakrishnan-2023 |
| CTE(T) | Shivaprasad-2020 | Yamanaka-1999 | Tomberlin-2004 | Hou-2022a | | | |
| k(T) | Shivaprasad-2020 | Tsuchiya-2001 | Tomberlin-2004 | Hou-2022a | Hofmeister-2014 | Bird-2020 | Balakrishnan-2023 |
| PIE | Shivaprasad-2020 | | Kawamura-2004 | Hou-2022b | Hickman-1965 | | |
| $T_{melt}$ | Shivaprasad-2020 | Shivaprasad-2022 | Tomberlin-2004 | Hou-2022a | Jiang-2017 | Tian-2022 | Balakrishnan-2023 |
| $T_{sinter}$ | Shivaprasad-2020 | Snead-2022 | Kurinskiy-2018 | Hou-2022a | Jiang-2017 | Tian-2022 | |
| $S_a$(T) | Shivaprasad-2020 | Yamanaka-1999 | Tomberlin-2004 | Hou-2022a | Vasilos-1964 | | |

| |
|---|
| **Complete Data** |
| **Incomplete Data** |
| **Not Readily Available** |

**Fig. 16.** Thermophysical and Mechanical Properties Data Availability of High-Temperature Moderator and Matrix Materials

**Table 10.** High-Temperature Moderators for NSP Reactors

| Moderator Name | Atomic Composition | Density at 298 K (Kg/m$^3$) |
|---|---|---|
| Graphite | C: 1 | 1710 |
| Zirconium Hydride (H/M = 1.66) | Zr: 0.38, H: 0.62 | 5653 |
| Yttrium Hydride (H/M = 1.8) | Y: 0.36, H: 0.64 | 4293 |
| Beryllium Oxide | Be: 0.5, O: 0.5 | 3015 |
| 40 vol % YH$_{1.8}$ in MgO | Y: 0.12, H: 0.21, Mg: 0.33, O: 0.33 | 3866 |
| 40 vol % YH$_{1.8}$ in 70 mole % BeO-MgO Eutectic | Y: 0.11, H: 0.19, Be: 0.25, Mg: 0.10, O: 0.35 | 3651 |
| 40 vol % CaH$_2$ in CaO | Ca: 0.43, H: 0.27, O: 0.30 | 2684 |

We found similar issues with beryllium and its alloys; thus, we also removed them from further consideration. We noted a gap in the literature regarding post-irradiation examination (PIE) and density versus service temperature for zirconium hydrides. Despite having many gaps in knowledge, allowable mechanical stress ($S_a$) and thermophysical properties data, we chose to include calcium hydride in our study because of their potential cost savings and high-temperature dehydriding resistance. We also included graphite and BeO due to their extensive use in fast reactor designs, which allowed us to compare our results with fast reactor NSP systems. Table 10 shows the moderators we considered for further neutronics analysis. Figure 16 references the appropriate sources for each material, which we have cited in the thesis's bibliography. Graphite properties are available in [21]. We arbitrarily chose yttrium hydride for the entrained material in the composite moderators to facilitate direct comparison between modifications in the matrix composition.

Now that we have identified the moderator materials to investigate, we discuss the neutronics software used and the study's methodology.

## 4.2 Choice of Simulation Code

Our investigation aims to understand the situations where particular moderators result in an overall superior NSP reactor design. We include the learnings from the previous chapters to determine the materials and expected operational environment. Our study continues to use the simple pin-in-cell fuel element shown in the previous chapter in Figure 2. For that fuel element, the only free design parameter is the size of the moderator hexagonal block because the other dimensions have been constrained by past fuel development and characterisation programs [38] and our analysis in Chapter 3.

Therefore, it is clear that we need to vary the dimensions of the hexagonal moderator block, or in other words, the moderator to fuel (MF) volume ratio. Further, we have a set of 7 materials we wish to study. A parametric study is required. The open-source Monte Carlo

code OpenMC was best suited to such studies because of its integration with the Python API, enabling us to pass variables to the code to define the simulation geometry [61]. It features depletion capability [62] and official compatibility with the latest nuclear data libraries (ENDF VIII.0). Moreover, geometry models created for OpenMC are cross-compatible with OpenMOC [63], an open-source deterministic code for nuclear reactor criticality calculations [64]. The cross-compatibility meant that our model was also amenable to deterministic calculations for verification and validation. Finally, the open-source nature of the codes meant that any interested NSP system designer could rerun our simulations to represent their specific use case, leading to more precise predictions and insights than we can provide here. Our simulation codes and results post-processing Python scripts are available in Appendix A. Appendix A also covers the simulation environment setup to ease the reproduction of our results.

## 4.3 Methodology of Moderator Neutronics Analysis

Table 11 represents the scope of the parametric study conducted with OpenMC 0.13.3. We chose the minimum Moderator to Fuel (MF) volume ratio of 1 and a maximum of 25 after preliminary calculations to maximise the data return from the simulation time taken. Any moderator material has an optimum MF volume ratio. An optimum value exists because reducing the amount of moderator would decrease the thermal neutrons present in the system to cause fission. On the other hand, increasing the MF ratio would not further increase the thermal neutron population; instead, the excessive amount of moderator would begin to absorb the thermal neutrons in the system. For the 7 moderator materials in Table 10, all except graphite and BeO have their optimum MF volume ratio between 1 and 25. One expects graphite and BeO to have an optimum MF ratio beyond 25 because they absorb thermal neutrons exceptionally weakly. However, these high MF ratios result in impractical NSP reactor core dimensions, and thus, the MF volume ratio was limited to 25.

Our simulations ignored any neutron leakage due to geometry at this stage to stay as general as possible and give NSP reactor engineers an unbiased data set. The simulation was 2D only, and the outer edges of the hexagonal moderator block were assigned a reflective boundary condition. In this configuration, we calculated the neutron multiplication factor as a function of the MF volume ratio for all 7 of the selected moderators. We labelled this study the Beginning Of Life (BOL) $K_{inf}$ study. We only ran enough neutrons to achieve a relative error of less than 0.005 and disabled photon tracking and simulation. Higher fidelity at this level of study is not necessary as we are interested in trends rather than precise values, and investigating many different configurations with a higher statistical accuracy was impractical.

We then moved on to the depletion simulations with the simplified CASL nuclide chain [65] for thermal reactors to reduce computation times without affecting the simulation results at the level of statistical accuracy we used. Neutron poison concentrations were established

**Table 11.** OpenMC Parametric Study Input Parameters and Parameter Limits

| OpenMC Model Parameter | Parameter Value |
|---|---|
| Minimum MF Volume Ratio | 1 |
| Maximum MF Volume Ratio | 25 |
| Depletion Power | 275 W/cm |
| Depletion Time | 10 years |
| Depletion Decay Chain | CASL - PWR |
| Fuel Pellet Material | UN |
| Fuel Pellet Density at 298 K | 14330 Kg/m$^3$ |
| Fuel Pellet Temperature | 1600 K |
| Fuel Clad Temperature | 1500 K |
| Moderator Temperature | 1200 K |

at 8.76, 87.6 and 876 hours before the Constant Extrapolation Linear Integrator (CELI) took larger timesteps to the final depletion time of 10 years. We chose this integrator and depletion schedule because they are the default found in the SERPENT Monte Carlo code, which meant our results were statistically identical to SERPENT 2.1.31. The depletion simulation provided us with two crucial data sets: the End of Life (EOL) $K_{inf}$ and the uranium burnup at EOL. UN irradiation campaigns have found that fuel pins irradiated to greater than 8 atom % burnup have a significant chance of failure.

In comparison, fuel pins with less than 7 atom % burnup remain intact [19]. $UO_2$ fuel pins have a higher burnup tolerance; up to 10 atom % has been successfully demonstrated in thermal reactors [19]. Therefore, it is vital to calculate the amount of burnup at EOL to ensure the reactor's fuel pins remain intact by the time EOL occurs. For this analysis, we continued with the specifications of UN fuel pellets irradiated and tested at 275 W/cm by NASA [38] for the SP-100 program.

Although our results in Chapter 3 indicate that operation at 1400 K is required, we continued the simulation with 1200 K with HeXe coolant because conventional hydrides dissociate at 1400 K at 2 MPa. All the materials used their density at 298 K for uniformity, as density versus temperature data was unavailable for most materials used in the model. To calculate its density, the 40 g/mol HeXe coolant gas was treated as an ideal gas at 2 MPa and 1200 K. Further, we used 1200 K as the moderator and coolant temperature because we wanted our results to reflect the maximum possible power the UN fuel pin was tested at.

Finally, we did not include thermal neutron scattering effects in our simulations. We found that thermal scatter data libraries did not exist at the temperatures of interest. Further, we found that their inclusion did not meaningfully impact the results within statistical errors. Since three of the seven moderators in Table 10 are novel and have no thermal scattering data, we chose not to include thermal scattering for all moderators in question without impacting the results.

Once all moderators' BOL and depletion simulations were complete, we created a Python script to assemble 3D NSP reactor cores using each moderator's optimum MF volume ratio. We chose the width between the flats of the hexagonal moderator block as the fuel element lattice pitch. We set the height of the reactor to 1.8474 times the reactor's circumscribing circle's radius to minimise geometric contributions to neutron leakage [39]. The Python script produced OpenMC models, which were simulated to find the 3D core BOL $K_{eff}$, minimum NSP reactor mass, height, and radius. We termed this study the Beginning Of Life (BOL) $K_{eff}$ study, where the difference between $K_{inf}$ and $K_{eff}$ is the geometric neutron leakage of a 3D geometry in contrast to a zero leakage reflective boundary 2D geometry in the $K_{inf}$ study.

## 4.4 Parameters for Comparing Moderators

Once the model is run, we expect a range of output data from the simulations. First, we shall determine the optimum MF volume ratio and then determine the MF mass ratio using the moderator to fuel density ratio. We define the optimal MF volume ratio as the MF volume ratio for which the BOL $K_{inf}$ value is the maximum. The ideal moderator for an NSP reactor should operate at high temperatures and have high neutron stopping power, which implies a low MF volume ratio. Finally, it would have a low mass compared to the UN fuel, which requires a low MF mass ratio.

Additionally, it would stimulate NSP reactor development and deployment if the moderator was easy to manufacture and relatively inexpensive. We would also prefer a high neutron economy from the reactor system. Since the $K_{inf}$ simulation does not factor in neutron leakage, neutron economy is only determined by the competing neutron moderation and absorption processes. Moderators with a high economy effectively thermalise neutrons without absorbing them, leaving them able to cause fission in the fuel. The more thermal neutrons available for fission, the more efficient the power production, ultimately reducing the burnup required to provide a fixed amount of power for a given period. Therefore, we seek a moderator that minimises the burnup with a neutron multiplication factor above one at EOL.

## 4.5 Reference Data for Simulation Model and Limitations of Study

In summary of this chapter, we present Table 12, which describes the pin-in-cell fuel element model, the materials used and the temperatures involved. This chapter discussed moderator materials for NSP reactor systems and identified 5 materials of promise, including 3 composites. While yttrium and zirconium hydrides have been popular in the literature, novel composite moderators show promise for compact, long-lived terrestrial microreactors. They are potentially helpful for NSP reactor systems that operate at high coolant temperatures to reject heat in space effectively. The coming chapters present the simulation results of these parametric OpenMC models.

Before moving on, let us reiterate the limitations of the model and framework discussed in this chapter. We wish to elucidate trends that provide insight to the NSP reactor designer. However, we acknowledge that each specific reactor design would have its fuel element design and, therefore, its own data set. To partially accommodate that shortcoming, we selected the open-source Monte Carlo particle transport and criticality simulation code OpenMC so that NSP systems designers may run their specific systems through our framework and simulations to obtain results tailored to their application. Our Python code is available in Appendix A. Besides that, the lack of material data was a source of error and assumptions. Most materials in the model did not have density versus temperature data published in the open literature. Thus, we were forced to use the densities at 298 K even though the material temperatures input to OpenMC were greater than 1200 K. The high temperatures also forced us to abandon the inclusion of thermal scatter physics as thermal scatter libraries above 1200 K were not available in ENDF VIII.0. Finally, due to constraints on computing time, we used a simplified decay chain for depletion simulation and set the maximum relative error on the neutron multiplication factor to 0.005.

**Table 12.** Summary of Pin-in-Cell Fuel Element Model for Parametric Simulations with OpenMC 0.13.3

| Fuel Element Parameter | Parameter Value |
|---|---|
| Fuel Pellet Material | UN |
| Fuel Pellet Density at 298 K | 14330 Kg/m$^3$ |
| Fuel Pellet Temperature | 1600 K |
| Fuel Pellet Linear Power | 275 W/cm |
| Fuel Pellet Diameter | 15.8 mm |
| Fuel Clad Material | MA 956 ODS |
| Fuel Clad Density at 298 K | 7250 Kg/m$^3$ |
| Fuel Clad Temperature | 1500 K |
| Fuel Clad Thickness | 0.5 mm |
| Coolant Material | 40 g/mol HeXe |
| Coolant Channel Area | 0.75 cm$^2$ |
| Coolant Pressure | 2 MPa |
| Coolant Temperature | 1200 K |
| Moderator Temperature | 1200 K |
| MF Volume Ratio | 1 to 25 |
| Depletion Time | 10 years |
| Depletion Decay Chain | CASL - PWR |
| Nuclear Data Library | ENDF VIII.0 |

# 5 $K_{inf}$ Analysis of Moderator Options – Variable UN Fuel Enrichment

As promised in Chapter 2, we now use the OpenMC model developed in the previous chapter to quantitatively analyse the influence of nitrogen and uranium enrichment on the neutronics performance of an NSP reactor using UN fuel pellets. The best scenario is when the UN fuel is 99.5 % enriched in 15-N, and the uranium is 24.75 % enriched. These enrichment levels are not whole numbers to allow tolerance for the enrichment process and uranium enrichment zoning to flatten the neutron power peaking profile. First, we shall compare UN fuels with varying uranium enrichment between 24.75 and 14.75 % with 99.5 % enriched nitrogen. Then, we shall discuss the effect of using natural nitrogen for a fixed uranium enrichment level. In the end, we attempt to suggest the appropriate combinations of enrichments for the UN fuel.

## 5.1 Variable Uranium Enrichment Results

Figure 17 shows the BOL $K_{inf}$ values obtained from the parametric OpenMC simulation for the 7 moderators listed in Table 10. As expected, graphite and BeO have low BOL $K_{inf}$ values because they are poor moderators, requiring a large MF volume ratio to begin thermalising neutrons. As the MF ratio increases, their $K_{inf}$ value rises towards that of the monolithic and composite hydride moderators. The difference between the $K_{inf}$ curve for graphite and any other moderator provides a qualitative measure of the degree of neutron thermalisation in the reactor for low MF volume ratios.
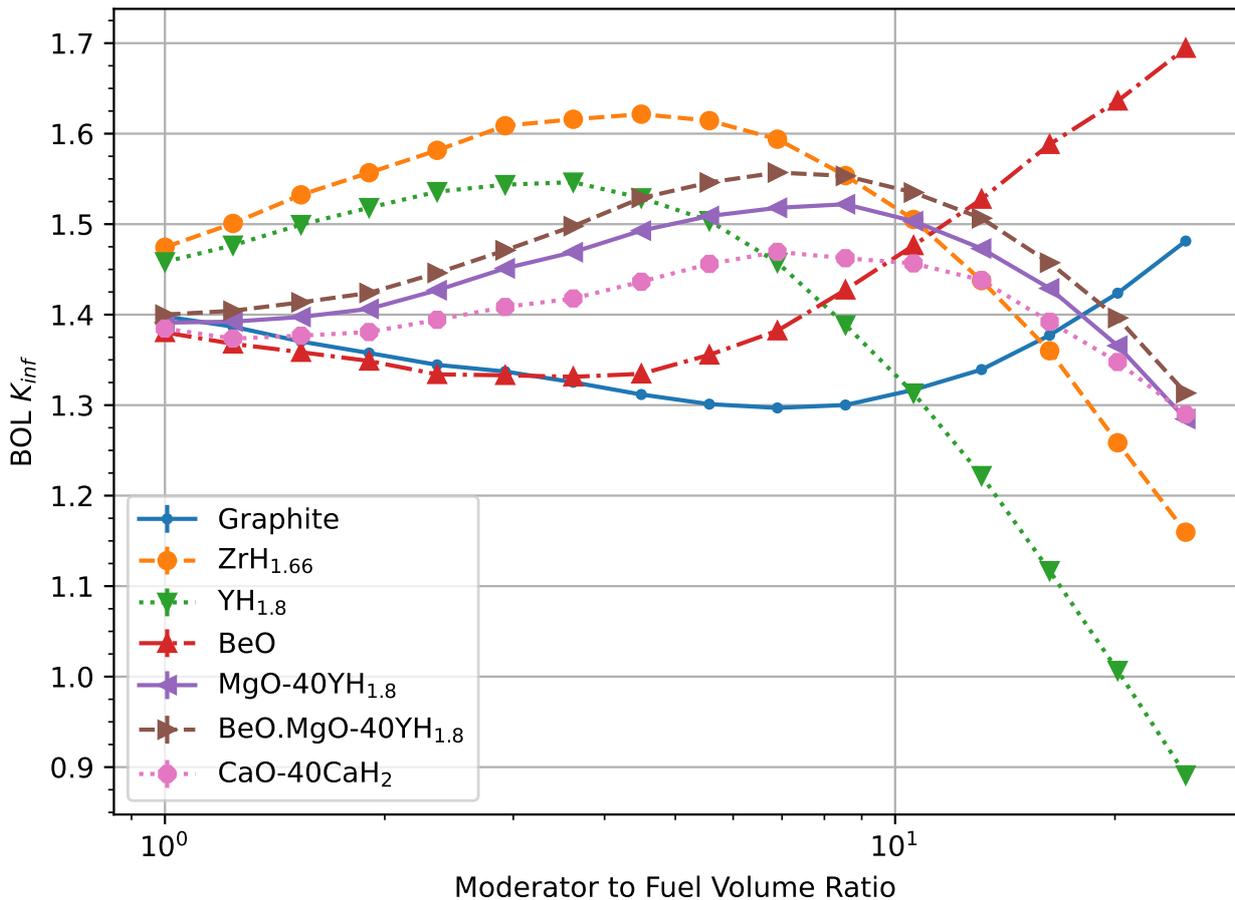
**Fig. 17.** Beginning of Life Infinite Neutron Multiplication Factor for Pin-in-Cell Fuel Element with 19.75 % Enriched UN Fuel and 99.5 % Enriched Nitrogen (Error Bars not Visible)

The monolithic hydrides have the highest $K_{inf}$ values, with zirconium hydride leading despite having a lower H/M ratio. Interestingly, they also have a lower rate of change of $K_{inf}$ versus the MF volume ratio compared to the composite moderators. The difference is because the composite moderator contains only 40 volume % hydride, reducing their relative moderating capacity and increasing the system's sensitivity to the MF volume ratio. Overall, the BeO-MgO composite performs on par with monolithic $YH_{1.8}$ while only using 40 vol % $YH_{1.8}$. The tradeoff is the larger MF volume ratio required for peak neutron moderation. As hypothesised, BeO-MgO surpasses the simple MgO composite, and we suggest material scientists launch an experimental campaign on 70 mole % BeO-MgO eutectic ceramic composite moderators to explore its manufacturability, costs and in-situ performance. Finally, we see that the $CaH_2$ composite performs the worst out of the composite moderators, possibly due to the thermal neutron absorption of calcium [30].

The OpenMC model also produces the optimum MF volume and mass ratios. Figures 18 and 19 show those results. Focusing on Figure 19, we see something intriguing. The $CaH_2$ composite results in a lower MF mass ratio than Zr hydride despite having a significantly large MF volume ratio in comparison. As noted in Table 10 in the previous chapter, the $CaO-CaH_2$

composite moderator is the least dense composite, and its high-temperature dehydriding resistance might mean that it is the only moderator option available for practical NSP systems of the 100 KWe class or higher.
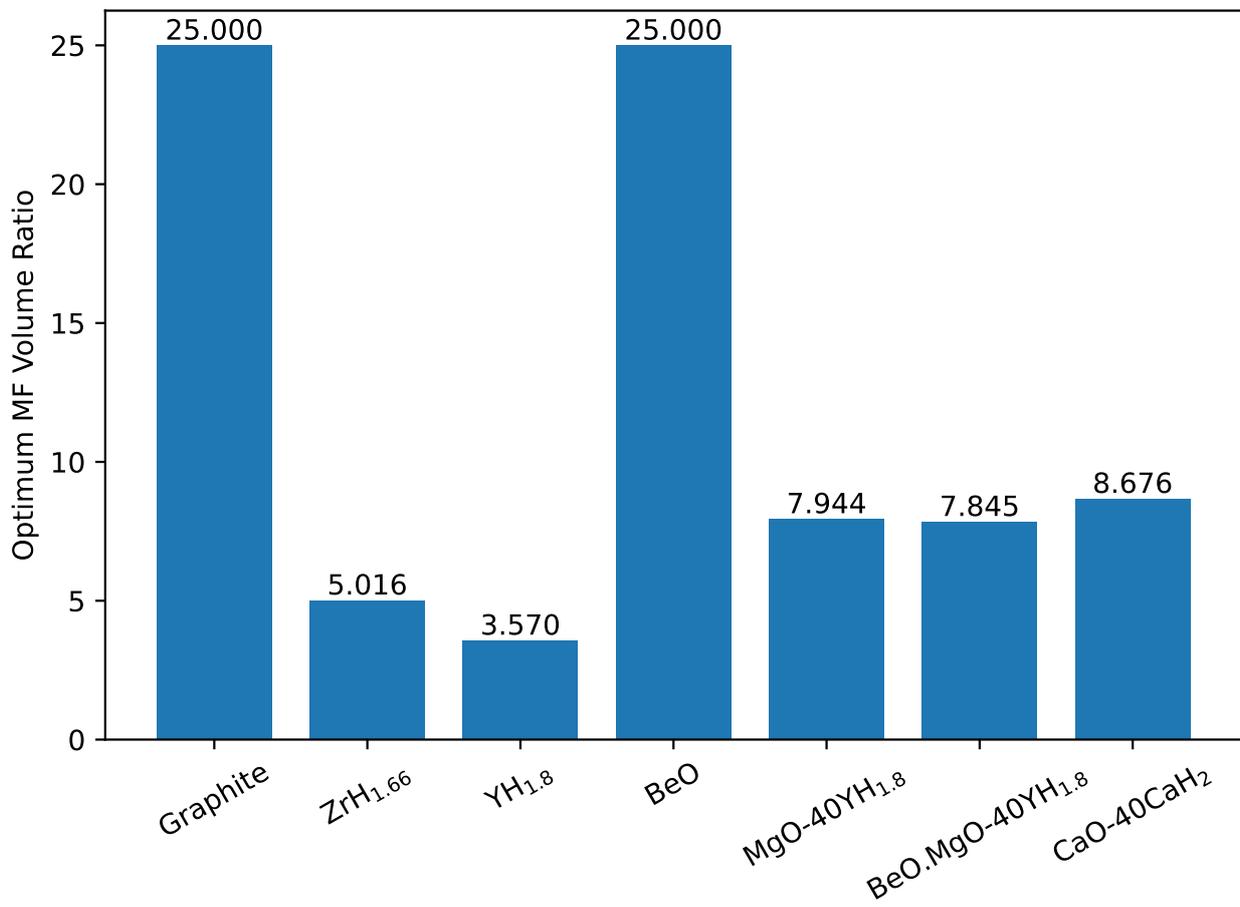


**Fig. 18.** Beginning of Life Optimum Moderator to Fuel Volume Ratios with 19.75 % Enriched UN Fuel and 99.5 % Enriched Nitrogen
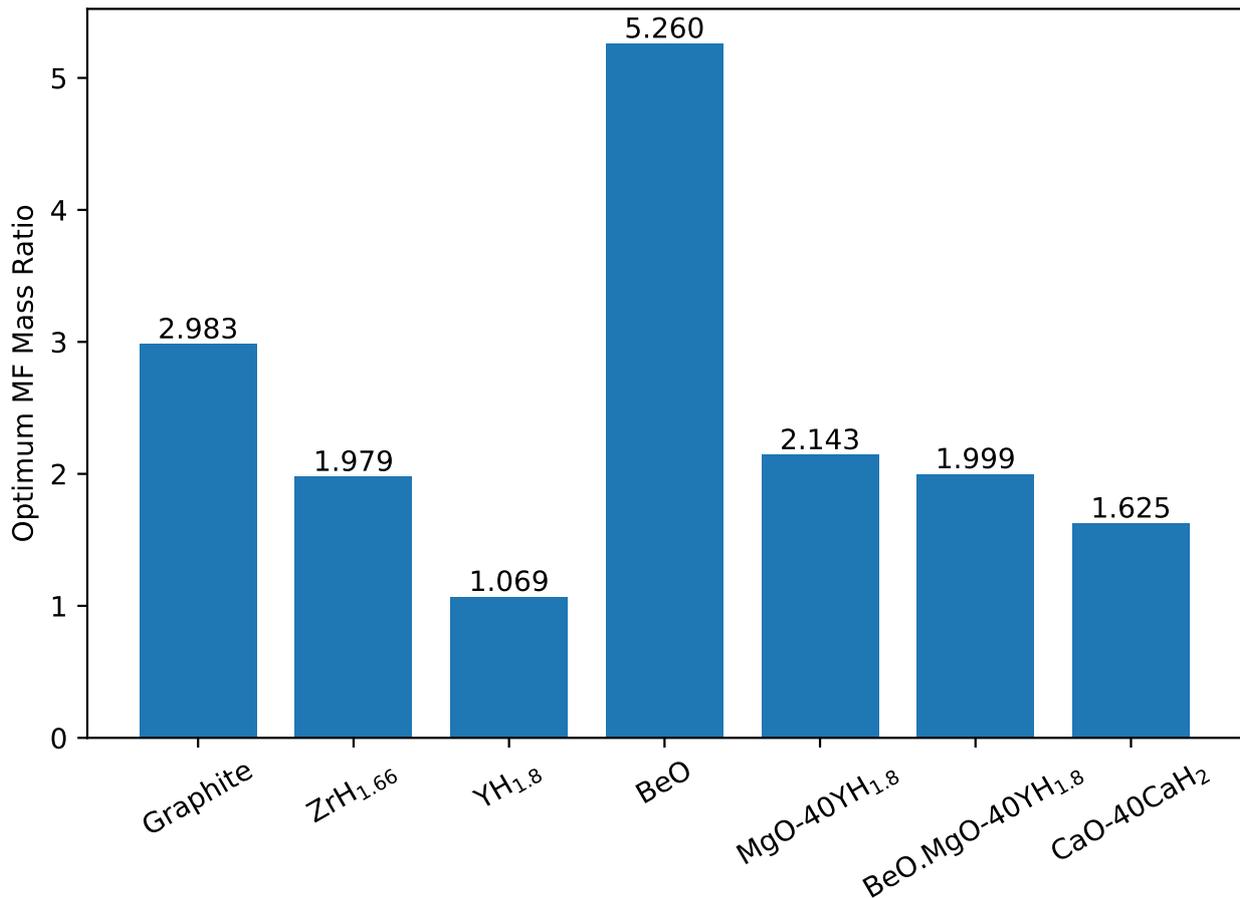
**Fig. 19.** Beginning of Life Optimum Moderator to Fuel Mass Ratios with 19.75 % Enriched UN Fuel and 99.5 % Enriched Nitrogen

Figures 20 and 21 show the per cent difference in the $K_{inf}$ values and the optimum MF ratio values when the uranium enrichment is reduced to 14.75 %. There is a clear trend that weakly moderating materials suffer the most from the drop in enrichment, and monolithic moderators are the least affected. The difference converges to about -4 % as the MF volume ratio increases. We believe the monolithic moderators' efficiency in thermalising neutrons is traded against the low uranium enrichment to produce a softer impact on the overall $K_{inf}$. The compositive moderators absorb a larger fraction of the neutrons they moderate; therefore, they suffer more than the monolithic moderators. Lastly, graphite and BeO experience the largest swing in $K_{inf}$ because they are very weak moderators, and the swing in $K_{inf}$ is primarily due to the reduction in fast fission in the enriched uranium. Looking at Figure 21, we note that the optimum MF volume ratio for the composite moderators has reduced. In contrast, the optimum MF ratio has increased for the monolithic moderators. We shall revisit this shortly.
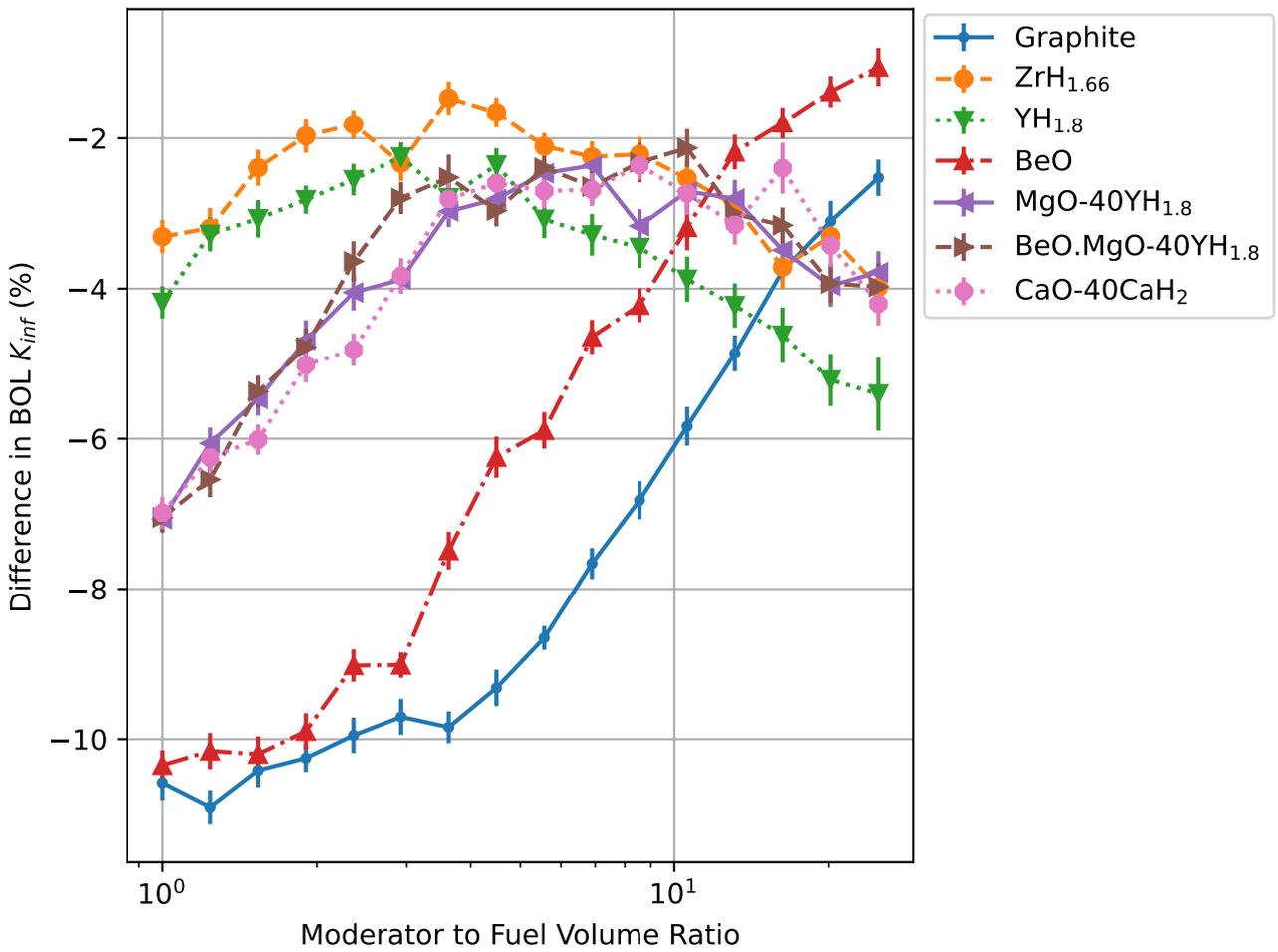
**Fig. 20.** Per Cent Difference of Beginning of Life Infinite Neutron Multiplication Factor Between 19.75 % and 14.75 % Enriched UN Fuel with 99.5 % Enriched Nitrogen
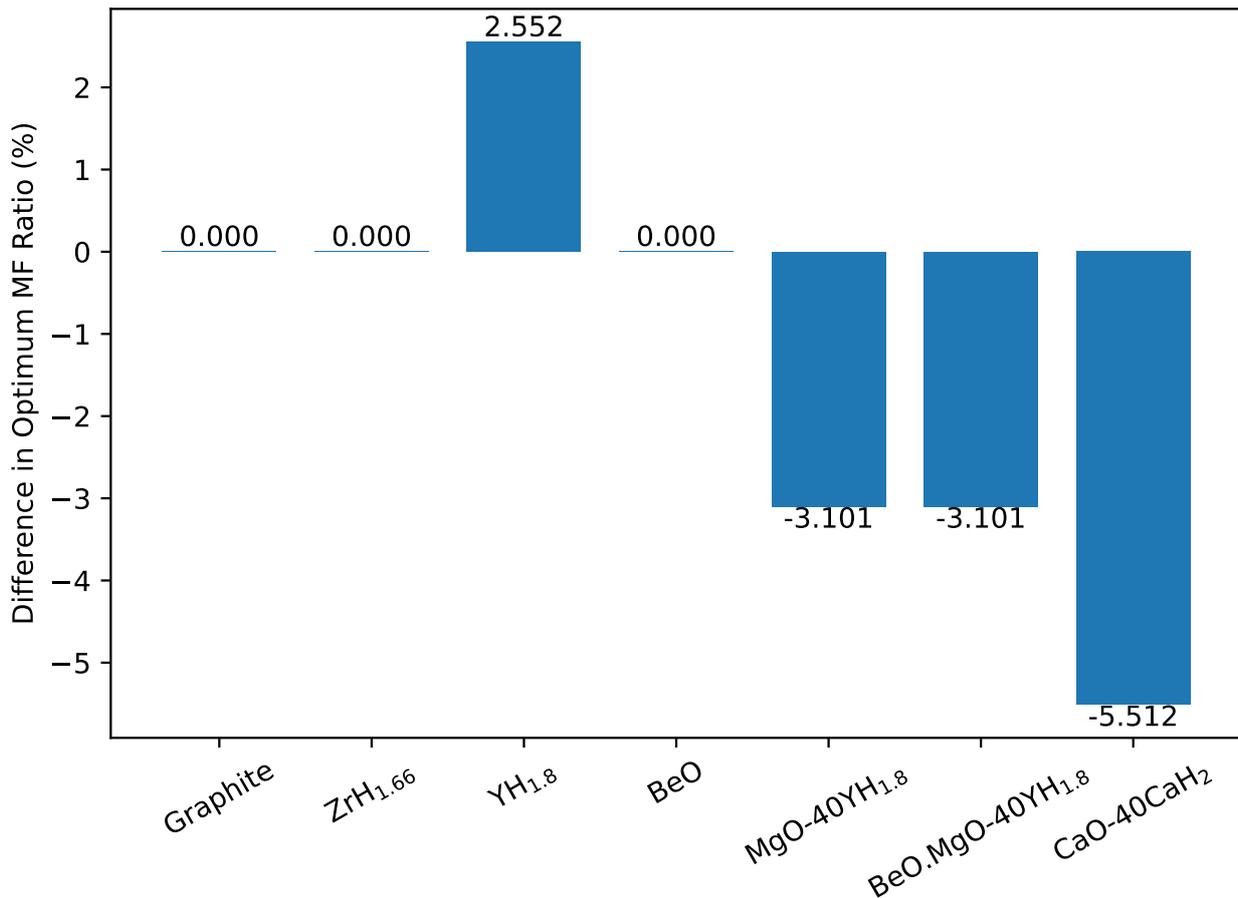
**Fig. 21.** Per Cent Difference of Beginning of Life Optimum Moderator to Fuel Ratios Between 19.75 % and 14.75 % Enriched UN Fuel with 99.5 % Enriched Nitrogen

For completeness, we also considered a case with 24.75 % enrichment. Figure 22 shows that the over trends are the same but reversed as with the case of 14.75 %. The explanations are also similar, except that monolithic moderators do not benefit from the enrichment increase because of the thermal neutron self-shielding of the UN fuel pellet. In other words, the moderated neutrons cannot cause fissions toward the centre of the fuel pellet because the uranium enrichment is high enough that the 235-U at the outer edges fissions first. This self-shielding is why highly enriched, fast neutron systems do not benefit from the addition of moderating materials. The self-shield is also dangerous because of the power peaking in a small volume at the periphery of the UN fuel pellet. Figure 23 shows the % difference in the MF ratios, and we see a dramatic change. The graphite optimum MF ratio has precipitously dropped. This drop in the MF ratio is because of the significant $K_{inf}$ change we saw in Figure 22, which leads to the $K_{inf}$ value at the MF volume ratio of 1 being larger than the $K_{inf}$ value at 25. In fact, graphite and BeO nearly equal the absolute BOL $K_{inf}$ of the monolithic composite moderators at the lowest MF ratio. This inversion indicates that a fast spectrum reactor is more favourable if the uranium enrichment exceeds 19.75 %. The lower mass and size of the resulting NSP reactor core would make a 24.75 % enriched fast reactor decidedly superior to 19.75 % enriched thermal reactors.
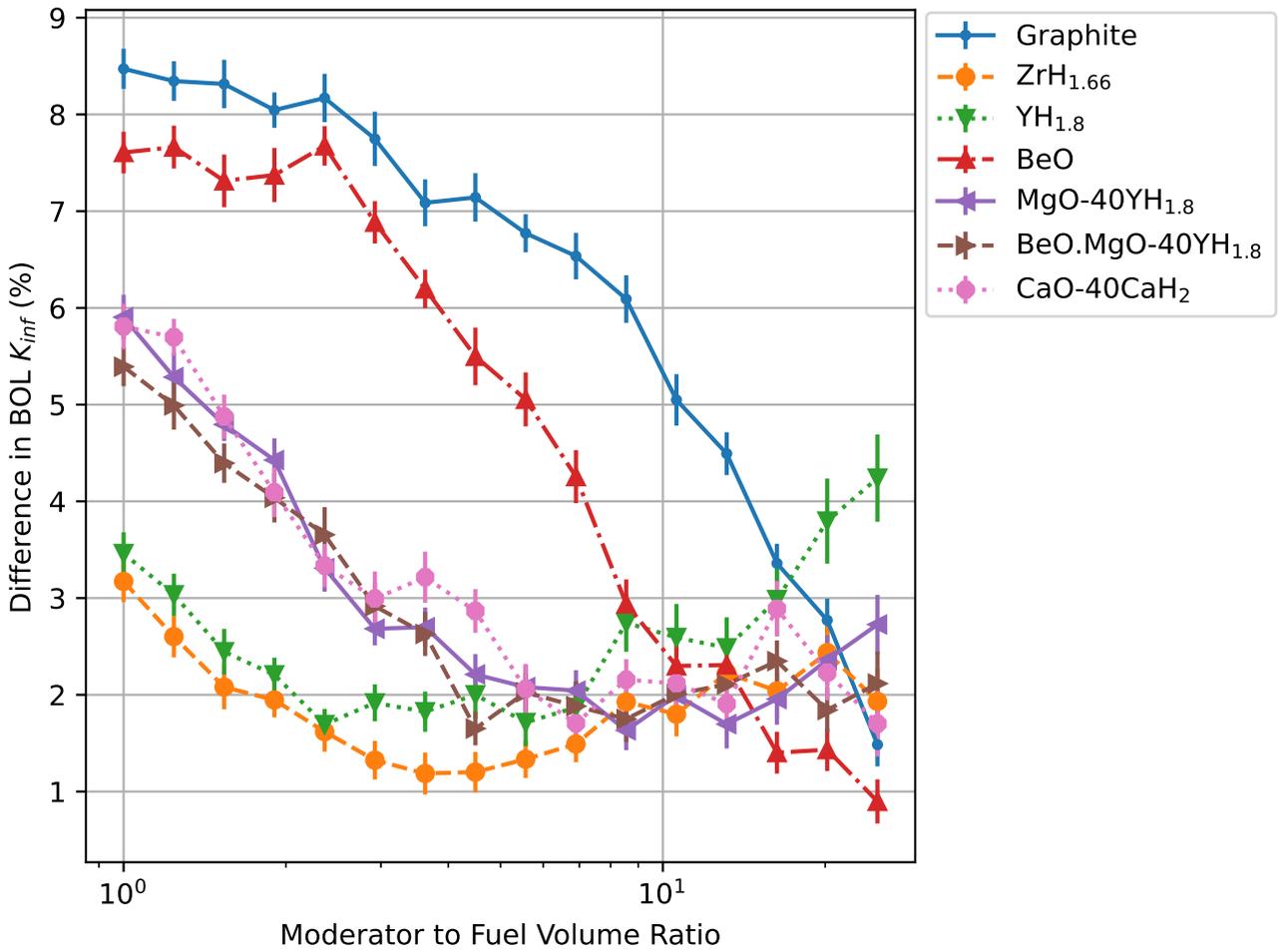
**Fig. 22.** Per Cent Difference of Beginning of Life Infinite Neutron Multiplication Factor Between 19.75 % and 24.75 % Enriched UN Fuel with 99.5 % Enriched Nitrogen
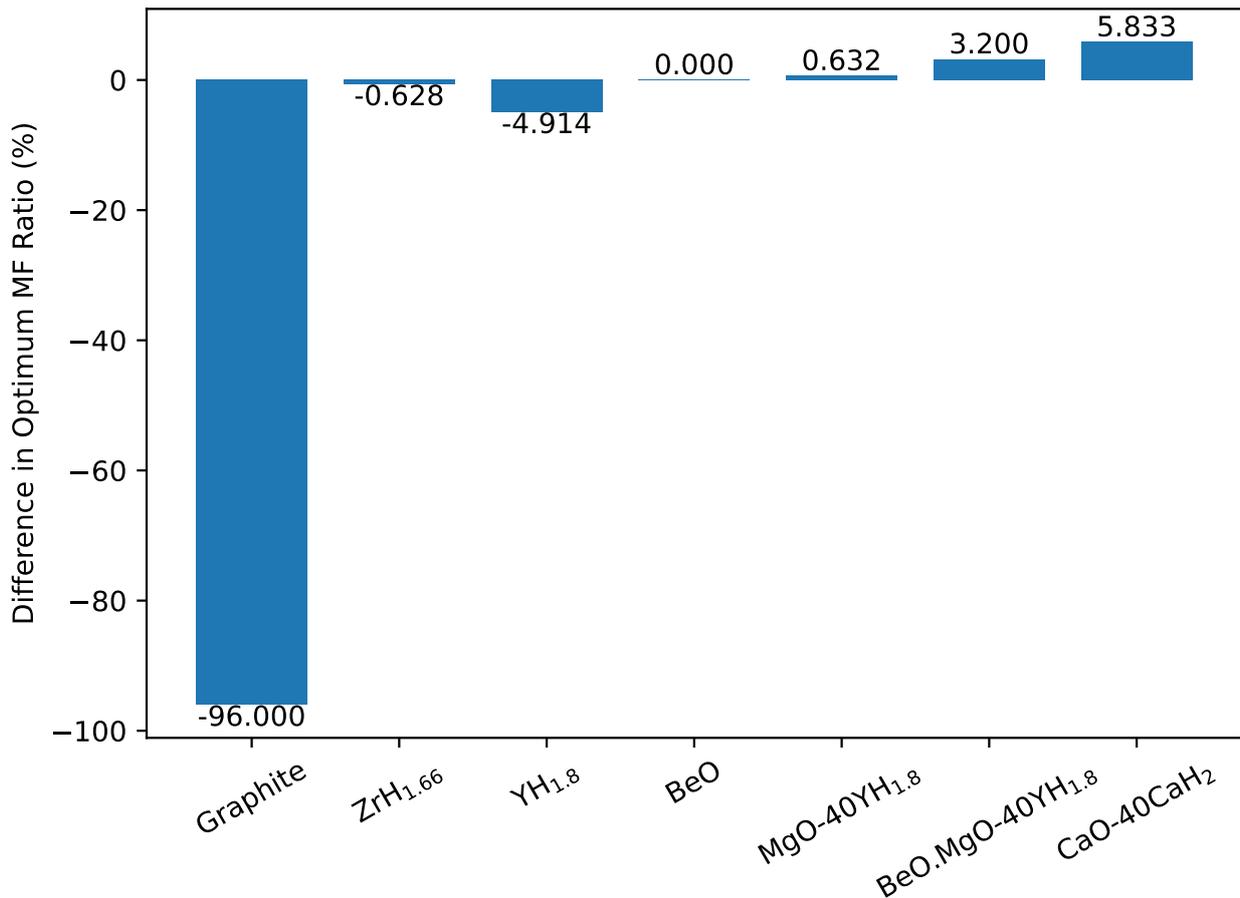
**Fig. 23.** Per Cent Difference of Beginning of Life Optimum Moderator to Fuel Ratios Between 19.75 % and 24.75 % Enriched UN Fuel with 99.5 % Enriched Nitrogen

Our final observation is a trend in Figures 21 and 23. As the uranium enrichment decreases, all the composite moderators' optimal MF volume ratio decreases. In contrast, the monolithic moderators behave oppositely. We believe high moderating efficiency and UN fuel self-shielding partly explain the trend for the monolithic moderators. However, we do not have a satisfactory explanation for the composite moderators' trend. We suggest reactor physics specialists investigate this trend further. In any case, the trend is valuable as it suggests that NSP reactor engineers can lower the uranium enrichment to reduce the reactor size, which is highly unusual.

As we move on to studying the impact of using natural nitrogen in the UN fuel, we remind the reader that the results presented in this section all used 99.5 % enriched nitrogen, and the reference uranium enrichment was 19.75 %.

## 5.2 Variable Nitrogen Enrichment Results

This section explores the impact of not enriching nitrogen for UN fuel. Figure 24 compares the BOL $K_{inf}$ values for 19.75 % enriched uranium fuel. We see a similar trend with increasing

MF volume ratio, and we note that the change affects all moderators equally. Figure 25 tells a similar story with a net increase in the optimal MF ratio for all moderators to compensate for the thermal neutron absorption of 14-N. Figures 26 and 27 show the $K_{inf}$ % differences for 14.75 and 24.75 % enriched uranium fuels. Although the graphs are primarily similar, we note the trend that the lower the uranium enrichment, the more significant the impact of the lack of nitrogen enrichment on the reduction of the BOL $K_{inf}$ and the increase of the optimum MF volume ratio.
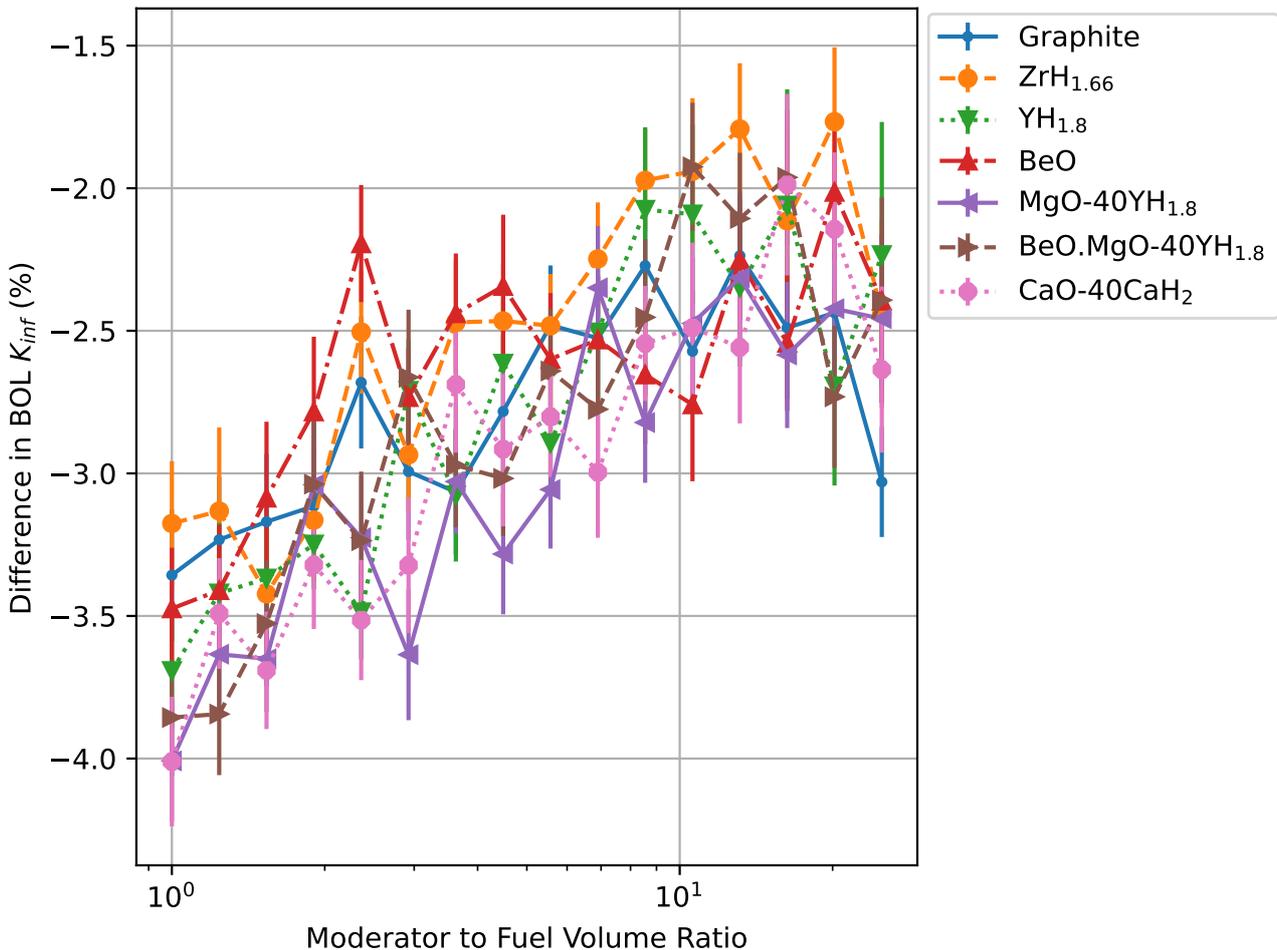


**Fig. 24.** Per Cent Difference of Beginning of Life Infinite Neutron Multiplication Factor for 19.75 % Enriched UN Fuel Between Natural Nitrogen and 99.5 % Enriched Nitrogen
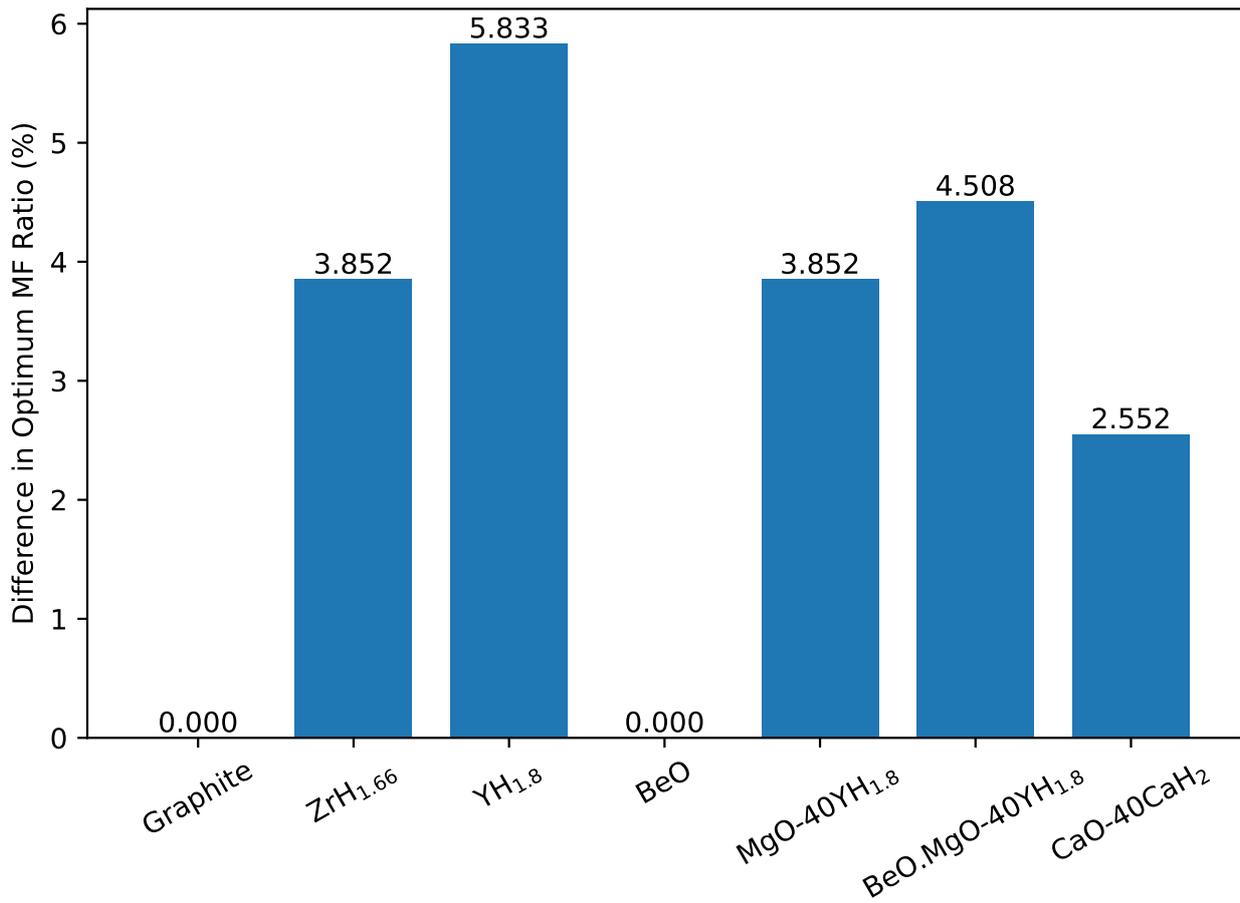
**Fig. 25.** Per Cent Difference of Beginning of Life Optimum Moderator to Fuel Ratios for 19.75 % Enriched UN Fuel Between Natural Nitrogen and 99.5 % Enriched Nitrogen
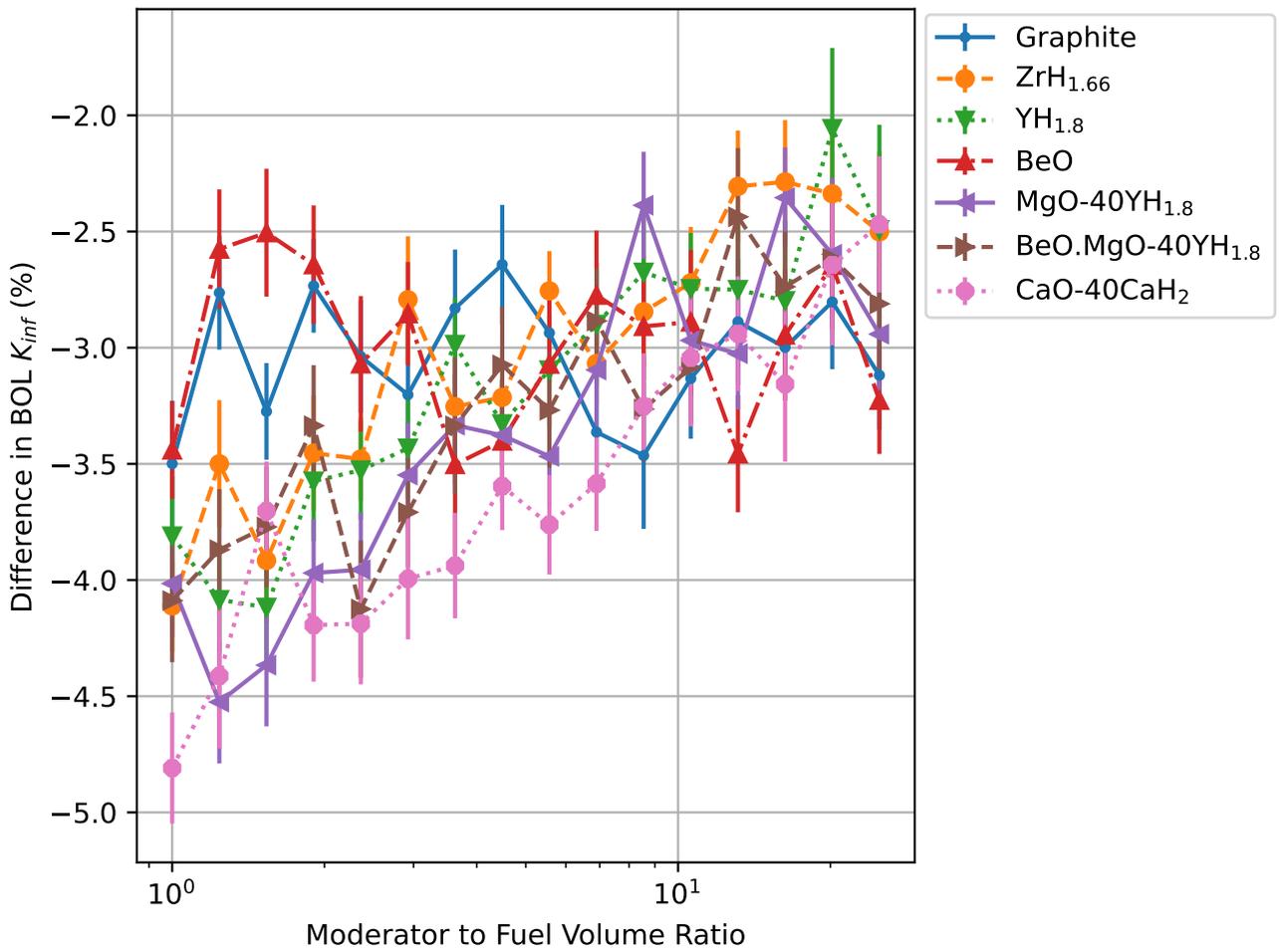
**Fig. 26.** Per Cent Difference of Beginning of Life Infinite Neutron Multiplication Factor for 14.75 % Enriched UN Fuel Between Natural Nitrogen and 99.5 % Enriched Nitrogen
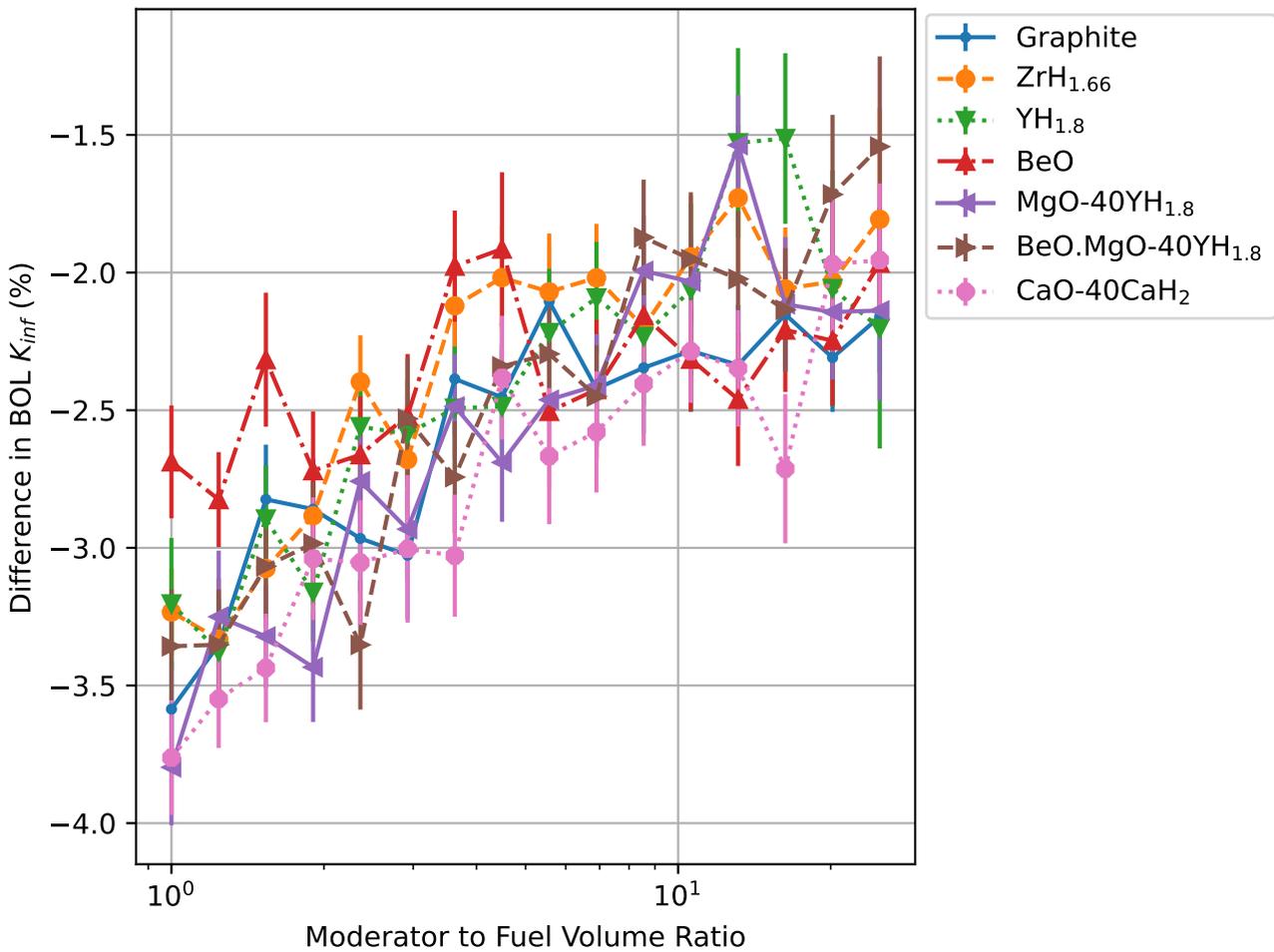
**Fig. 27.** Per Cent Difference of Beginning of Life Infinite Neutron Multiplication Factor for 24.75 % Enriched UN Fuel Between Natural Nitrogen and 99.5 % Enriched Nitrogen

## 5.3  Selection of Optimum Fuel Isotopic Composition

The large variety of the trends observed in this chapter makes it challenging to make particular recommendations. Here, we focus on working with uranium enrichments below 20 %, and therefore, we do not consider 24.75 % enriched uranium as a practical option due to nuclear safeguarding and non-proliferation concerns. Legal and political limitations notwithstanding, our results show that self-shielding effects begin to substantially diminish the utility of using a moderator in the reactor at high uranium enrichments. In other words, thermal spectrum reactors function best with HALEU or lower-enriched uranium.

Our results also show that 14.75 % enrichment has the advantage of lower optimum MF volume ratios for composite moderators. If the 4 % $K_{inf}$ penalty is tolerable, we suggest NSP reactor designers consider natural nitrogen 19.75 % enriched UN instead due to concerns surrounding enriched nitrogen supply. If the NSP reactor core possesses excessive extra reactivity, an 8 % penalty on the BOL $K_{inf}$ gets us natural nitrogen 14.75 % enriched UN instead. NSP reactor designers are recommended to review these results in the context of their reactor to understand if tradeoffs to reduce nitrogen and uranium enrichments could be

made to reduce the reactor's fuel costs dramatically.

Ultimately, we continue to use 19.75 % enriched UN with 99.5 % enriched nitrogen as the reference fuel, representing the most neutronically performant fuel option practically possible, considering legal and political constraints. As we head toward the end of our design workflow, the next chapter explores the remaining questions concerning the burnup at EOL, its variation with fuel enrichments, and the characteristics of assembled 3D NSP cores with the optimum MF volume ratios we presented in this chapter.

# 6 In-Depth Analysis of Moderator Options

Although the previous chapter discusses the results of our parametric OpenMC model, we modified it to explore the fundamentals of NSP reactor neutronics in greater detail. The extensions to the simulation model include depletion and BOL $K_{inf}$ studies of assembled 3D reactor cores to account for neutron leakage. We require these results to put the previous chapter's results in a more practical context and judge the effects of the loss of ideality in our reactor design. Further, we noted in Chapter 5 that there is a burnup limit of 8 % on the UN fuel pellets based on the experimental experience so far [19]. Hence, it is necessary to understand if our fuel pellets stay below 8 atom % burnup at EOL.

Following the last chapter's example, we initially thought to begin with a variable enrichment study. Our preliminary calculations suggested that a nitrogen enrichment variation study would not be required. Interestingly, the trends exhibited in the previous chapter were identical when the core was depleted at 275 W/cm for 10 years. The relative difference in BOL and EOL $K_{inf}$ was independent of the nitrogen enrichment. Unexpectedly, the EOL burnup was also insensitive to the nitrogen enrichment.

Further, we ignored the 24.75 % uranium enrichment level, deeming it impractical and unimplementable. The higher enrichment did not offer a substantial advantage to thermal spectrum reactor cores and would increase costs and regulatory hurdles. However, we reiterate that fast reactors using 24.75 % 235-U are worthy of investigation as a lightweight, increased power density and overall higher performance alternative to 19.75 % enriched thermal reactors. The results presented in this chapter reinforce that conclusion. Now, let us examine the 19.75 % enriched UN-fueled pin-in-cell fuel element in more detail.

## 6.1 Depletion and 3D Core Analysis for 19.75 % Enriched UN Fuel

First, we look at the EOL $K_{inf}$ results from our depletion simulation. The overall ordering of the moderators in Figure 28 compared to Figure 17 is the same. In Figure 29, we find that the more thermal the neutron spectrum, the lower the loss in reactivity. Each moderator exhibits a trough on the curve where neutron absorption balances the rate of neutron thermalisation. Graphite and BeO have a low neutron stopping power and low neutron absorption cross sections [30].
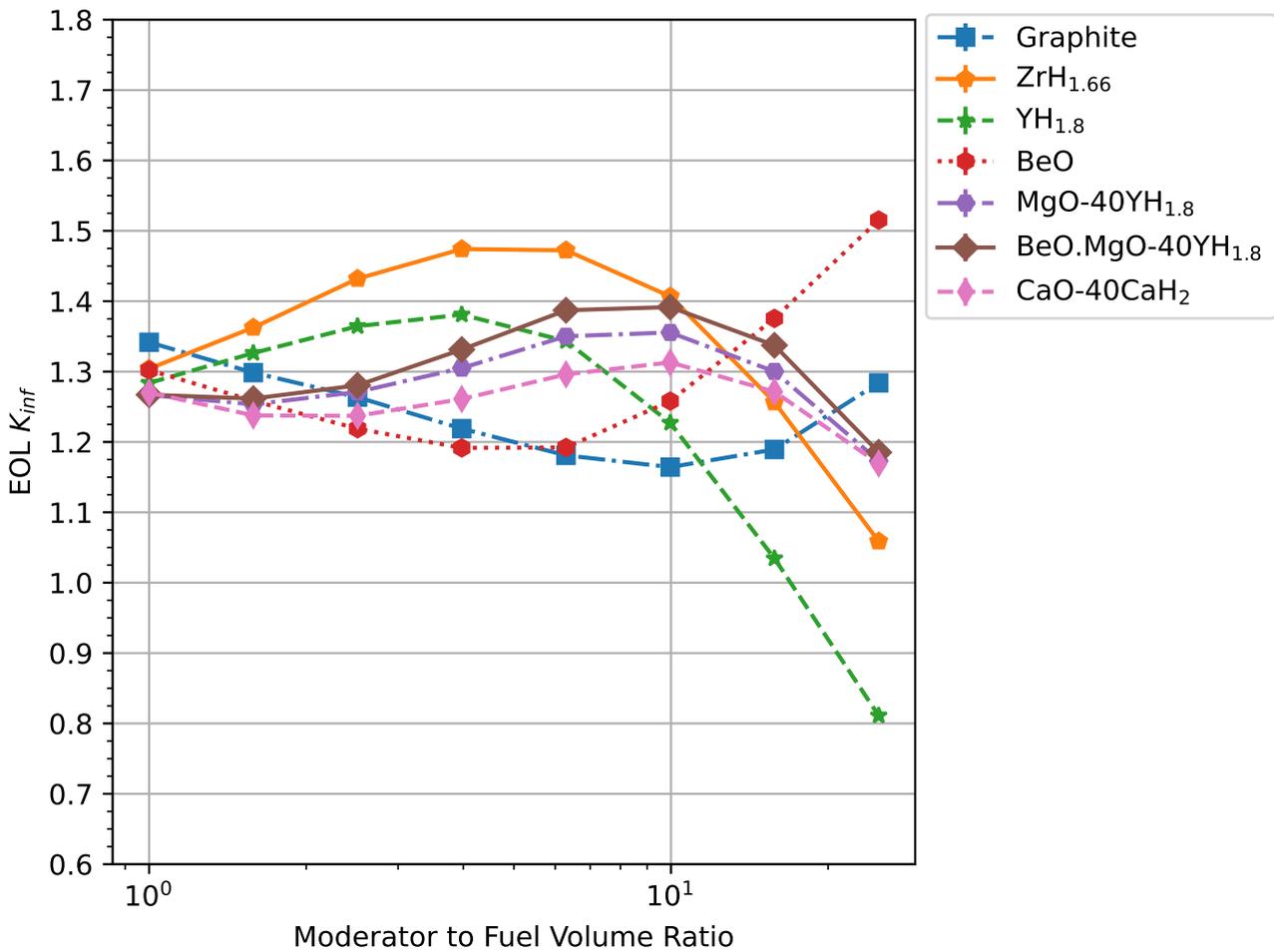
**Fig. 28.** End of Life Infinite Neutron Multiplication Factor for Pin-in-Cell Fuel Element with 19.75 % Enriched UN Fuel and 99.5 % Enriched Nitrogen (Error Bars not Visible)

The monolithic hydrides' hydrogen and rare earth metals absorb more neutrons because they have larger absorption cross sections and higher density. Thus, the EOL $K_{inf}$ is lower. Finally, the composite moderators have a non-moderating weak neutron absorber matrix. This matrix material increases the neutron absorption while decreasing the moderating power, leading to the most considerable reduction in EOL $K_{inf}$ as the MF volume ratio increases. Eventually, enough entrained metal hydride is present to balance the neutron absorption and moderation; thus, a visible trough for all the composite moderators is seen in Figure 29. Graphite and BeO have similar behaviour, though the trough occurs off the right side of the graph. At the same time, the monolithic moderators may not exhibit a trough because of their intrinsically coupled neutron absorption and neutron thermalisation rates.
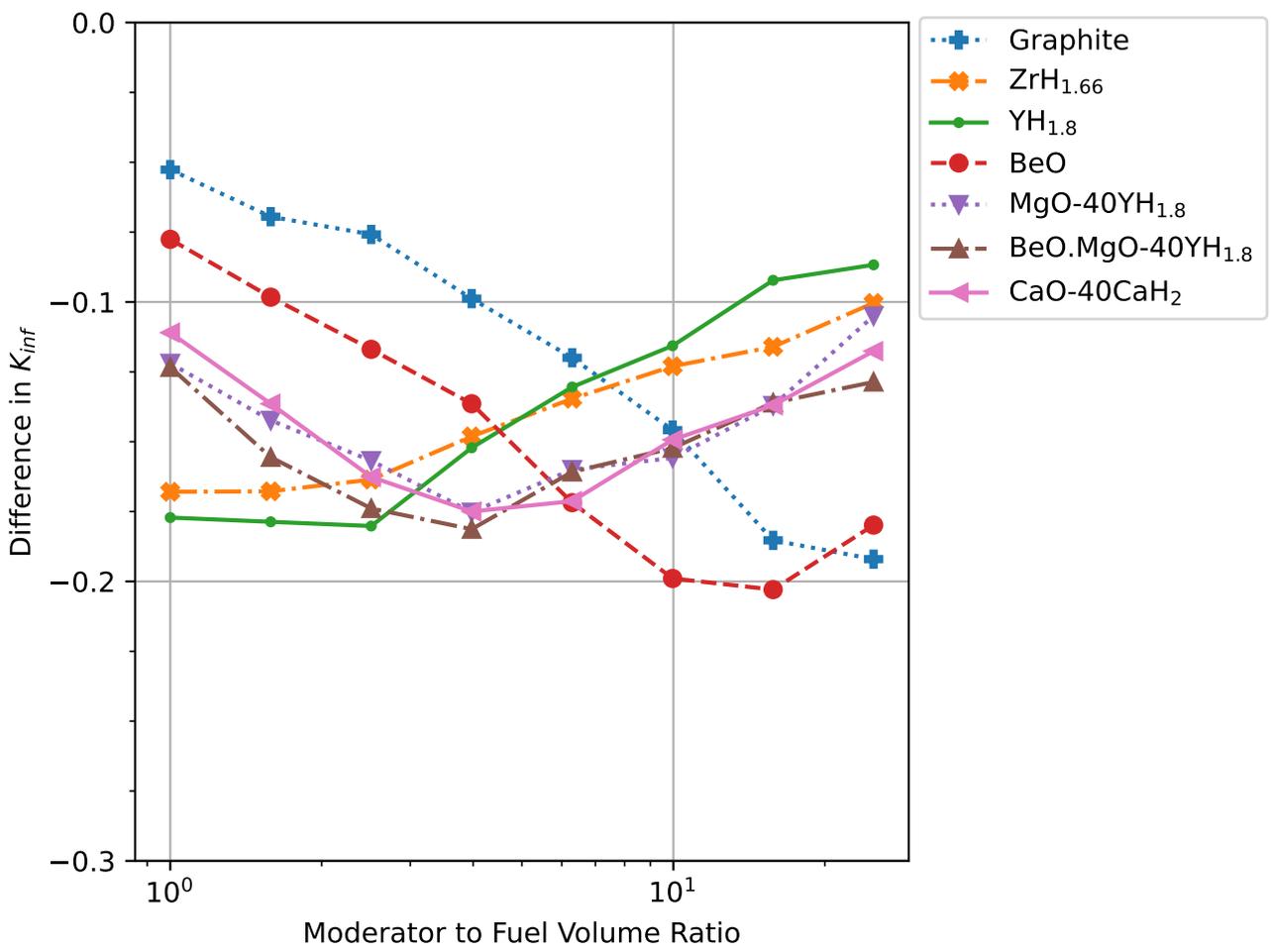
**Fig. 29.** Difference in Infinite Neutron Multiplication Factor for Pin-in-Cell Fuel Element with 19.75 % Enriched UN Fuel and 99.5 % Enriched Nitrogen
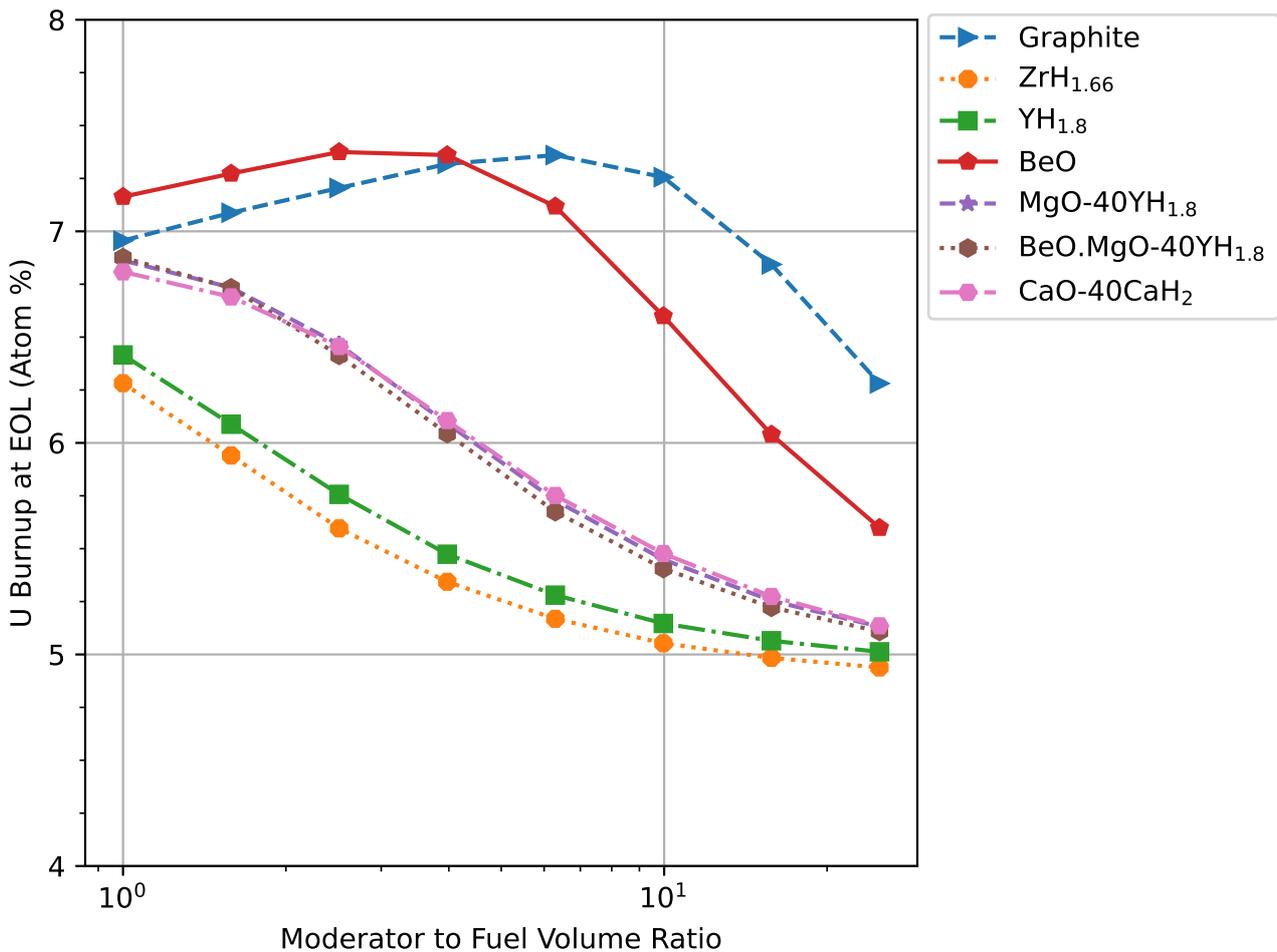
**Fig. 30.** Uranium Atom % Burnup at the End of Life for Pin-in-Cell Fuel Element with 19.75 % Enriched UN Fuel and 99.5 % Enriched Nitrogen

The EOL burnups shown in Figure 30 are a function of the thermal neutron economy. The more thermal the spectrum, the lower the burnup. Note that the model is still infinite; therefore, the fuel mass does not play a role in Figure 30. The weakest moderators, graphite and BeO, burn the most fuel to produce 275 W/cm. As the MF volume ratio increases, they begin to thermalise the spectrum, and the fission reaction becomes more efficient, sharply reducing the burnup.

The composite and monolithic moderators exhibited similar trends, though their high neutron stopping power means that even at very low MF volume ratios, the neutron spectrum is still thermal. Simply put, the burnup is determined by the number of neutrons moderated but not absorbed that proceed to fission uranium in the fuel. The independence of burnup from neutron absorption in the fuel is intriguing because it shows that the probability of uranium fission from a thermal neutron overshadows the probability of thermal neutron capture by natural nitrogen. As an instructive side note, $ZrH_{1.66}$ performs better than $YH_{1.8}$ despite its higher H/M ratio because of the increased thermal neutron absorption by yttrium [30] and the higher density of zirconium hydrides [66]. These observations increasingly demonstrate the need to separate moderation and absorption into concurrent and independent physical processes

to explain the simulation results, especially the behaviour of the composite moderators.

Provided the optimum MF volume ratios from the BOL $K_{inf}$ and noting that depletion did not change the optimum values, we can assemble 3D cores of optimal height [60] and radius for a given moderator and number of fuel element rings. We also use a BeO filler material in the void space of the circumscribing circle to closely emulate practical reactor designs which use BeO to reduce neutron leakage and provide structural support [4] [54]. Figure 31 shows an XY slice of a 7-ringed $YH_{1.8}$ core at its optimal MF volume ratio of 3.570. The region in red is the BeO wrapper. The mass and dimensions of the wrapper vary according to the number of fuel element (FE) rings in the 3D core and the optimal MF volume ratio. However, the neutronic impact is similar between different-sized cores of the same moderator.
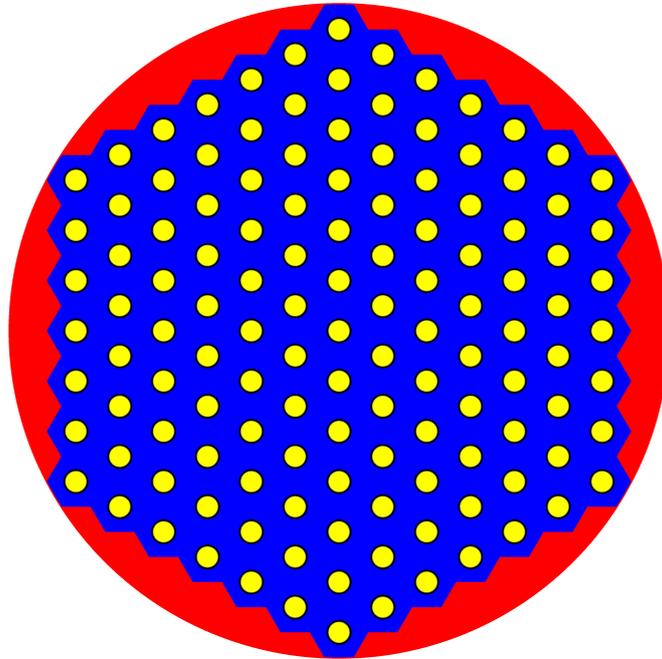
**Fig. 31.** XY Slice of a 7-Ringed 3D NSP Reactor Core with MF Volume Ratio of 3.57 and $YH_{1.8}$ Monolithic Moderator. The blue region is the moderator, and the red region is the BeO wrapper. The fuel cladding and coolant channels are not visible on this scale. This figure is to scale with each edge equal to 100 cm.

Here, we are interested in three things: the dimensions of the 3D core, its total mass and the minimum number of rings required for each moderator to produce a critical core with some excess reactivity at BOL. Figures 32 and 33 provide core radius and height data. Figure 34 provides the minimum 3D core mass for the optimum MF volume ratio. Finally, we cross-reference the BOL $K_{eff}$ from Figure 35 to interpret the above figures and look for the 3D cores that are also critical with excess reactivity. The graphite and BeO cores used an MF volume ratio of 1 to approximate the equivalent fast reactor core.
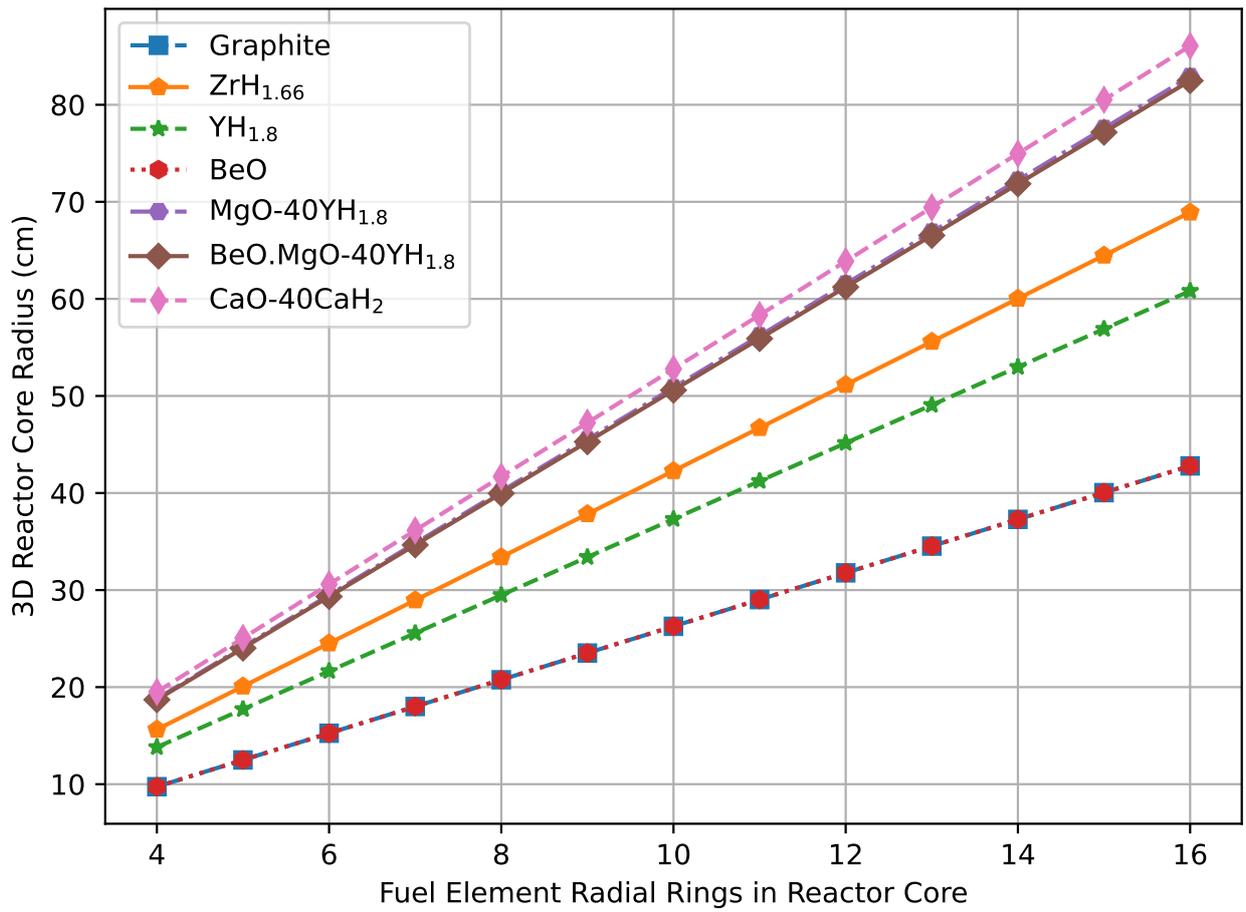
**Fig. 32.** 3D NSP Reactor Core Radius versus Number of Fuel Element Rings for 19.75 % Enriched UN Fuel with 99.5 % Enriched Nitrogen
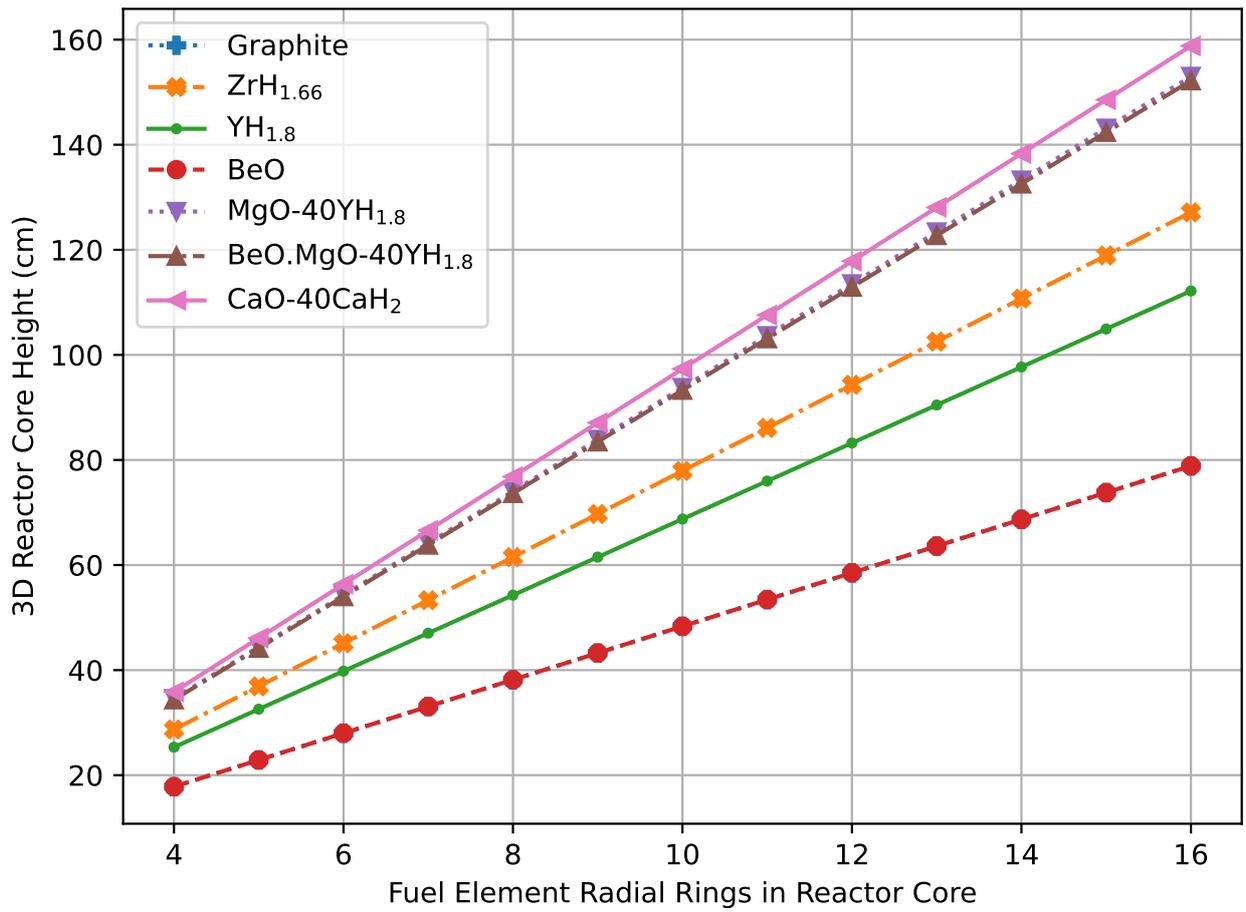
**Fig. 33.** 3D NSP Reactor Core Height versus Number of Fuel Element Rings for 19.75 % Enriched UN Fuel with 99.5 % Enriched Nitrogen
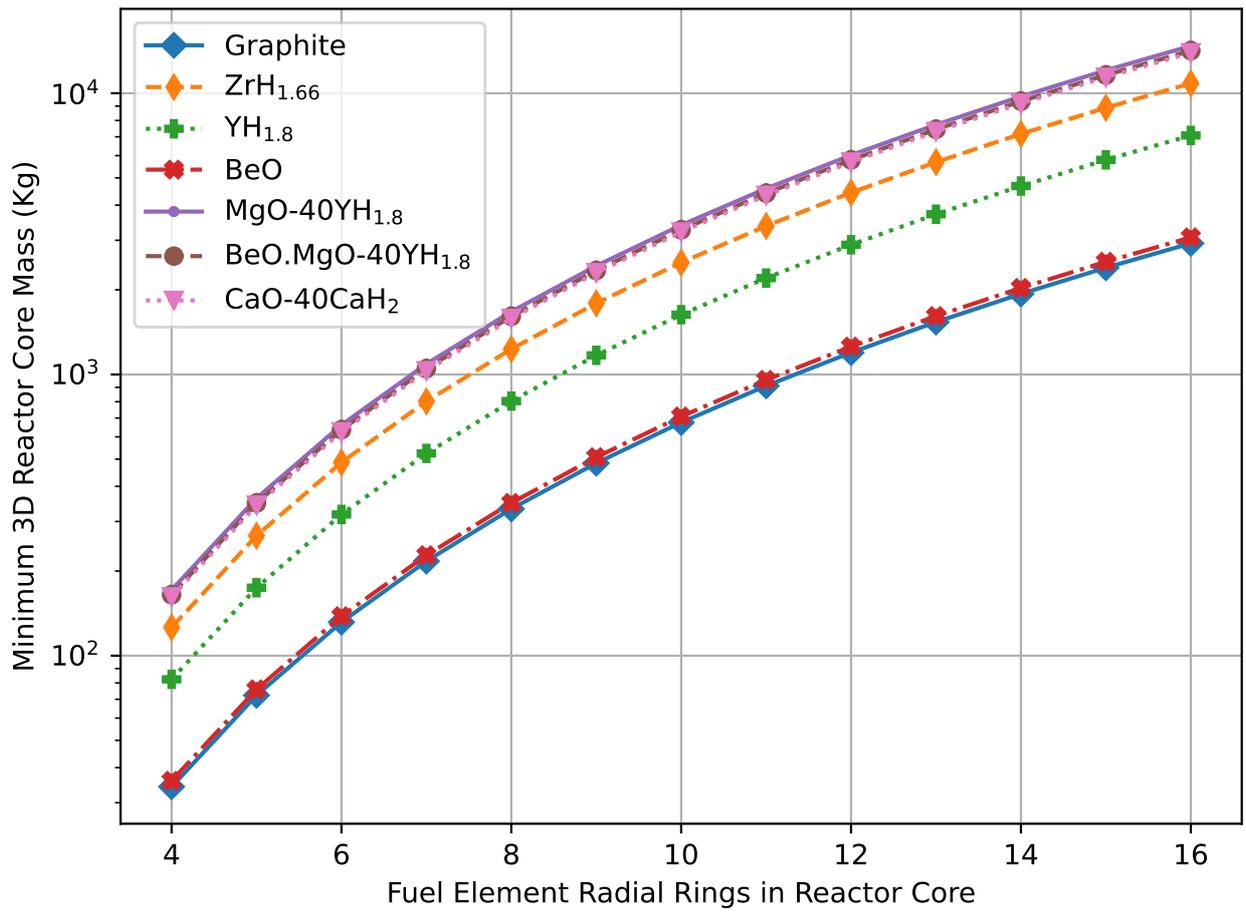
**Fig. 34.** Minimum 3D NSP Reactor Core Mass versus Number of Fuel Element Rings for 19.75 % Enriched UN Fuel with 99.5 % Enriched Nitrogen
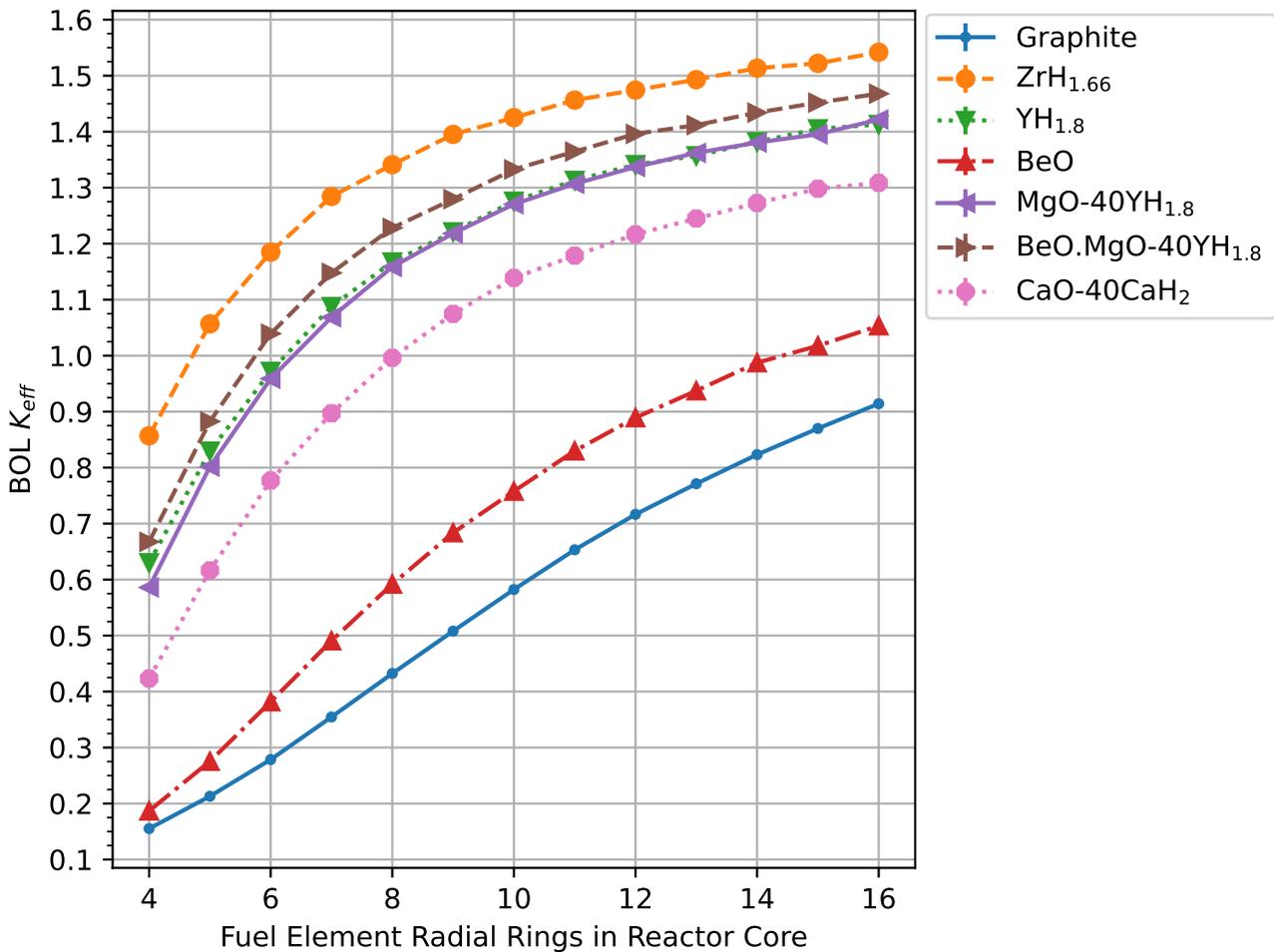
**Fig. 35.** 3D NSP Reactor Core $K_{eff}$ versus Number of Fuel Element Rings for 19.75 % Enriched UN Fuel with 99.5 % Enriched Nitrogen (Error Bars not Visible)

Table 2 from Chapter 1 reminds us that the target mass is below 2500 Kg and the target radius is under 60 cm. We can see from Figure 34 that only NSP reactor cores with less than 10 rings satisfy the mass limit, with the size being less limiting. However, Figure 35 shows that the CaO-CaH$_2$ composite moderator core does not have enough excess reactivity. This moderator's cores would be subcritical if the fuel used natural nitrogen. Surprisingly, our FE design suits YH$_{1.8}$ with its 50 cm core height at 7 rings and enough excess reactivity. Yttrium hydride produces the lightest critical cores, the 7-ringed variant being close to 500 Kg minimum mass. This trend seemingly contradicts Figure 19 from the last chapter, where we discussed the MF mass ratios. The NSP reactor designer would observe that the final 3D core mass trends differ from the MF mass ratio figures in the last chapter. Although the MF mass ratios predict that the composite moderator cores would be similar to ZrH$_{1.66}$, the core height is only a function of the MF volume ratio. Therefore, the overall core mass is firmly dependent on the MF volume ratio, not the MF mass ratio, which is unusual. Further, a significant fraction of the core minimum mass comprises the BeO structural support wrapper and reflector. We conclude that the MF mass ratios weakly influence the final 3D core mass.

We quickly note that using natural nitrogen in the fuel increases the core radius and height

by 1 to 2 % while reducing the $K_{eff}$ by 2 to 4 %. Due to the strong dependency of the core mass on the MF volume ratio, we found that the mass increase was double that, 2.75 to 5 %. Therefore, there is a sizeable penalty due to using natural nitrogen, even if more rings are not required. Next, we explore the differences between 14.75 % enriched fuel and 19.75 % enriched fuel.

## 6.2 Depletion and 3D Core Analysis for 14.75 % Enriched UN Fuel

Figures 36 and 37 show the depletion results for 14.75 % enriched UN fuel. We see a slight increase in the relative reduction in $K_{inf}$ between EOL and BOL; the trend observed earlier has been mildly exaggerated. More importantly, graphite and BeO have nearly breached the burnup limit of 8 atom %. As the MF volume ratio increases and neutron absorption overshadows the effects of the decrease 235-U, we see that Figures 30 and 37 become identical. Aside from these minor effects, the $K_{inf}$ depletion simulations satisfied the trends and differences between the systems discussed in the previous chapter.
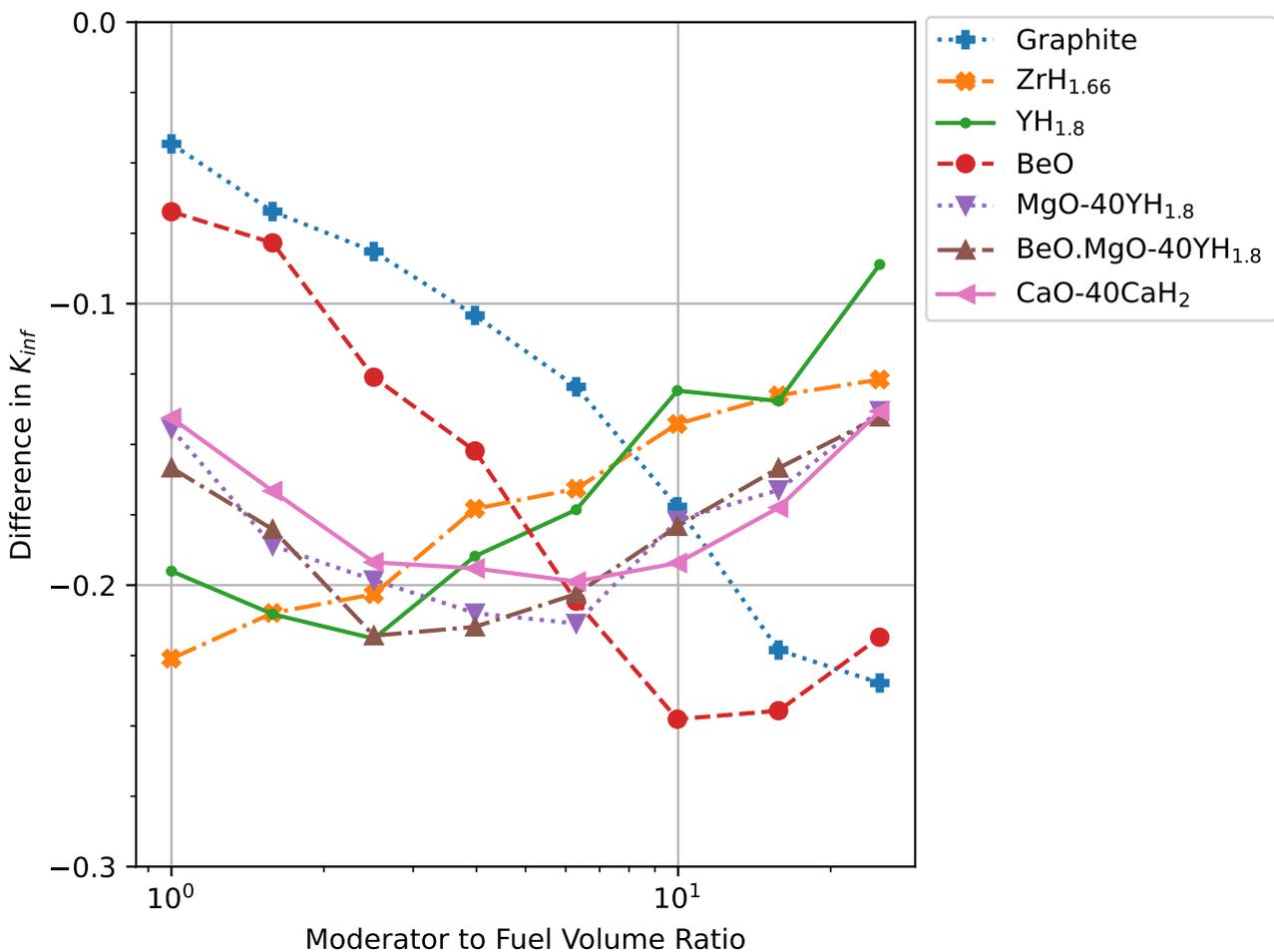


**Fig. 36.** Difference in Infinite Neutron Multiplication Factor for Pin-in-Cell Fuel Element with 14.75 % Enriched UN Fuel and 99.5 % Enriched Nitrogen
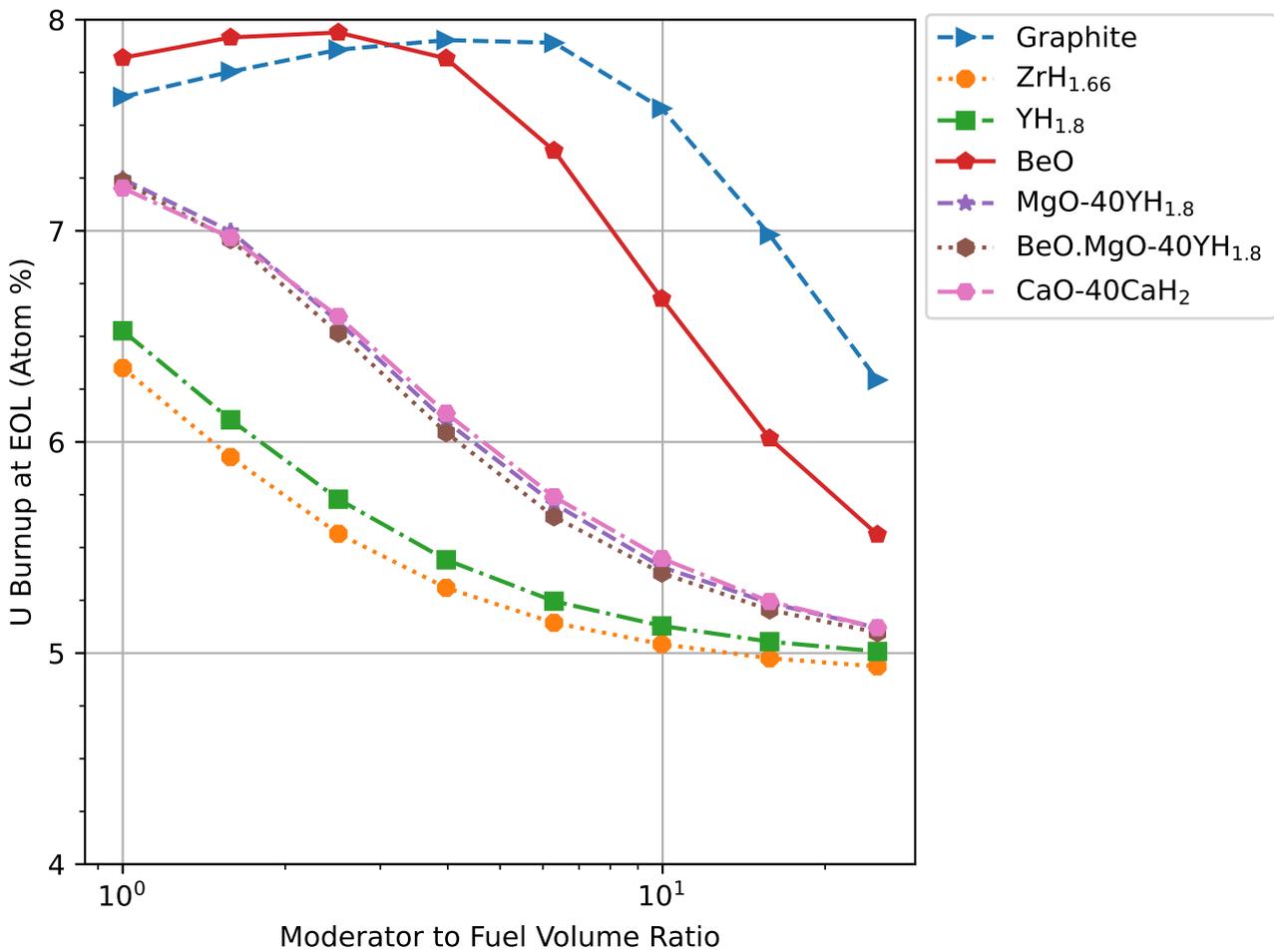
**Fig. 37.** Uranium Atom % Burnup at the End of Life for Pin-in-Cell Fuel Element with 14.75 % Enriched UN Fuel and 99.5 % Enriched Nitrogen

The most exciting results were comparing the reactor size, mass and $K_{eff}$ for 14.75 % enriched fuel with natural and enriched nitrogen. When the nitrogen was 99.5 % enriched, the trends expected from the BOL data analysis were held. Figure 38 shows the expected 2 to 4 % reduction, with graphite and BeO experiencing the most considerable shift. The smallest cores suffer the greatest from neutron leakage effects, which the BeO wrapper could not mitigate. Recall that as the uranium enrichment reduced, the optimum MF volume ratio increased for monolithic moderators and decreased for the composite moderators. Figure 39 shows that the reduction in the MF volume ratio for $CaO-CaH_2$ is substantial enough to reduce the minimum core mass by 6 %. If we compare the case with natural nitrogen enrichment, we find that there is still a net mass decrease of 2 %.
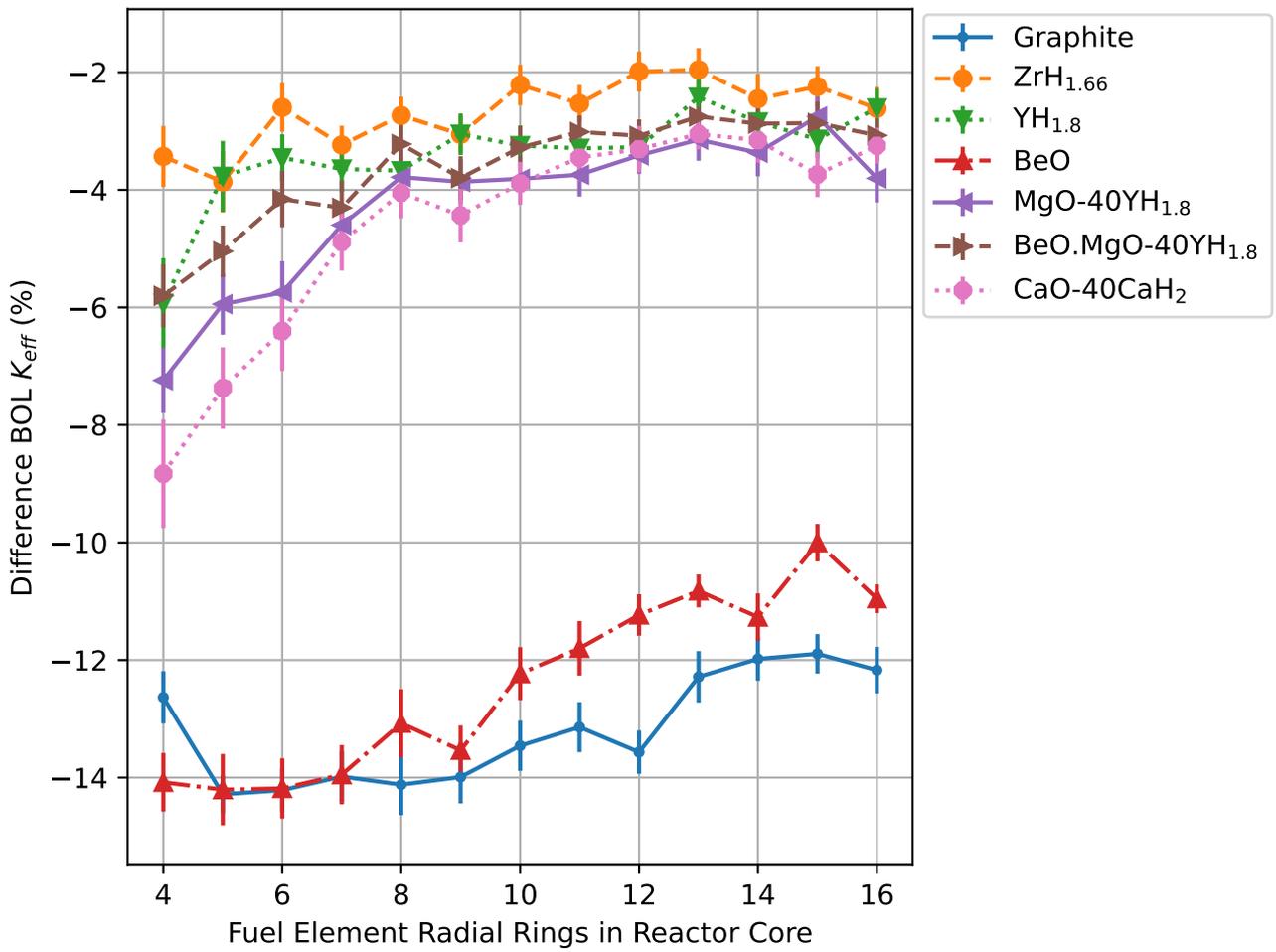
**Fig. 38.** 3D NSP Reactor Core $K_{eff}$ Difference versus Number of Fuel Element Rings Between 19.75 % and 14.75 % Enriched UN Fuel with 99.5 % Enriched Nitrogen
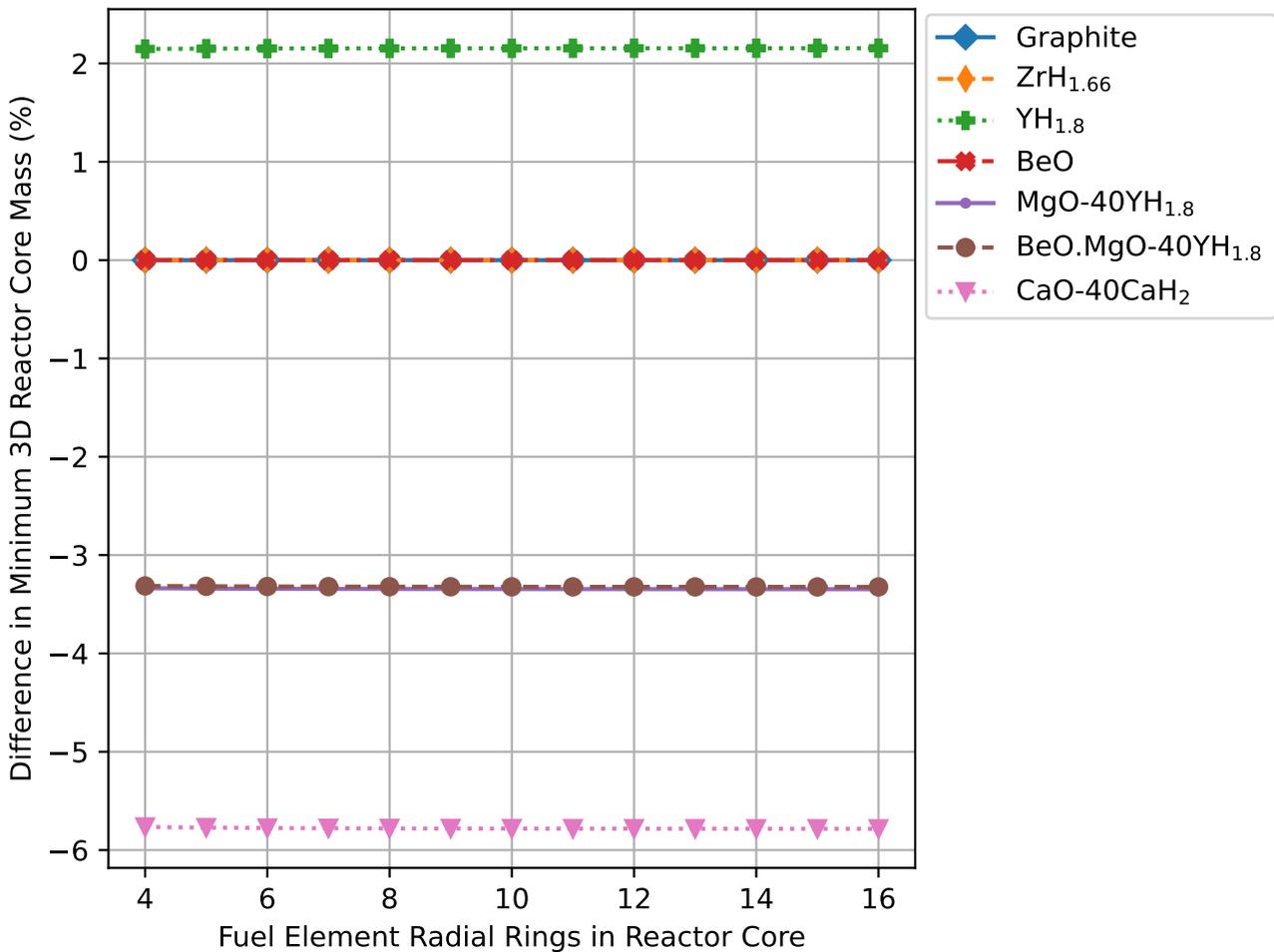
**Fig. 39.** Difference in Minimum 3D NSP Reactor Core Mass versus Number of Fuel Element Rings Between 14.75 % and 19.75 % Enriched UN Fuel with 99.5 % Enriched Nitrogen

Similarly, the power density has increased by a net 2 %, and the radius and height decreased by a net one per cent each. Figure 40 shows the net differences in the $K_{eff}$ between the reference fuel and natural nitrogen 14.75 % enriched UN. Referring to Figure 35, we also see that a net 7 % decrease in the BOL $K_{eff}$ would leave the leftover BOL excess reactivity in the 9-ring core with Cao-CaH$_2$ subcritical, and this core is not practical. However, these results show that the best and highest enrichment may not be the most compact or lightest core. Although the differences are within a few per cent, NSP reactor designers need not design a core with the optimal MF volume ratio, and our results show the power of reducing it even by a few per cent.
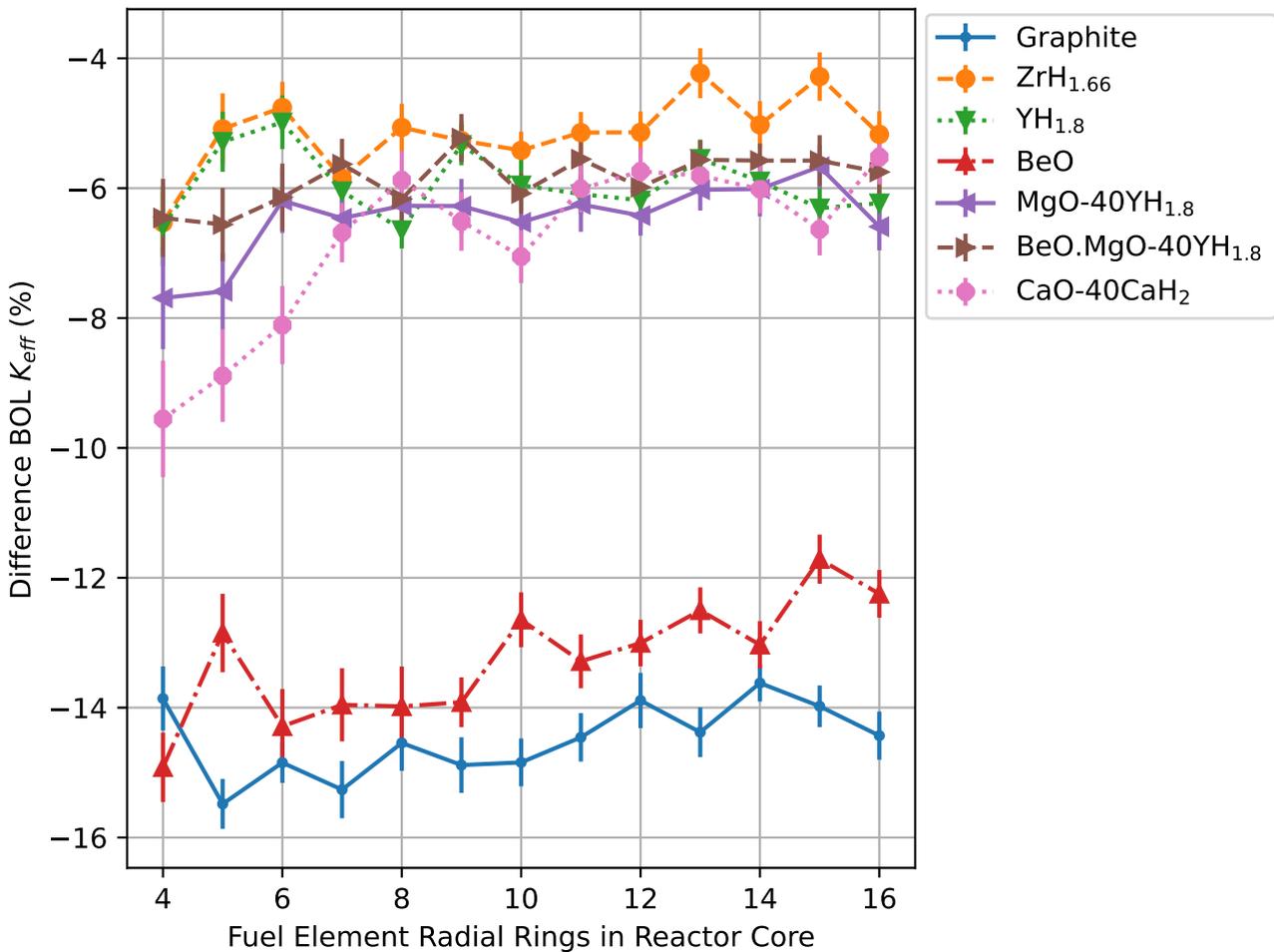
**Fig. 40.** 3D NSP Reactor Core $K_{eff}$ Difference versus Number of Fuel Element Rings for 14.75 % Enriched UN Fuel with Natural Nitrogen from the Reference Fuel Composition

## 6.3 Interpretation of Results and Trends

In this chapter, we have gained fascinating insights into the relationships between 3D core mass, size and fuel enrichment. We also understood the factors that affect EOL $K_{inf}$ and burnup. Initially, as we discussed the depletion results of the 19.75 % enriched fuel, we found that nitrogen enrichment did not affect burnup results and the difference between the EOL and BOL $K_{inf}$. The 14.75 % enriched fuel behaved similarly. As the moderation effect increased, the burnup at EOL reduced due to more efficient utilisation of the neutrons for fissioning the fuel. However, increasing neutron absorption with higher MF volume ratios washed out that effect. In the end, burnup values were higher for the 14.75 % case at low MF volume ratios, and the rate of decrease was steeper as the system was thermalised because of the stronger sensitivity of the system to the neutron economy due to its lower 235-U content.

Besides the depletion simulations, we also analysed the 3D NSP reactor core BOL $K_{eff}$ simulation results. The critical lesson we learnt was that the optimum MF volume ratio overshadowed all other parameters when determining the 3D core's size and mass. We found

that cores with less than 10 FE rings satisfied the criteria in Table 2, with the $YH_{1.8}$ core closely following our past calculations. Reductions in uranium and nitrogen enrichment led to smaller, lighter and more power dense cores if composite moderators were used, chiefly because of the reduction in the optimum MF volume ratio. Notably, there was a 6 to 8 % reduction in the BOL $K_{eff}$ for the 14.75 % enriched fuel with natural nitrogen with respect to the reference fuel. This reduction in $K_{eff}$ led to some cores becoming subcritical and negating the improvements in size and mass. Ultimately, we determined quantitatively how an NSP reactor designer can trade off $K_{eff}$ for reductions in size, mass and fuel enrichments to achieve the lightest, most compact and most cost-effective NSP reactor core design.

# 7 Synthesis of Results and Lessons Learnt

This chapter briefly summarises everything of note uncovered in our work. We began this thesis by justifying what NSP generation could achieve in deep space. Then, we set out to identify urgent and necessary applications of NSP systems and their approximate specifications. Once satisfied, we turned our attention to reactor materials to narrow the list of well-studied and characterised materials and fuels our reactor would use. With the rough specifications and partial materials limitations, we conducted rudimentary system-level thermodynamics and thermal hydraulics to establish temperature and thermal limits. These thermal limits informed us when we moved on to moderator material selection and designing our methodology to study them systematically. The final chapters presented the results of our OpenMC simulations, leading to this penultimate chapter.

## 7.1 Most Probable Choices for Reactor Materials and Specifications

The NSP systems designer is encouraged to revisit Tables 2 and 12. Our first chapter dealt with Solar Photo-Voltaic (SPV) systems and their evolution in space. We found that SPV systems struggled to compete with NSP generation at power generation levels greater than 100 KWe, but solar cells continue to improve and shed weight. Regardless, we found that a nuclear data communications relay was an urgent and necessary application of NSP systems, and we created Table 2, which placed spacecraft size and lifetime constraints on our design. The second Chapter briefly reviewed data on $UO_2$ and UN fuel forms, finding that $UO_2$ might prove better overall, but UN resulted in more compact cores due to its high uranium density. We found that the high temperatures reduced the number of structural and cladding materials we could consider. Most tungsten, rhenium, and tantalum refractory alloys heavily absorb thermal neutrons. We settled on MA 956 ODS steel and Mo-TZM on our final shortlist and continued with the steel because it absorbed fewer neutrons overall and was lighter. However, we had to note that the more robust and heavy-duty our structural materials were, the more the reactor would cost and weigh, and we ultimately left it to the NSP system designer to decide which materials were appropriate for their specific system.

## 7.2 Interplay of Reactor Materials, Lifetime and Thermodynamics

Chapter 3 was our first brush with engineering. We developed simple thermal hydraulics models of the Pin-in-Cell fuel element that we considered throughout our study. A discussion on selecting pure helium or HeXe followed and was not decisive. We continued with 40 g/mol HeXe to maintain applicability with legacy designs. Our thermal hydraulics model clearly showed that gas-cooled NSP reactors are at their operation limits, with 275 W/cm barely supported by the 0.75 $cm^2$ coolant channel. Switching the coolant to sodium made

the heat transfer isothermal, doubling the supported linear power. Despite the inadequate thermal conductivity, $UO_2$ fuel is better suited to NSP systems because the 1600 K temperature cap on UN resulted in low power densities with gas coolant. We learnt that thermal hydraulics supported a higher linear power when the coolant temperature was lower, in opposition to efficient heat rejection via a radiator in space. Later chapters showed little room to increase power densities with UN fuel because a linear power rating of 275 W/cm for the fuel pellets translated to the maximum burnup of 8 atom % after 10 years of operation. $UO_2$ fuel was less limited by burnup than UN. Overall, annular $UO_2$ fuel pellets would support higher power densities and easier heat rejection than UN but result in more massive reactors due to reduced uranium loading.

Our rudimentary heat engine models of the Brayton and Rankine cycles gave us fantastic insight. The mathematics developed for the Brayton cycle were simple enough to make rough guesses concerning system temperatures, power outputs and conversion efficiencies with predictive power. Our comparison singled out the inefficiencies of radiator heat rejection and heat injection into a gas coolant and the inadequate utilisation of the available radiator area by single-phase coolant. The solution to all these problems was isothermal heat injection and rejection provided by sodium in a Rankine cycle. In the end, while the power conversion efficiencies were similar, the Rankine cycle required smaller radiators, lower pressures and temperatures and supported much higher power densities while reducing system mass. We recommend that future NSP designers consider sodium Rankine cycles and, more generally, alkali metal cycles for second-generation NSP systems. Terrestrial sodium-cooled fast reactor systems stand to benefit the most from the theoretical and practical development of Rankine cycles for NSP systems in the coming years. In contrast, gas-cooled NSP systems do not have much to contribute to gas-cooled reactor designs on Earth.

Equipped with this knowledge, we began nuclear engineering to build a working reactor within the constraints. Chapter 4 discusses the level of experience and knowledge with various moderator materials. We narrowed the list of moderator materials to 7 options, including 3 composite moderators and one low-cost alternative with no rare earth metals. Using OpenMC's Python API, we designed a set of parametric simulation models, providing us with the optimum Moderator to Fuel (MF) volume ratios, MF mass ratios, and more. We found that these ratios are sensitive to uranium and nitrogen enrichment with complex trends, some unexplained. When interrogated in-depth, we observed the true power of the MF volume ratio in controlling the 3D reactor's size, mass and excess BOL reactivity. We found that for composite moderators, cores with lower uranium and nitrogen enrichment were slightly lighter and more power dense. Overall, we uncovered a complex interplay of the MF volume ratio, fuel enrichments, burnup and linear power density, which tied back into the thermal hydraulics. These interplays are complex to disentangle, and we hope our work has undone the first knot.

## 7.3 Nuclear Space Power System Design Workflow

We have noted before that legacy NSP system designs built the spacecraft and mission around the reactor concept, rarely giving ample consideration to justification, logistics and spacecraft thermal management. Our approach has done the opposite to illustrate this possibility and its advantages. The justification, logistics and thermals put fundamental constraints on our system design while ensuring our design methodology was modular and robust. The design workflow adopted in this thesis is general and enables an NSP system designer to deliver a system for any spacecraft and mission. The workflow we demonstrated uses only open-source, simple-to-use software for the preliminary design of an NSP system. We hope the reader can appreciate that although the resulting design is preliminary, it is still quite thorough. We hope this flexibility and modularity enable faster adoption of NSP generation in space in the coming decades.

## 7.4 Further Work and Scope for Improvements

Frequently, we have made assumptions in our simulations, decision-making criteria and applicability of our learning. The area of high-temperature, high-heat load thermal management for spacecraft requires more fundamental work than we could present here. Comparisons between more complex heat cycles with regeneration or recuperation would be helpful. Factoring in redundancy and its impact on system mass shall be critical for practical design exercises. The fidelity of our OpenMC simulations was intentionally low to facilitate the parametric calculation of numerous models. Future work can investigate if the trends and conclusions presented in this work hold up to a more exact analysis. Comparisons with MCNP, a respected Monte Carlo code and OpenMOC, an open-source deterministic code, would further support the validity of our results.

In this thesis, we found better materials, coolants and designs than the reference system we used. A restudy of the thermal hydraulics with $UO_2$ fuel would be extremely useful. Similarly, repeating the parametric analysis conducted here with $UO_2$ pellets would enable NSP designers to definitively conclude the rivalry between $UO_2$ and UN fuel forms. There are many other avenues for improvement in this work, but at this point, we conclude this chapter and hope that future NSP designers would build upon the work presented here.

# Bibliography

[1] M. Kaczmarzyk and M. Musiał, "Parametric study of a lunar base power systems," *Energies*, vol. 14, no. 4, p. 1141, 2021 (cited on pp. 11, 12, 14).

[2] A. Bermudez-Garcia, P. Voarino, and O. Raccurt, "Environments, needs and opportunities for future space photovoltaic power generation: A review," *Applied Energy*, vol. 290, p. 116 757, 2021 (cited on pp. 11, 12, 14, 15).

[3] Wikipedia, *New Horizons 2*, Mar. 2023. [Online]. Available: `https://en.wikipedia.org/wiki/New_Horizons_2` (cited on p. 11).

[4] D. I. Poston, M. A. Gibson, T. Godfroy, and P. R. McClure, "KRUSTY reactor design," *Nuclear Technology*, vol. 206, no. sup1, S13–S30, 2020 (cited on pp. 11, 24, 25, 75).

[5] M. Kuzlu, K. Abalos, O. Elma, O. Popescu, and M. Pipattanasomporn, "Modeling and simulation of the International Space Station (ISS) electrical power system," *International Transactions on Electrical Energy Systems*, vol. 31, no. 8, e12980, 2021 (cited on pp. 11, 15, 28).

[6] R. R. Hofer and T. M. Randolph, "Mass and cost model for selecting thruster size in electric propulsion systems," *Journal of Propulsion and Power*, vol. 29, no. 1, pp. 166–177, 2013 (cited on pp. 12, 16, 23).

[7] NASA, *Solar power technologies for future planetary science missions*, Dec. 2017. [Online]. Available: `https://solarsystem.nasa.gov/resources/548/solar-power-technologies-for-future-planetary-science-missions/` (cited on p. 13).

[8] J. Rodmann, A. Miller, M. Traud, K. D. Bunte, and M. Millinger, "Micrometeoroid impact risk assessment for interplanetary missions," in *Orbital Debris Conference*, 2019 (cited on pp. 14, 15).

[9] Camanes, *Study of the state of the art of space thermal control systems*, Jun. 2019. [Online]. Available: `https://ec.europa.eu/research/participants/documents/downloadPublic?documentIds=080166e5c802fe77&amp;appId=PPGMS` (cited on pp. 14, 16).

[10] J.-M. P. Tournier and M. S. El-Genk, "Liquid metal loop and heat pipe radiator for space reactor power systems," *Journal of propulsion and power*, vol. 22, no. 5, pp. 1117–1134, 2006 (cited on pp. 14, 35).

[11] J. Meseguer, I. Pérez-Grande, and A. Sanz-Andrés, *Spacecraft thermal control*. Elsevier, 2012 (cited on pp. 14, 24, 33).

[12] A. C. Marshall, J. H. Lee, W. H. Mcculloch, *et al.*, "Nuclear safety policy working group recommendations on nuclear propulsion safety for the space exploration initiative," Tech. Rep., 1993 (cited on pp. 15, 17).

[13]  NRC, *Typical spent fuel transportation casks*, 2023. [Online]. Available: `https://www.nrc.gov/waste/spent-fuel-storage/diagram-typical-trans-cask-system-2.pdf` (cited on p. 15).

[14]  Wikipedia, *Heavy-lift launch vehicle*, Aug. 2023. [Online]. Available: `https://en.wikipedia.org/wiki/Heavy-lift_launch_vehicle` (cited on pp. 15, 16).

[15]  R. D. Launius, "Reacting to nuclear power systems in space: American public protests over outer planetary probes since the 1980s," *Acta Astronautica*, vol. 96, pp. 188–200, 2014 (cited on p. 15).

[16]  J. D. Gylfe, "Nuclear power systems for advanced high-powered communications satellites," in *Progress in Astronautics and Rocketry*, vol. 19, Elsevier, 1966, pp. 501–528 (cited on p. 16).

[17]  M. Mammarella, P. M. Vernicari, C. A. Paissoni, and N. Viola, "How the Lunar Space Tug can support the cislunar station," *Acta Astronautica*, vol. 154, pp. 181–194, 2019 (cited on p. 16).

[18]  S. Berrezzoug, A. Boudjemai, and F. T. Bendimerad, "Interactive design and multidisciplinary optimization of geostationary communication satellite," *International Journal on Interactive Design and Manufacturing (IJIDeM)*, vol. 13, no. 4, pp. 1519–1540, 2019 (cited on pp. 16, 23).

[19]  A. Peakman and B. Lindley, "A review of nuclear electric fission space reactor technologies for achieving high-power output and operating with HALEU fuel," *Progress in Nuclear Energy*, vol. 163, p. 104 815, 2023 (cited on pp. 18–20, 23, 24, 54, 71).

[20]  M. S. El-Genk and J.-M. Tournier, "A review of refractory metal alloys and mechanically alloyed-oxide dispersion strengthened steels for space nuclear power systems," *Journal of Nuclear materials*, vol. 340, no. 1, pp. 93–112, 2005 (cited on pp. 18, 20, 21).

[21]  V. Bobkov, L. Fokin, E. Petrov, V. Popov, V. Rumiantsev, and A. Savvatimsky, "Thermophysical properties of materials for nuclear engineering: A tutorial and collection of data," *IAEA, Vienna*, 2008 (cited on pp. 18–21, 31, 52).

[22]  S. K. Rutledge, B. A. Banks, M. J. Mirtich, *et al.*, "High temperature radiator materials for applications in the low Earth orbital environment," National Aeronautics and Space Administration, Cleveland, OH (United States …, Tech. Rep., 1994 (cited on p. 18).

[23]  M. S. El-Genk and J.-M. Tournier, "Noble-gas binary mixtures for closed-Brayton-cycle space reactor power systems," *Journal of Propulsion and Power*, vol. 23, no. 4, pp. 863–873, 2007 (cited on pp. 18, 23, 24, 26, 28).

[24]  C. W. Bale and E. Bélisle, *Factweb*, 2016. [Online]. Available: `https://www.crct.polymtl.ca/factweb.php` (cited on p. 18).

[25]  G. Vasudevamurthy and A. T. Nelson, "Uranium carbide properties for advanced fuel modeling–A review," *Journal of Nuclear Materials*, vol. 558, p. 153 145, 2022 (cited on p. 19).

[26] B. D. Rogozkin, N. M. Stepennova, and A. A. Proshkin, "Mononitride fuel for fast reactors," *Atomic Energy*, vol. 95, no. 3, pp. 624–636, 2003 (cited on pp. 19, 20).

[27] B. J. Makenas, D. M. Paxton, S. Vaidyanathan, M. Marietta, and C. W. Hoth, "SP-100 Fuel Pin Performance: Results from Irradiation Testing," in *AIP Conference Proceedings*, vol. 301, American Institute of Physics, 1994, pp. 403–412 (cited on pp. 19, 20).

[28] R. B. Matthews, "Irradiation performance of nitride fuels," Los Alamos National Lab., NM (United States), Tech. Rep., 1993 (cited on pp. 20, 31).

[29] C. Ekberg, D. Ribeiro Costa, M. Hedberg, and M. Jolkkonen, "Nitride fuel for Gen IV nuclear power systems," *Journal of radioanalytical and nuclear chemistry*, vol. 318, pp. 1713–1725, 2018 (cited on p. 20).

[30] V. F. Sears, "Neutron scattering lengths and cross sections," *Neutron news*, vol. 3, no. 3, pp. 26–37, 1992 (cited on pp. 21, 50, 59, 71, 74).

[31] L. L. Snead, D. Sprouster, B. Cheng, *et al.*, "Development and potential of composite moderators for elevated temperature nuclear applications," *Journal of Asian Ceramic Societies*, vol. 10, no. 1, pp. 9–32, 2022 (cited on pp. 22, 48, 50).

[32] B. Cheng, E. M. Duchnowski, D. J. Sprouster, L. L. Snead, N. R. Brown, and J. R. Trelewicz, "Ceramic composite moderators as replacements for graphite in high temperature microreactors," *Journal of Nuclear Materials*, vol. 563, p. 153 591, 2022 (cited on pp. 22, 48, 49).

[33] A. T. T., *Beryllium-a unique material in nuclear applications*. Citeseer, 2004 (cited on p. 22).

[34] A. Mazzetti, M. G. Pret, G. Pinarello, L. Celotti, M. Piskacev, and A. Cowley, "Heat to electricity conversion systems for moon exploration scenarios: A review of space and ground technologies," *Acta Astronautica*, vol. 156, pp. 162–186, 2019 (cited on p. 23).

[35] C. Toro and N. Lior, "Analysis and comparison of solar-heat driven Stirling, Brayton and Rankine cycles for space power generation," *Energy*, vol. 120, pp. 549–564, 2017 (cited on pp. 24, 34, 35).

[36] J. K. Fink and L. Leibowitz, "Thermodynamic and transport properties of sodium liquid and vapor," Argonne National Lab., Tech. Rep., 1995 (cited on pp. 24, 38, 40).

[37] H. U. Borgstedt, "Influence of liquid sodium on mechanical properties of steels, refractory alloys and ceramics," in *Materials Issues for Generation IV Systems: Status, Open Questions and Challenges*, Springer, 2008, pp. 461–480 (cited on p. 24).

[38] J. G. Slaby, B. L. Siegel, L. Gedeon, and R. J. Galbo, "Irradiation of three t-111 clad uranium nitride fuel pins for 8070 hours at 990 c (1815 f)," Tech. Rep., 1973 (cited on pp. 25, 52, 54).

[39] N. Read, "Nuclear electric propulsion with low enriched uranium," PhD Thesis, University of Cambridge, 2020 (cited on pp. 26, 55).

[40] F. Zhao, Y. Mei, T. Liang, B. Wang, H. Jing, and W. Chen, "A Review on Heat Transfer Characteristics and Enhanced Heat Transfer Technology for Helium–Xenon Gas Mixtures," *Energies*, vol. 16, no. 1, p. 68, 2022 (cited on pp. 26, 28, 31, 97).

[41] P. K. Johnson, "A method for calculating viscosity and thermal conductivity of a helium-xenon gas mixture," *NASA Center for AeroSpace Information*, 2006 (cited on pp. 26, 97).

[42] B. M. Gallo and M. S. El-Genk, "Brayton rotating units for space reactor power systems," *Energy conversion and management*, vol. 50, no. 9, pp. 2210–2232, 2009. [Online]. Available: `https://www.sciencedirect.com/science/article/pii/S0196890409001733` (visited on 09/26/2023) (cited on p. 28).

[43] F. A. Di Bella and K. D. Fairman, "Development of a 240,000 kg/Day Hydrogen Pipeline Centrifugal Compressor for the Department of Energy's Hydrogen Delivery and Production Program," in *ASME International Mechanical Engineering Congress and Exposition*, vol. 45226, American Society of Mechanical Engineers, 2012, pp. 115–121 (cited on p. 28).

[44] R. E. Masterson, *Nuclear reactor thermal hydraulics: An introduction to nuclear heat transfer and fluid flow*. CRC Press, 2019 (cited on pp. 29, 31).

[45] K. Shinozaki, C. Y. Kang, Y. C. Kim, M. Aritoshi, T. H. North, and Y. Nakao, "The metallurgical and mechanical properties of ODS alloy MA 956 friction welds," *Welding Journal-Including Welding Research Supplement*, vol. 76, no. 8, pp. 287–299, 1997 (cited on p. 31).

[46] Staff, "Equations, tables, and charts for compressible flow," NASA Ames Research Center, Tech. Rep., 1953 (cited on p. 35).

[47] J. S. Smith and A. P. Watson, "Design, Manufacture, And Testing Of A High Speed 10 MW Permanent Magnet Motor And Discussion Of Potential Applications.," in *Proceedings of the 35th Turbomachinery Symposium*, Texas A&M University. Turbomachinery Laboratories, 2006 (cited on p. 36).

[48] M. S. El-Genk, "Space nuclear reactor power system concepts with static and dynamic energy conversion," *Energy Conversion and Management*, vol. 49, no. 3, pp. 402–411, 2008 (cited on p. 38).

[49] M. S. El-Genk, J.-M. P. Tournier, and B. M. Gallo, "Dynamic simulation of a space reactor system with closed Brayton cycle loops," *Journal of propulsion and power*, vol. 26, no. 3, pp. 394–406, 2010 (cited on p. 38).

[50] J. K. Fink, "Tables of thermodynamic properties of sodium," Argonne National Lab.(ANL), Argonne, IL (United States), Tech. Rep., 1982 (cited on pp. 38, 40, 44, 97).

[51] W. M. Phillips, "Some alkali metal corrosion effects in a rankine cycle test loop," in *Corrosion by Liquid Metals: Proceedings of the Sessions on Corrosion by Liquid Metals of the 1969 Fall Meeting of the Metallurgical Society of AIME, October 13–16, 1969, Philadelphia, Pennsylvania*, Springer, 1970, pp. 197–215 (cited on p. 42).

[52] A. P. Shivprasad, E. P. Luther, and V. R. Dasari, "Hydrogen loss from clad metal hydride moderators," Los Alamos National Lab.(LANL), Los Alamos, NM (United States), Tech. Rep., 2022 (cited on p. 48).

[53] Z. Wang, F. Liu, Z. Guo, J. Zhang, L. Wang, and G. Yan, "Advance in and prospect of moderator materials for space nuclear reactors," *International Journal of Energy Research*, vol. 45, no. 8, pp. 11 493–11 509, 2021 (cited on p. 48).

[54] M.-d. Hou, X.-w. Zhou, and B. Liu, "Beryllium oxide utilized in nuclear reactors: Part I: Application history, thermal properties, mechanical properties, corrosion behavior and fabrication methods," *Nuclear Engineering and Technology*, 2022 (cited on pp. 50, 75).

[55] A. T. Chapman, "Phase Studies in BeO–Metal Oxide Systems Using a Porous-Collector Technique," *Journal of the American Ceramic Society*, vol. 46, no. 4, pp. 171–174, 1963 (cited on p. 50).

[56] S. Balakrishnan, T. D. Humphries, M. Paskevicius, and C. E. Buckley, "Thermodynamic and kinetic properties of calcium hydride," *International Journal of Hydrogen Energy*, 2023 (cited on p. 50).

[57] J. E. Bird, T. D. Humphries, M. Paskevicius, L. Poupin, and C. E. Buckley, "Thermal properties of thermochemical heat storage materials," *Physical Chemistry Chemical Physics*, vol. 22, no. 8, pp. 4617–4625, 2020 (cited on p. 50).

[58] R. Kimura and S. Wada, "Temperature Reactivity Control of Calcium Hydride–Moderated Small Reactor Core with Poison Nuclides," *Nuclear Science and Engineering*, vol. 193, no. 9, pp. 1013–1022, 2019 (cited on p. 50).

[59] R. H. Borgwardt, "Sintering of nascent calcium oxide," *Chemical Engineering Science*, vol. 44, no. 1, pp. 53–60, 1989 (cited on p. 50).

[60] S. Reed and E. Kisi, "Miscibility gap alloys with a ceramic matrix for thermal energy storage," *SN Applied Sciences*, vol. 2, pp. 1–9, 2020 (cited on pp. 50, 75).

[61] P. K. Romano, N. E. Horelik, B. R. Herman, A. G. Nelson, B. Forget, and K. Smith, "OpenMC: A state-of-the-art Monte Carlo code for research and development," *Annals of Nuclear Energy*, vol. 82, pp. 90–97, 2015 (cited on p. 53).

[62] J. Yu and B. Forget, "Verification of depletion capability of OpenMC using VERA depletion benchmark," *Annals of Nuclear Energy*, vol. 170, p. 108 973, 2022 (cited on p. 53).

[63] G. Gunow, S. Shaner, W. Boyd, B. Forget, and K. Smith, "Accuracy and performance of 3d moc for full-core pwr problems," 2017 (cited on p. 53).

[64]  W. Boyd, S. Shaner, L. Li, B. Forget, and K. Smith, "The openmoc method of characteristics neutral particle transport code," *Annals of Nuclear Energy*, vol. 68, pp. 43–52, 2014 (cited on p. 53).

[65]  K. S. Kim, "Specification for the VERA depletion benchmark suite," *Consortium for Advanced Simulation of LWRs*, 2015 (cited on p. 53).

[66]  S. Yamanaka, K. Yamada, K. Kurosaki, *et al.*, "Characteristics of zirconium hydride and deuteride," *Journal of alloys and compounds*, vol. 330, pp. 99–104, 2002 (cited on p. 74).

[67]  OpenMC, *Quick install guide*, 2023. [Online]. Available: `https://docs.openmc.org/en/stable/quickinstall.html` (cited on p. 96).

[68]  OpenMC, *Official data libraries*, 2023. [Online]. Available: `https://openmc.org/official-data-libraries/` (cited on p. 96).

[69]  OpenMC, *Openmc depletion data generation scripts*, 2023. [Online]. Available: `https://github.com/nutcasev15/openmc-data/tree/endf80/depletion/endfb80` (cited on p. 96).

[70]  OpenMC, *Casl pwr nuclide branching ratios*, 2023. [Online]. Available: `https://github.com/nutcasev15/openmc-data/blob/endf80/depletion/branching_ratios_pwr.json` (cited on p. 96).

[71]  OpenMC, *Serpent fission q value generator*, 2023. [Online]. Available: `https://github.com/nutcasev15/openmc-data/blob/endf80/depletion/generate_serpent_fissq.py` (cited on p. 96).

[72]  OpenMC, *Infinite neutron multiplication factor simulation scripts*, 2023. [Online]. Available: `https://github.com/nutcasev15/MSc-Thesis/tree/main/Hex` (cited on p. 96).

[73]  OpenMC, *3d nsp reactor core simulation scripts*, 2023. [Online]. Available: `https://github.com/nutcasev15/MSc-Thesis/tree/main/Core` (cited on p. 96).

[74]  UoM, *Derivations for simple brayton heat cycle in space*, 2023. [Online]. Available: `https://github.com/nutcasev15/MSc-Thesis/blob/main/Thermal/NSP_Brayton.pdf` (cited on p. 97).

[75]  UoM, *Derivations for simple rankine heat cycle in space*, 2023. [Online]. Available: `https://github.com/nutcasev15/MSc-Thesis/blob/main/Thermal/NSP_Rankine.pdf` (cited on p. 97).

[76]  UoM, 2023. [Online]. Available: `https://github.com/nutcasev15/MSc-Thesis/tree/main/Thermal` (cited on p. 97).

[77]  P. C. Jain and S. C. Saxena, "Transport properties of helium in the temperature range 400–2300° K," *Chemical Physics Letters*, vol. 36, no. 4, pp. 489–491, 1975 (cited on p. 97).

# Appendix A : OpenMC Environment Setup and Python Scripts

In the interest of reproducibility of our results, this appendix guides the reader on the configuration of OpenMC as we used it for our parametric modelling studies. We followed the quick installed guide on the OpenMC documentation [67]. Installing the Miniconda software package manager, we used Mamba to install OpenMC 0.13.3. The official ENDF VIII.0 hdf5 neutron data libraries were available from [68]. Then, we wrote a script to generate a decay chain from the ENDF library data, which is available from [69]. We further processed the resulting decay chain with the CASL script at [69] and the list of decay nuclides present in PWRs at [70]. Finally, we used [71] to generate a database of fission Q values so that our depletion results would agree with SERPENT 2.1.31.

Once the setup is complete, the reader can download the BOL and depletion $K_{inf}$ simulation files from [72]. The 'BaseMat.py' file must be run to create the materials database used for the parametric simulations. Then, one can configure 'BOL.py' for running the BOL $K_{inf}$ study or 'Deplete.py' for the EOL $K_{inf}$ study. The model definition is found in 'OMC_model.py'. The 'BPlot.py' file parses the output pickle file of 'BOL.py' to generate the plots we saw in Chapter 5. 'BDiff.py' compares the results of different runs of 'BOL.py'. 'DPlot.py' post-processes the output of the depletion simulations.

Similar to the $K_{inf}$ simulations, the 3D core $K_{eff}$ BOL and depletion simulation files are available from [73]. 3D core Depletion studies were not included in this thesis for the reduction of its length. Again, the 'BaseMat.py' script must be run before the other simulations. The naming scheme and functions of the scripts are identical.

The results files for our simulations are included in [72] and [73], and the interested reader can run the post-processing scripts to obtain the plots produced in Chapters 5 and 6.

# Appendix B : Heat Engine Mathematics and GNU Octave Scripts

As promised in Chapter 3, we provide links to more detailed mathematical derivations for the Brayton cycle [74] and Rankine cycle [75]. Also, [76] links to the list of GNU Octave 8.3.0 scripts we used. The 'G_lim.m' script contains code for calculating the mass flux limits. It depends on the 'HeXe_mu_k_Pr.m' script, which calculates the transport properties of HeXe as a function of temperature and molar mass. 'JOHNSON-2006.xlsx' contains data from [41], which the script imports to calculate its outputs. 'JAIN-1975.xlsx' contains pure helium transport property data from [77]. 'FINK-1982' contains entropy and the ratio of specific heats data for sodium from [50] for the curve fits shown in Chapter 3. The 'HTC_gen.m' script uses those generated transport property data to create the GT tables we presented in Chapter 3 using Taylor's HTC correlation [40].

All the scripts mentioned above work to create CSV files for the HTC coefficient, which other programs can easily import. 'Gas_Model.m' imports the HTC data to solve linear power for the limiting fuel element for the gas-cooled pin-in-cell fuel element. 'LHP_Model.m' does the same but with isothermal evaporation conditions similar to sodium evaporation in a looped heat pipe in modern spacecraft.

'NSP_Brayton.m' and 'NSP_Rankine.m' are responsible for solving the mathematics of the Brayton and Rankine cycles and producing the plots shown in Chapter 3.